Universität
Rostock
Traditio et Innovatio

FLOW STRUCTURES AND HEAT TRANSFER ON DIMPLED SURFACES

Dissertation

zur

Erlangung des akademischen Grades

Doktor-Ingenieur (Dr.-Ing.)

der Fakultät für Maschinenbau und Schiffstechnik

der Universität Rostock

Rostock, 2012

---

vorgelegt von Dipl.-Ing. Johann Turnow
geboren am 13. Dezember 1981
in Dresden
aus Rostock

---

urn:nbn:de:gbv:28-diss2012-0074-8

Gutachter:

1. Gutachter

   Prof. Dr.-Ing. habil. Egon Hassel
   Institut für Technische Thermodynamik, Universität Rostock

2. Gutachter

   Prof. Dr.-Ing. habil. Nikolai Kornev
   Institut für Modellierung und Simulation, Universität Rostock

3. Gutachter

   Prof. Dr.-Ing. Heinz Herwig
   Institut für Thermo-Fluid-Dynamik, Technische Universität Hamburg-Harburg

Datum der Einreichung: 04.10.2011

Datum der Verteidigung: 24.04.2012

Abstract

Dimples are known to increase heat transfer with a low induced hydraulic loss in narrow channels. Main attention of papers published in the literature has been paid to the heat and mass transfer effects averaged in time whereas the unsteady processes and their role in the heat transfer enhancement have not been thoroughly investigated. Following the investigations of unsteady effects and its direct impact on heat transfer enhancement is the main subject of this thesis.

Vortex structures and heat transfer mechanism in a turbulent flow over a single dimple and a staggered dimple array in a narrow channel have been investigated using Large Eddy Simulation (LES), Reynolds-averaged Navier-Stokes (RANS) simulation, Laser Doppler Velocimetry (LDV), time resolved pressure measurements and dye visualizations. Considered are dimples with a depth to diameter ratio $h/d = 0.26$ for Reynolds numbers in the range of $\mathrm{Re}_d = 10000$ to $\mathrm{Re}_d = 40000$. The numerical methods have been validated with experiments, DNS data and empiric correlations published in literature. The flow and temperature fields are captured by LES using dynamic mixed model applied both for the velocity and temperature.

A test bench has been installed at the University of Rostock to validate the numerical methods and to investigate flow structures over dimpled surfaces using modern measurement techniques. The conducted time resolved pressure measurements and analysis of the time signals recorded from LDA measurements give a deep insight into flow physics.

In addition to the direct analysis of the flow field, the three-dimensional Proper Orthogonal Decomposition (POD) method has been carried out on LES pressure and velocity fields to identify spatio-temporal structures hidden in the random fluctuations.

A multi-objective design optimization based on mesh motion algorithm has been performed within the framework OpenFOAM for further improvement of the heat exchanger performance. Based on mesh motion technique and selected parameters for optimization, the surface can adopt an arbitrary shape and is not limited by any kind of interpolation. The aim of the procedure is to find the geometry most favorable to maximize heat exchange while obtaining a minimum hydraulic loss.

Contents

List of Figures

List of Tables

Nomenclature

Roman Symbols

Symbol	**Unit**	**Description**
$a^{(n)}$	$1/s$	POD time coefficients
A	m^2	Surface area
A^+	$-$	Parameter in van Driest damping function
b_i	$-$	optimization parameters
B	m	Channel width
c_p	$J/(kg \cdot K)$	Heat capacity
C^+	$-$	Wall normal constant
C_f	$-$	Friction coefficient
C_p	$-$	Resistance coefficient
Co	$-$	Courant number
C_k	$-$	Kolmogorov constant
C_S	$-$	Smagorinsky constant
$C(t, t^{'})$	m^2/s^2	Temporal correlation tensor
d	m	Dimple print diameter
D	m^2/s	Molecular diffusivity
D_{eff}	m^2/s	Effective viscosity
D_H	m	hydraulic diameter
D_t	m^2/s	Turbulent diffusivity
$\dot{E}_V$	J/s	Exergy loss
f	$1/s$	Frequency
F	$-$	cost function
G	K	Filter function
h	m	Dimple depth
H	m	Channel height
k	m^2/s^2	Turbulent kinetic energy
L	m	Reference length
N	$-$	Number of realizations

p	N/m^2	Pressure
p_{ij}	$-$	Hessian matrix
P_k	m^2/s	Turbulent production rate
$\dot{q}$	$J/(m^2 s)$	Specific heat flux
R_{ij}	m^2/s^2	Correlation tensor
S_{ij}	$1/s$	Strain rate tensor
S_f	m^2	Face area
S_ϕ	$-$	Source term
$\dot{S}_{Pro}$	W/m	Entropy production rate
t	s	time
T	K	Temperature
T_W	K	Wall temperature
u_i	m/s	Velocity component
u_τ	m/s	Friction velocity
U	m/s	Velocity
V	m^3	Volume

Greek symbols

α	$W/(m^2 \cdot K)$	Heat transfer coefficient
δ_T	m	Thermal boundary layer thickness
δ	m	Velocity boundary layer thickness
$\overline{\Delta}$	m	Filter length scale
ϵ	$J/(kg \cdot s)$	Dissipation rate
η	m	Kolmogorov dissipation lengthscale
Θ^+	$-$	non-dimensional wall temperature
κ	m^{-1}	Wavenumber
λ	$W/(m \cdot K)$	Heat conduction coefficient
ν	m^2/s	Kinematic viscosity
ν_t	m^2/s	Turbulent kinematic viscosity
ρ	kg/m^3	Density
τ_{ij}	$kg/(m \cdot s^2)$	Stress tensor
τ_w	$kg/(m \cdot s^2)$	Wall stress tensor
ϕ	$-$	Conserved quantity
$\Phi_i^{(n)}$	m	Orthogonal base functions of POD
ψ	$-$	Fanning friction factor

ω	s^{-1}	Vorticity
Ω_{ij}	kg/ms^2	Vorticity tensor

Dimensionless Groups

Kn	Knudsen number
Nu	Nusselt number
Pr	Prandtl number
Re	Reynolds number
St	Strouhal number

Subscripts

$(\ldots)_0$	–	Equivalent for a flat plate
$(\ldots)_d$	–	Equivalent for the standard dimple
$(\ldots)^+$	–	Normalized value
$(\ldots)'$	–	Fluctuating part
$(\ldots)^a$	–	Anisotropic, deviatoric part of a tensor
$(\ldots)_\tau$	–	Friction, shear based value
$(\cdots)_b$	–	Bulk, freestream value
$\langle\cdots\rangle$	–	Time averaged value
$\overline{\cdots}$	–	Spatial filtered value
$\widehat{\cdots}$	–	Test filtered value

Abbreviations

CDS	Central Difference Scheme
CFD	Computational Fluid Dynamics
CFL	Courant Friedrich Levy
DLR	Deutsches Zentrum fr Luft- und Raumfahrt
DNS	Direct Numerical Simulation
DMM	Dynamic Mixed Model
DSM	Dynamic Smagorinsky Model
FEM	Finite Element Method
FFT	Fast-Fourier-Transformation

FVM	Finite Volume Method
LDA	Laser Doppler Anemometry
LES	Large Eddy Simulation
OpenFOAM	Opensource Field Operation and Manipulation
PDE	Partial Differential Equation
PDF	Probability Density Function
POD	Proper Orthogonal decomposition
rms	root mean square
RANS	Reynolds-Averaged-Navier-Stokes
URANS	Unsteady Reynolds-Averaged-Navier-Stokes
SGS	Subgrid Scale
SST	Shear-Stress-Transport
STL	Surface Tesselate Language
UDS	Upwind Difference Scheme

1 Introduction

1.1 Motivation

The importance of understanding heat transfer mechanism in technical devices is increasing due to the limited energy resources and its growing demand of optimal usage. Especially the convective heat transfer mechanism plays a decisive role for the overall system and economy performance in technical devices which is therefore in the main focus of many research groups.

Methods like surface roughness, mechanical impact (e.g. vibration) and vortex generating elements are known to enhance heat transfer. In the last decade special research interest has been paid to turbulators (Fiebig et al. [22] [21]] to analyze hydrodynamic mechanism and intensification of heat exchange using numerical simulations and experiments. The main idea is to place so-called turbulators at the cooling side to induce longitudinal and vertical vortices, what results in a disruption of the thermal boundary layer and thus augments heat transfer. The turbulators can be designed in different ways like wings or ribs to manipulate the internal flow field. Beside its high efficiency to increase heat transfer some disadvantages can be pointed out like blocking of the cooling channels, drastic raise of flow resistance, complicated installation, etc. To overcome these negative side effects, especially in narrow channels, convex surface depressions called dimples attracted interest in the last decades. Dimples show the following advantages compared to other devices like riblets or fins.

- intensification of heat transfer compared to flat surfaces
- no blocking of the channels
- reduction of the weight
- self cleaning due to vortex structures
- simpleness of design
- small increase of flow resistance.

The practical and effective way of heat transfer enhancement by dimples is well-known and is already used in commercial heat exchangers. The heat transfer can be significantly enhanced compared to a smooth wall and is about the same as that obtained by conventional ribs, whereas the hydraulic resistance inside the cooling channel was found to be small. Detailed experimental investigations have been performed by Ligrani et al. [60]. A comparison of overall heat transfer in terms of Nusselt number Nu and overall resistance C_p normalized by the values of an equivalent smooth channel Nu_0 and C_{p0} for many configurations is presented in Fig. 1.1.

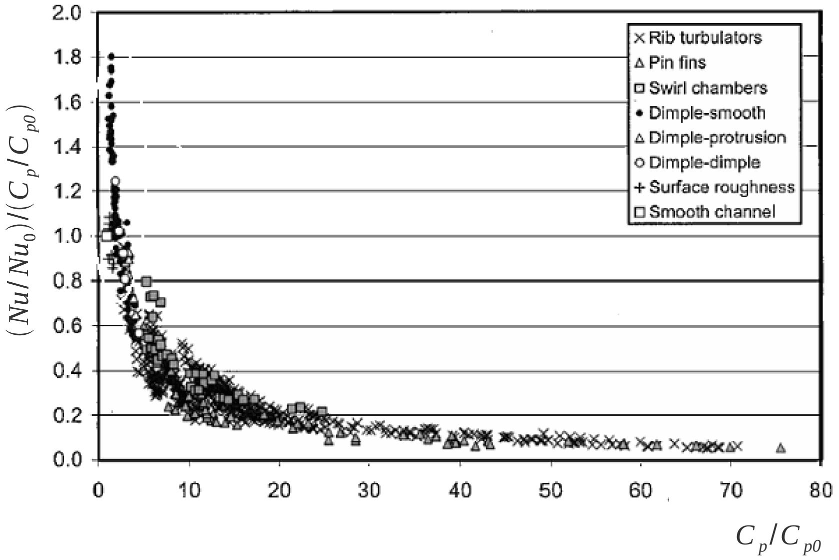

Fig. 1.1: Measurement data of integral heat transfer Nu and flow resistance C_p for different turbulator designs in comparison to an equivalent flat wall Nu_0 and C_{p0} in narrow channels (Ligrani et al. [60]).

The experimental results reveal that the best performance $(\mathrm{Nu}/\mathrm{Nu}_0)/(C_p/C_{p0}) > 1$ can be obtained by using dimples for internal cooling. In other words, the increase of heat transfer is much higher than the additional induced hydraulic losses inside the cooling passage. Two reasons for this behavior can be found. First the heat transfer surface is increased due to dimple geometry and second due to the formation of special vortex structures which amplify convection processes inside and outside the dimples. It was found that the overall heat transfer augmentation can reach approximately a factor of $\mathrm{Nu}/\mathrm{Nu}_0 = 2.5$ referred to an equivalent flat wall (see Chyu [15]). Since the increase of the heated surfaces in case of dimples is only 20%, the impact of the vortex formations on heat transfer is much higher than the surface enlargement. Hence, one may conclude, that the complete understanding of vortex formations and its impact on the local heat transfer is indispensable to design an efficient dimple geometry.

1.2 Heat transfer enhancement using dimples

In general, dimples are known already from golf ball aerodynamics. In this classical case applications of dimples are understood as a special form of surface roughness which shift the typical drop down of the pressure resistance for blunt bodies into the low Reynolds number range (Davis [16], Williams [98]). Initially, the idea was to use dimples simply for drag reduction. Wieghardt et al. [96] documented the influence of dimples in terms of friction factor. Remarkably results have been published from the DLR in Colone by Wuest [100]. In this study the application of dimples on ICE reduces the forces from sidewinds up to 17%. Breuer et al. [59] performed experimental and numerical studies using dimples for drag reduction in a channel. No drastic reduction of drag has been documented for the investigated geometrical configurations of dimples. However, a high increase of drag resistance was also not observed which implies that dimples can be used to enhance heat transfer without significant hydraulic losses. First publications using dimples for intensification of heat transfer have been published by Kuethe [56] and Presser [81]. Presser determined a strong heat transfer enhancement of $\mathrm{Nu}/\mathrm{Nu}_0 = 2.2$ in turbulent flow over three-dimensional cavities for a wide range of Reynolds numbers. Afanasyev et al. [1] investigated the pressure drop and heat transfer on a plate with a staggered array of dimples in the turbulent flow regime. It was reported that the heat transfer augmentation is about 30-40% with a negligible induced pressure drop. Most motivating results using dimples have been performed by Chyu [15], who investigated the pressure drop and heat transfer improvement for the surface roughened by an array of hemisphere and tear-drop shaped cavities in the range of Reynolds number

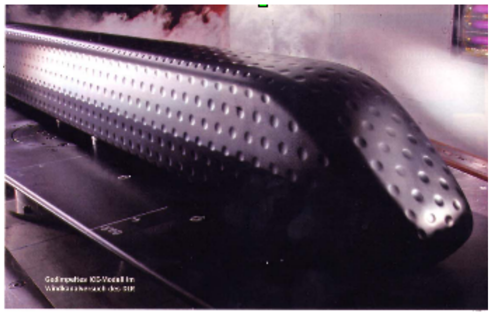

Fig. 1.2: Application of dimples on ICE trains to reduce side drag [100].

$\mathrm{Re}_{Dh} = 10'000 - 50'000$ based on the hydraulic diameter. The increase of heat transfer coefficients of both configurations was determined to be 2.5 times higher than compared to the opposite smooth wall whereas the induced pressure resistance was as twice as small compared to rib turbulators. The effect of the channel height and dimple depth on heat transfer in turbulent flow regimes was studied by Moon et al. [77] and Burgess et al. [11]. It was evaluated that the heat transfer and friction factor augmentation increases for a decreasing channel height and a rising dimple depth. Today a large number of experimental investigations have been performed for different dimple geometries yielding to an overall heat transfer enhancement of about 200 - 300% in combination with a low flow resistance compared to other structured surfaces like ribs (see Ligrani et al. [60] and Ekkad et al. [17]).

Nevertheless, main attention of papers published in the literature has been paid to the heat and mass transfer effects averaged in time whereas the important unsteady processes including the vortex formations and their role in the heat transfer enhancement have not been thoroughly investigated. Snedeker et al. [86] documented an unusual asymmetric distribution of the flow in a three-dimensional surface depression. Two stable vortex positions for special dimple configurations have been estimated whereas the axis of the vortex has a certain angle towards the main flow. The authors have demonstrated that only asymmetric vortex structures can exist in a stable state for dimples with a high ratio of dimple depth to dimple print diameter. The visualizations and velocity measurements from Gromov et al. [29] confirmed and extended the results of Snedeker et al. [86].

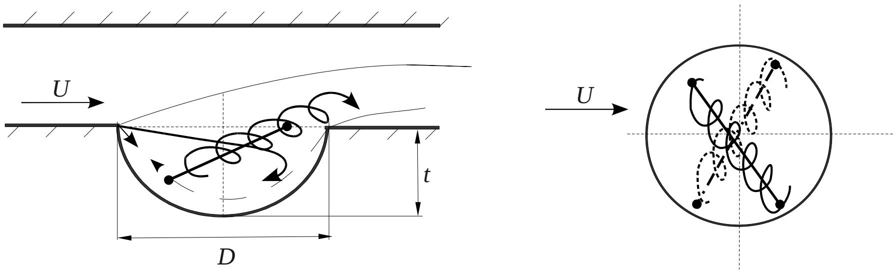

Fig. 1.3: Asymmetric vortex structures of turbulent flow over a single dimple with a high ratio of dimple depth to dimple print diameter proposed by Snedeker [86].

It was found that the position of the vortex changes between two positions for high Reynolds numbers in time. For lower Reynolds numbers in the laminar and transitional range the vortex inside the dimple occurs as symmetric with respect to the main flow direction. It becomes unstable by increasing flow rates and changes finally to an asymmetric formation. Hiwada et al. [33] discovered three different flow regimes for various depths of the cylindrical cavity where two of these were auto oscillations. The heat transfer measurements showed that an auto oscillating regime at a ratio $h/d = 0.5$ is an ideal regime for heat transfer enhancement. It is characterized by an explicit asymmetry of the pressure distribution which is in line with the observations of Snedeker et al. [86] and Gromov et al. [29]. Analysis of flow regimes and local heat transfer on dimples have been studied by Kiknadze et al. [48] [49]. It has been documented that the set of three-dimensional cavities can increase in the heat transfer coefficient up to $\mathrm{Nu}/\mathrm{Nu}_0 = 2.4$ while keeping the aerodynamic resistance at a minimum. From flow visualization studies it can be seen that the flow is both complex and can take different forms by its nature and depends upon the geometric parameters of the cavity. Fig. 1.4 presents tornado-like spatial flow structures inside dimples arising into the main channel flow which are identified and used to explain the high thermo-hydraulic performance of dimples. Further it was found that a dynamic vortex with transverse oscillations towards the main flow evolves enforcing the heat flux inside and outside the dimple. Nevertheless, the tornado-like structures have not been confirmed in other publications, whereas the transverse oscillations are in line with Hiwada et al. [33]. One of the most detailed investigations of flow over a single dimple was done by Terekhov et al. [89], [88]. The visualization using hydrogen bubbles, LDA and pressure measurements revealed a complex and oscillating vortex structure with periodical outburst at the downstream rim of the dimple with a ratio of $h/d = 0.26$. Transverse oscillations of the outbursts with low ($f < 1Hz$) and high frequency ($f > 1Hz$) were observed at the Reynolds numbers up to $\mathrm{Re}_d = 40000$. Analysis of instantaneous pictures reveal a consequent process of generation of regular vortices in the recirculation zone inside the dimple. Their shedding downstream result in the formation of staggered rows of vortices. The most detailed experimental study of unsteady flow characteristics on dimpled packages has been performed by Ligrani et al. [60], [61], [62] and Mahmood et al. [70], [71]. A primary vortex pair formed periodically in the center of the

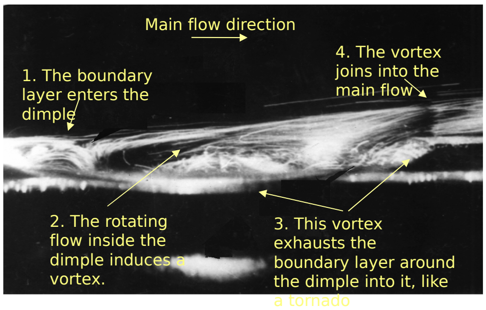

Fig. 1.4: Tornado-like jets running out of dimples and penetrating into the main flow (Kidnaze [48]).

dimple has been visualized using smoke patterns. In addition, two secondary vortex pairs appearing near the spanwise edges of a spherical dimple at $\mathrm{Re}_H = 1250$ are determined (see Fig. 1.5). For dimples with a depth to diameter ratio of $h/d \geq 0.22$ a significant augmentation of heat transfer is documented due to dynamic vortex structures with transversal oscillations around the dimple area. Ligrani et al. [60], [61], [62] conducted many studies to establish a data basis including the pressure drop and heat transfer values according to various dimple and channel geometries. Numerical studies of dimpled heat exchangers have been performed by a number of researchers. Park et al. [79] examined turbulent flow over dimples with a ratio $h/d = 0.3$ using RANS method for Reynolds numbers $\mathrm{Re}_H = 2700$ up to $\mathrm{Re}_H = 41000$. This study provides an insight into the development of flow structures produced by the dimples and the increase of heat transfer rates, whereas the integral values were not in good agreement to experimental data. The results showed the existence of a rotating vortex pair generated inside and upstream each dimple and a second pair at the spanwise edges of the dimple. Burgess et al. [11] investigated the impact of dimple depth on the integral heat transfer rates. It was reported that the heat transfer increases by enlargement of the dimple depth, whereas the flow resistance is also increased. Wang et al. [94] carried out research of low Reynolds number flow in dimpled channels of $\mathrm{Re}_\tau = 180$ based on the friction velocity. The existence of a symmetric horseshoe vortex was documented inside a single dimple. The most detailed numerical investigations have been performed by Isaev [39], [40]. Usage of overlapping grids and equations, written in a conservative form, established the possibility to perform calculations with high resolved zones inside and outside the dimple. This method in combination with the k-ω-SST model proposed by Menter [74] showed best results in comparison to experiments. On the basis of URANS a series of vortex formations inside have been performed which change quantitative as well as qualitative depending on the ratio dimple depth to dimple

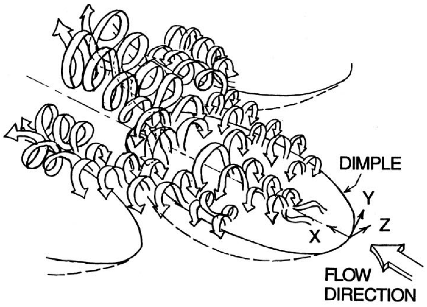

Fig. 1.5: Sketch of three-dimensional flow structure and visualization images in different planes for of the flow $\mathrm{Re}_H = 1250$ and $h/d = 0.5$ from Ligrani [60].

print diameter. Two symmetric vortex structures in Fig. 1.6 (left) change into a single vortex structure by increasing the ratio h/d starting from $h/d = 0.22$ (see Fig. 1.6 (right)). This result is in accordance with measurements performed by Terekhov [89] for a dimple with a ratio $h/d = 0.26$. Numerical results showed that asymmetric vortex structures provide a higher efficiency than symmetric ones. For the turbulent flow regimes it was suggested to define the dimple geometry for each purpose to generate mono core vortex structures using an asymmetric dimple shape [41]. A numerical study of dimples at the lower and protrusions at the upper wall of the channel to enhance heat transfer was done by Elyyan et al. [18]. Calculations have been performed over a wide range of Reynolds numbers from $\mathrm{Re}_H = 200$ up to $\mathrm{Re}_H = 15000$ including laminar, transient and fully turbulent flow. A large database has been established for pressure drop, friction factor and Nusselt number values according to variations of the Reynolds number.

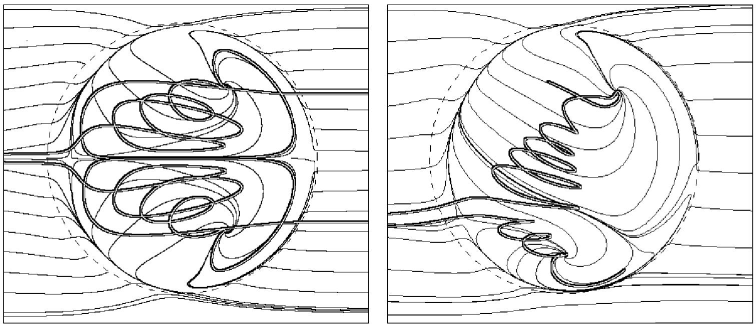

Fig. 1.6: Bifurcation of vortex structures in a spherical dimple with a ratio $h/d = 0.22$ for symmetric (*left*) and asymmetric (*right*) patterns.

1.3 Scope of this work

Investigations of heat transfer and flow structures on dimple shaped surfaces using numerical and experimental methods with focus on the unsteady effects and their direct impact on heat transfer have been performed. The different methods are established through this work to analyze the heat transfer and flow structures of turbulent flow up to $\mathrm{Re}_d = 40000$ over a single spherical dimple in detail. The methods are extended together with the latest findings for dimples arranged in a staggered package. Following an optimization technique has been developed to determine preferable surface structures in terms of high heat transfer rates and low hydraulic losses.

The thesis is divided into two parts. In the first part the theoretical background and numerical methodologies are presented. The basic theory of heat transfer mechanism, the characteristics of turbulence characteristics and boundary layer behaviour is discussed in chapter 2. Since the focus in this work is placed on unsteady effects, the derivation of the filtered partial differential equations and and closure models written in terms of LES for fluid motion and heat transfer are presented in chapter 3. The equations and closure models for RANS modeling and the discretization practices of the Finite Volume Method (FVM) are briefly introduced. Chapter 4 presents the implemented Proper Orthogonal Decomposition (POD) method to determine high energy containing spatial structures and its physical interpretation. The established test bench and its methods for experimental investigations are described in chapter five which closes the first part of the thesis.

The experimental and numerical results are presented in the second part of this thesis. The heat transfer mechanism and flow structures of a single spherical dimple in a narrow channel are described in chapter 6 including the validation of the numerical and experimental methods with the help of DNS calculations and empiric correlations published in the literature. In addition, the results through the POD method are discussed in detail. The applied methods are extended on dimples arranged in a staggered package whereas the results concerning heat transfer, flow structures and POD modes are presented in chapter 7. The optimization process and its application on the basis of the framework OpenFOAM to find an optimal shape of the heat transfer surface is introduced in chapter 8. Finally, the thesis is closed with a conclusion given in chapter 9.

2 Governing Equations

The fundamental partial differential equations (PDE's) for heat transfer and fluid dynamics are presented in the following sections. The equations describe the flow dynamics and heat transfer of fluids in terms of pressure p, velocity $U = (u\ v\ w)^T$ and temperature T which are functions of space $\overrightarrow{x}$ and time t.

2.1 Heat transfer mechanism

The heat exchange is defined as a transfer of energy in the form of heat from a fluid with a high temperature to a fluid with a low temperature and can be characterized into three parts: heat conduction, heat radiation and convective heat transfer.

- **Heat conduction** is the transport of thermal energy between molecules due to the temperature gradient in a fluid or solid. The heat is always transferred from the high temperature towards low temperature level and is proportional to the temperature gradient (second law of thermodynamics).
- **Heat radiation** is the transfer of energy in the form of electro magnetic waves. It can also occur inside a vacuum and is therefore not dedicated to a special matter.
- By **convective heat transfer** the energy is transported by the macroscopic movement of fluids. It will occur between a surface and a moving fluid when both media have different temperature levels.

The focus of this work is based on heat conduction and convective heat transfer, whereas heat radiation will be neglected. The heat flux due to conduction can be understand as transfer of energy from the more energetic molecule to the less energetic molecule which can be calculated using the Fourier law in the one-dimensional form

$$q_x = -\lambda \cdot \left(\frac{\partial T}{\partial x} \right) . \tag{2.1}$$

The variable λ is called heat transfer conduction coefficient and is specific to the present material and depends on the temperature. The heat flux $\vec{\dot{Q}}$ normal through a differential surface element dA can be written as

$$d\dot{Q} = -\lambda \cdot \nabla T \cdot \vec{n} \cdot dA = -\lambda \frac{\partial T}{\partial n} \cdot dA\,. \tag{2.2}$$

Convective heat transfer can be classified into free and enforced convection. Free convection is only driven by buoyancy forces due to density differences whereas enforced convection is driven from external means e.g. by a fan or a pump. Since the overall temperature differences are assumed to be small, the density ρ of the fluid will not change and thus buoyancy forces can be neglected. To quantify the heat transfer between a fixed wall with a temperature T_W and a fluid with a temperature T_F, the heat transfer coefficient α is introduced to obtain the resulting heat flux as

$$\dot{q}_W = \alpha \left(T_W - T_F\right)\,. \tag{2.3}$$

The heat transfer coefficient α summarizes all unknown parameters like velocity, surface roughness and boundary layer thickness. Hence, the main goal of experiments and numerical simulations is the determination of the local and global heat transfer coefficient α. In common heat exchangers like parallel or cross flow exchangers, the heat is transferred from the hot wall towards the cold flow. Infinite to the wall the energy can only be transferred by heat conduction, due to the wall bounding of the fluid. Thus the definition of Fourier's law (see Eq. 2.1 can be applied direct at the wall for evaluation of the heat flux (see Incropera [37]) in the form of

$$\dot{q}_W = -\lambda \left.\frac{\partial T}{\partial n}\right|_W\,. \tag{2.4}$$

Hence, the heat transfer coefficient α can be derived using Eq. 2.3 and 2.4

$$\alpha = -\lambda \frac{1}{T_W - T_F} \left.\frac{\partial T}{\partial n}\right|_W\,. \tag{2.5}$$

The Nusselt number is introduced as dimensionless variable calculated by a characteristic length of the heat exchanger L and heat conduction coefficient λ

$$Nu = \frac{\alpha L}{\lambda} \tag{2.6}$$

for quantitative comparison of heat transfer rates of different heat exchangers. For comparison of the different temperature levels it is often useful to rewrite the temperature T in a non-dimensional way as

$$T^+ = \frac{T - T_0}{\Delta T}. \tag{2.7}$$

The temperature T_0 is the reference temperature and ΔT is the characteristic temperature difference. In terms of non-dimensional quantities the heat transfer coefficient α in Eq. 2.5 can be formally written as

$$\alpha = -\lambda \frac{1}{T_W^+ - T_F^+} \left.\frac{\partial T^+}{\partial n}\right|_W . \tag{2.8}$$

With definition of non-dimensional values the calculation of Nusselt number results in

$$Nu = -\frac{1}{T_W^+ - T_F^+} \left.\frac{\partial T^+}{\partial n}\right|_W L \, . \tag{2.9}$$

As it can be seen from the Eq. above, the Nusselt number depends on the temperature gradient at the wall, the dimensionless temperature T_w^+ at the wall and the fluid temperature T_F^+. To estimate the integral Nusselt number Nu_m of the whole heat transfer surface A, the local Nusselt number Nu can be integrated

$$Nu_m = \frac{1}{A\left(T_W^+ - T_F^+\right)} \int\limits_A Nu \left(T_W^+ - T_F^+\right) \, dA \, . \tag{2.10}$$

If the temperature difference $T_W^+ - T_F^+$ is constant, Eq. 2.10 can be written as

$$Nu_m = \frac{1}{A} \int\limits_A Nu \, dA \, . \tag{2.11}$$

Finally, the overall heat flux using the integral Nusselt number Nu_m can be calculated as

$$\dot{Q} = \lambda \frac{Nu_m}{L} \left(T_W - T_F\right) A \, . \tag{2.12}$$

2.2 Fluid dynamics

Within the continuum mechanics, where the scale of representing of motion is larger than the mean free path of molecules (*Knudsen* number $\mathrm{Kn} \ll 1$), the fluid motion is described by the principle of conservation of mass, momentum and energy expressed in a continuous way in space and time.

Conservation of mass The equation expresses the conservation of mass in an infinite control volume dV. The difference of the entering and outgoing mass flow of the control volume dV at each time interval under consideration of the variable density ρ can be written in integral form as

$$\int\limits_{(V)} \frac{\partial \rho}{\partial t} dV + \int\limits_{(A)} \rho u_i dA = 0. \tag{2.13}$$

Eq. 2.13 can be transformed using Gauss theorem into the differential form

$$\frac{\partial \rho}{\partial t} + \frac{\partial(\rho u_i)}{\partial x_i} = 0. \tag{2.14}$$

For incompressible flows ($\rho = const$) the equation results in

$$\frac{\partial u_i}{\partial x_i} = 0, \tag{2.15}$$

which implies a divergence free field of the velocity.

Conservation of momentum The time variation of momentum is equal to the sum of the forces acting on the control volume dV. In this case, the sum of the time variation of the momentum inside dV and its flux through the boundaries dA is equal to the sum of the surface and volume forces acting on dV, which can be written in integral form as

$$\int\limits_{(V)} \frac{\partial(\rho u_i)}{\partial t} dV + \int\limits_{(A)} \rho u_i u_j dA = -\int\limits_{(A)} p dA + \int\limits_{(A)} \tau_{ij} dA + \int\limits_{(V)} \rho f_i dV. \tag{2.16}$$

The value p denotes the pressure, τ_{ij} the tensor of viscous stresses and f_i the volume (body) forces. The balance equation of momentum can be rewritten using Gauss theorem as

$$\frac{\partial \rho u_i}{\partial t} + \frac{\partial(\rho u_i u_j)}{\partial x_j} = -\frac{\partial p}{\partial x_i} + \frac{\partial \tau_{ij}}{\partial x_j} + \rho f_i. \tag{2.17}$$

The stress tensor can be derived from Newton's hypothesis:

$$\tau_{ij} = 2\mu S_{ij} - \frac{2}{3}\mu \frac{\partial u_k}{\partial x_k}\delta_{ij} \tag{2.18}$$

in terms of the strain rate tensor S_{ij}

$$S_{ij} = \frac{1}{2}\left(\frac{\partial u_i}{\partial x_j} + \frac{\partial u_j}{\partial x_i}\right). \tag{2.19}$$

Newtonian isothermal flow with constant fluid properties ($\rho, \nu = const$) without any body forces is assumed in the conducted investigations which results in the simplified momentum equation

$$\frac{\partial u_i}{\partial t} + \frac{\partial(u_i u_j)}{\partial x_j} = -\frac{\partial P}{\partial x_i} + \frac{\partial}{\partial x_j}\left(\nu 2 S_{ij}\right), \tag{2.20}$$

where $P = p/\rho$ is the pseudo pressure and $\nu = \mu/\rho$ the kinematic viscosity. The derived balance equation in combination with the conservation of mass are commonly known as the incompressible Navier-Stokes equations.

Conservation of energy The equation of energy transport can be derived from the first law of thermodynamics using the equation of state $dh = c_p dT$ and the definition of the Prandtl number Pr

$$\mathrm{Pr} = \frac{\nu}{a} \tag{2.21}$$

where a is the heat conduction coefficient of the fluid ($a = \lambda/(\rho c_p)$). The energy equation can be formulated with the assumption of constant material properties as

$$\frac{\partial\left(\rho c_p T\right)}{\partial t} + \frac{\partial\left(\rho c_p u_i T\right)}{\partial x_i} = \frac{\partial}{\partial x_i}\left(\rho c_p \frac{\nu}{\mathrm{Pr}} \frac{\partial T}{\partial x_i}\right) + S_Q\,. \tag{2.22}$$

The form of the thermal energy balance equation is similar to a general scalar transport equation. The second term of the left side of Eq. 2.22 represents the heat transfer through convection whereas the first part takes care of the instationary part. The terms on the right hand side represent an arbitrary source term S_Q and the heat transfer diffusion through heat conduction. No outer heat sources are considered in this work which leads to $S_Q = 0$. As mentioned above, the impact of temperature T on the physical properties of the fluid is assumed to be small and can therefore be neglected (ρ, ν, c_p, $Pr = const$). Thus the thermal energy equation is fully decoupled of the Navier-Stokes equations what results into a passive scalar transport equation:

$$\frac{\partial T}{\partial t} + \frac{\partial\left(u_i \cdot T\right)}{\partial x_i} = \frac{\nu}{Pr}\frac{\partial^2 T}{\partial x_i^2}. \tag{2.23}$$

Using the non-dimensional temperature T^+ (see Eq. 2.7), the thermal energy equation results in

$$\frac{\partial T^+}{\partial t} + \frac{\partial\left(u_i \cdot T^+\right)}{\partial x_i} = \frac{\nu}{Pr}\frac{\partial^2 T^+}{\partial x_i^2}\,. \tag{2.24}$$

2.3 Properties of turbulent flows

To analyze the impact of turbulence on heat and mass transfer, the characteristics of turbulent flows are introduced. The problem of turbulence was formulated by Leonardo da Vinci's (1452-1519), who draw the famous picture illustrating multi-scale vortical character of turbulent flows (Fig. 2.1).

Even six centuries later it is rather difficult to define turbulence in an exact way. Osborne Reynolds was the first, who studied the transition and turbulence in a pipe

Fig. 2.1: Leonardo da Vinci's studies of turbulent motion.

flow. He found that the onset of transition depends upon a dimensionless parameter, the Reynolds number Re, which O. Reynolds defined as

$$\mathrm{Re} = \frac{U \cdot d}{\nu}. \tag{2.25}$$

It represents the ratio of diffusion to convection time or inertial force to viscous force. In the experiments, Reynolds found, that the flow is turbulent when the Reynolds number is greater than a critical value, which is around 2300 for flow inside a circular pipe. It is explained that at high Reynolds numbers flow, the viscous forces are much smaller than the inertial forces. So the flow cannot be longer stabilized and becomes unstable. If the Reynolds number is large enough, the flow finally becomes turbulent. Although turbulence is not completely understood, its important features can be described qualitatively:

- Turbulent flows are irregular and disorganized. This important feature appears in almost any definition of turbulence. Because of irregularity, the deterministic approach to turbulence becomes impractical to describe the turbulent motion in all details as a function of time and space coordinates.

- Turbulent flows are diffusive. It causes rapid mixing and increased rates of momentum, heat and mass transfer. Turbulent flows are able to mix transported quantities much more rapidly than if only molecular diffusion processes were involved. For example, if a passive scalar (like the temperature T) is transported by the flow, a certain amount of mixing will occur due to molecular diffusion. In a turbulent flow, the same sort of mixing is observed, but in a much greater amount than predicted by molecular diffusion.

- Turbulent flows are dissipative. Viscosity effects will result in the transformation of kinetic energy into heat. If there is no external source of energy to overcome the kinetic energy loss, the turbulent motion will decay.

- Turbulent flows are three dimensional and rotational. The flow evolves in every direction due to the vortex stretching and is therefore a function of space and time.
- Turbulent flows are characterized as a continuum problem. Even the smallest scales that occur in a turbulent flow are far larger than any molecular length scale.
- Turbulent flows are defined on multi-scales. Turbulent motion exist on different time and length scales due to the interaction and superposition.

The balance equations of mass and momentum contain all turbulence properties and describe the motion of incompressible newtonian fluids, since the equations are derived directly from conservation laws. However, excepting for very simple flows, there is no analytical solution for these equations. To get an insight into the turbulent motion and its effect on heat and mass transfer, statistical description of turbulent flows needs to be introduced. Thus, the velocity field $u_i(\mathbf{x},t)$ is decomposed into its mean value $\langle u_i(\mathbf{x},t)\rangle$ and a time varying fluctuating part $u_i^{'}(\mathbf{x},t)$, which can be formally written as

$$u_i^{'}(\mathbf{x},t) \;=\; u_i(\mathbf{x},t) - \langle u_i(\mathbf{x},t)\rangle \tag{2.26}$$

whereas

$$\langle u_i^{'}(\mathbf{x},t)\rangle = 0. \tag{2.27}$$

The statistical average is often called Reynolds average, which can be evaluated by different operations. The ensemble average is the statistical average over N different realizations and is formulated as

$$\langle u_i(\mathbf{x},t)\rangle_E = \lim_{N\to\infty}\frac{1}{N}\sum_{k=1}^{N} u_i^{(k)}(\mathbf{x},t)\,. \tag{2.28}$$

The phase averaging is useful for periodic processes to average the value over a time period t_n in terms of

$$\langle u_i(\mathbf{x},t)\rangle_P = \lim_{N\to\infty}\frac{1}{N}\sum_{k=1}^{N} u_i(\mathbf{x},t+T_k)\,. \tag{2.29}$$

Moreover, according to the Ergodic theorem for stationary and homogeneous processes, the ensemble averaging can be written as time averaging in the form of

$$\langle u_i(\mathbf{x},t)\rangle = \lim_{T\to\infty}\frac{1}{T}\int_0^T u_i(\mathbf{x},t)\,\mathrm{d}t\,. \tag{2.30}$$

A general statistical description of the turbulence is based on correlations between two velocity fluctuations at two different points and and different times

$$R_{ij}(\mathbf{r},\tau) = \langle u_i^{'}(\mathbf{x},t) u_j^{'}(\mathbf{x}+\mathbf{r},t+\tau)\rangle, \tag{2.31}$$

which is called cross-correlation function. Mostly all correlation functions are normalized by $\langle u_i u_j \rangle$ limiting the function in the range of -1 to $+1$. The correlation at two different points is called auto-correlation in space in the case of $\tau = 0$ at same time instant

$$R_{ij}(\mathbf{r},t) = \frac{\langle u_i^{'}(\mathbf{x},t) u_j^{'}(\mathbf{x}+\mathbf{r},t)\rangle}{\langle u_i^{'}(\mathbf{x},t) u_j^{'}(\mathbf{x},t)\rangle} \tag{2.32}$$

whereas $\mathbf{r} = 0$ gives auto-correlation of time

$$R_{ij}(\mathbf{x},\tau) = \frac{\langle u_i^{'}(\mathbf{x},t) u_j^{'}(\mathbf{x},t+\tau)\rangle}{\langle u_i^{'}(\mathbf{x},t) u_j^{'}(\mathbf{x},t)\rangle}. \tag{2.33}$$

The integral lengthscales can be calculated to determine the extension of fluid structures inside the flow by integration of the autocorrelation function. It is often used to ensure whether the computational domain is large enough to capture all flow structures. The integral lengthscale is derived from

$$L_{ij}(\mathbf{x},t) = \frac{1}{R_{ij}(0,t)} \int\limits_0^\infty R_{ij}(\mathbf{r},t)\,\mathrm{d}r. \tag{2.34}$$

An additional generalized turbulence lengthscale can be derived from similarity analysis in terms of kinetic energy k and its rate of dissipation ε

$$L \equiv \frac{k^{3/4}}{\varepsilon}\ . \tag{2.35}$$

Kolmogorov postulated the definition of the smallest scales of a turbulent structure

$$\eta \equiv \left(\frac{\nu^3}{\varepsilon}\right)^{1/4}\ . \tag{2.36}$$

The ratio between the largest to the smallest scales can be expressed

$$\frac{L}{\eta} = Re_L^{3/4} \tag{2.37}$$

in dependence on the turbulent Reynolds number and can be used to determine the grid resolution for a Direct Numerical Simulation (DNS). It is useful to transform the velocity autocorrelation into Fourier space to get a deep insight into energetic processes

$$\Phi_{ij}(\boldsymbol{\kappa}) = \frac{1}{(2\pi)^3} \int\limits_{-\infty}^{\infty} R_{ij}(\mathbf{r}) e^{-i\boldsymbol{\kappa}\cdot\mathbf{r}} \,\mathrm{d}\mathbf{r} \tag{2.38}$$

$$R_{ij}(\mathbf{r}) = \int\limits_{-\infty}^{\infty} \Phi_{ij}(\boldsymbol{\kappa}) e^{i\boldsymbol{\kappa}\cdot\mathbf{r}} \,\mathrm{d}\boldsymbol{\kappa} \tag{2.39}$$

whereas $\boldsymbol{\kappa}$ is the wavenumber. Hence, the energy spectrum of the flow can be estimated by integrating $0.5\Phi_{ij}$ (Pope [80]) from

$$E(\kappa) = \oint \frac{1}{2} \Phi_{ii}(\boldsymbol{\kappa}) \mathrm{d}S(\kappa) \; . \tag{2.40}$$

The term $S(\kappa)$ denotes the sphere in wavenumber space and κ is the magnitude $|\boldsymbol{\kappa}|$.

The energy spectrum $E(\kappa)$ obtained from experiments and simulations for fully developed turbulent flows *far away from the wall* shows an universal behavior for high Reynolds number presented in Fig. 2.2.

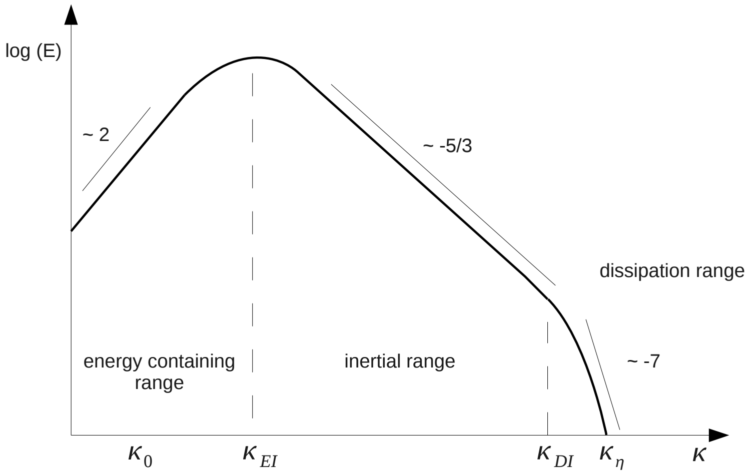

Fig. 2.2: Sketch of the one-dimensional energy spectrum for turbulent flows.

The schematic energy spectrum in logarithmic scale shows three different ranges (Fox [24])

- the energy containing range ($0 \leq \kappa \leq \kappa_{\mathrm{EI}}$),
- the inertial range ($\kappa_{\mathrm{EI}} < \kappa < \kappa_{\mathrm{DI}}$),
- the dissipation range ($\kappa_{\mathrm{DI}} \leq \kappa$).

The mechanism is called energy cascade, which can be interpreted as energy transfer from the large $\kappa_{EI} = 2\pi/L$ to the small scales $\kappa_\eta = 2\pi/\eta$. The energy containing range corresponds to large scale fluid motions producing the most kinetic energy due to outer forces. The range between energetic eddies and small scale dissipative eddies is called inertial range. The energy decay can be identified by Kolmogorovs law $E(\kappa) \sim \kappa^{-5/3}$. Moreover, the scales of the inertia range are independent of outer forces and are dominated by inertial rather than viscosity forces. Within the inertial range the energy is transferred from the large scales to the very small ones whereas the energy dissipates under the effect of the viscosity at high wavenumbers. Hence, the viscous effects damp the turbulent motion what results in a strong decrease in the energy spectrum. At these small scales the turbulent motion is independent of the outer forces and boundary conditions and can be assumed as locally isotropic.

Kolmogorov postulated that for large Reynolds numbers Re_L the energy spectrum $E(\kappa)$ will be universal for all flows and depends only on the kinematic viscosity ν and the turbulent energy dissipation rate ε. From similarity analysis it was shown, that the energy spectra reads

$$E(\kappa) = C_K \varepsilon^{2/3} k^{-5/3} \tag{2.41}$$

whereas C_K is the Kolmogorov constant which is estimated from experiments and simulations as $C_K = 1.5$. Kolmogorov postulated that the generation of turbulence energy happens on length scales which are much larger than the dissipative length scales. This assumption is valid for high Reynolds number flows and was confirmed for a wide range of turbulent flows. Low Reynolds number flows show another behavior. The wall acts as limiter to the physical growth of the vortices, which are therefore spatially restricted and cannot become large length scales close to the wall. From the corresponding energy spectra it can be shown, that an inertial range do not exist close to the wall (Kim [50]).

2.4 Velocity and temperature boundary layers

The knowledge of the impact of surrounding walls is essential to understand the complex flow mechanism. From the physical point of view, the flow near a solid wall exhibits substantially different anisotropic structures than in the main flow. In this region, called boundary layer, the evolving scales determine the overall properties of flow behavior and heat transfer, especially when the surface is structured by macroscopic devices like dimples. Hence, a brief introduction is given to the boundary layer theory in terms of velocity and temperature.

Fig. 2.3 presents the development of a thermal and velocity boundary layer of the flow over a flat plate schematically. The fluid particles at the flat plate surface have a zero velocity due to the no slip condition and act as a retardant to reduce velocity of adjacent fluid particles in the vertical direction to the wall. The thickness of the velocity boundary layer δ is normally defined as the distance from the solid body to the point where the flow velocity U is 99% of the freestream velocity U_∞. The boundary layer thickness is a function of the length x and is growing rapidly downstream in x direction. Moreover, the velocity U varies normal to the plate through the boundary layer. Hence, the velocity gradients within the boundary layer are large which needs special treatment in numerical simulations and experiments.

If the flow in front of the plate has a temperature T_∞ different than the wall temperature T_W, a thermal boundary layer is evolving in addition to the velocity boundary layer. The fluid temperature varies from T_W at $y = 0$ to T_∞ far away from the wall.

Fig. 2.3 presents the evolvement of a temperature boundary layer of the flow over a flat plate with a constant wall temperature T_W.

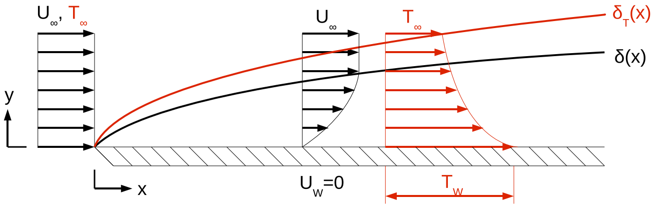

Fig. 2.3: Schematic profiles of the velocity and thermal boundary layer of a heated flat wall ($T_W = const$) with turbulent parallel flow.

The thermal boundary layer thickness δ_T is growing downstream in flow direction as it is the case of the velocity. The thickness of the thermal boundary layer δ_T is typically defined when the ratio

$$\frac{T_W - \overline{T}}{T_W - T_\infty} = 0.9 \tag{2.42}$$

is reached. The high temperature gradient close to the leading edge at the wall implies, that the resulting heat flux (see Eq. 2.5) is large in comparison to that of a expanded thermal boundary layer thickness δ_T further downstream. Hence, the heat flux decreases with the distance x from the leading edge.

A turbulent boundary layer of the velocity can be typically divided into three regions, the viscous sub-layer, the buffer-layer and the log-law or fully turbulent region, which are plotted on the semi-logarithmic axes presented in Fig. 2.4.

The turbulent boundary layer profiles for the velocity have been made dimensionless using the friction velocity u_τ calculated by the wall shear stress τ_w and viscosity

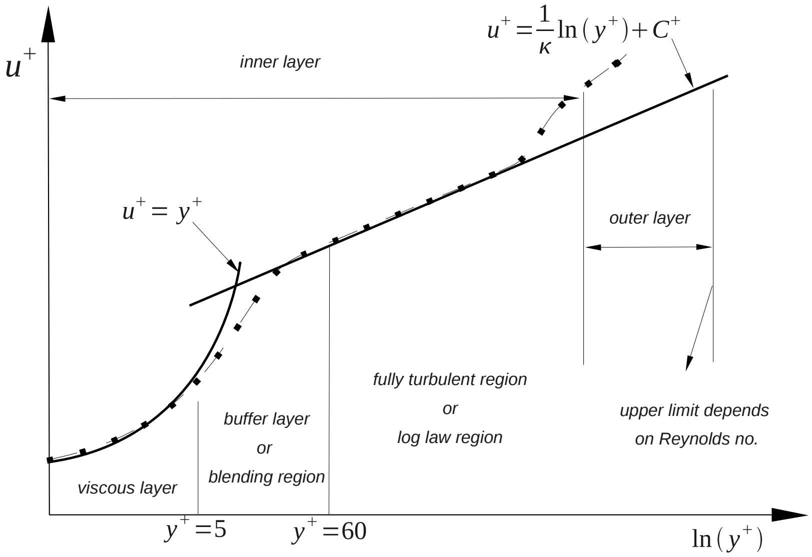

Fig. 2.4: Boundary layer profile for the velocity with schematic measurements.

ν as denoted by the superscript “+”. The wall shear stress can be defined as

$$\tau_W = \rho\nu \left.\frac{dU}{dy}\right|_W \tag{2.43}$$

to calculate the friction velocity from

$$u_\tau = \sqrt{\frac{|\tau_W|}{\rho}}. \tag{2.44}$$

The dimensionless coordinate y^+ normal to the wall and the dimensionless velocity u^+ can be estimated as

$$y^+ = \frac{u_\tau y}{\nu} \tag{2.45}$$

and

$$u^+ = \frac{U}{u_\tau} \tag{2.46}$$

respectively.

The boundary layer is called viscous sub-layer immediately adjacent to the surface $0 < y^+ < 5$ whereas the viscous effects are dominating and the turbulent fluctuations are negligible. A linear relation between the dimensionless velocity u^+ and dimensionless coordinate y^+ is valid in the viscous sub-layer.

$$u^+ = y^+ \tag{2.47}$$

The asymptotic behavior is universal for all turbulent flows near the wall. From $y^+ = 5$ up to $y^+ = 30$ the dependence of u^+ on y^+ transitions from linear to logarithmic variation. In this range, which is called buffer layer, the viscous and turbulent stresses are both in equilibrium. The log-law region extends from $y^+ > 30$ (Pope [80]) and is dominated by the effects of inertia forces. The principle distribution of the velocity is called log-law of the wall

$$u^+\left(y^+\right) = \frac{1}{\kappa} ln\left(y^+\right) + C^+, \tag{2.48}$$

where $\kappa = 0.41$ is the Kármán constant and C^+ is an integration constant which can be estimated from measurements for a smooth wall as $C^+ = 5$ (see Herwig [31]). An universal boundary layer profile for the temperature can be derived as it is in the case of the velocity. The temperature profile depends on heat conduction direct at the wall whereas convection processes are dominating in the outer region. Analogously to the friction velocity u_τ, a friction temperature can be defined as

$$T_\tau = -\frac{\dot{q}_W}{\rho c_p u_\tau} \tag{2.49}$$

for normalization. Using Eq. 2.4 it can be shown, that the friction temperature depends on the temperature gradient at the wall

$$T_\tau = -\frac{\nu}{\mathrm{Pr}} \frac{1}{u_\tau} \left.\frac{\partial \overline{T}}{\partial n}\right|_W . \tag{2.50}$$

Hence, the non-dimensional wall temperature Θ^+ can be written as

$$\Theta^+ = \frac{\overline{T} - T_W}{T_\tau}. \tag{2.51}$$

The temperature Θ^+ is zero direct at the wall whereas its profile in the viscous sub-layer ($y^+ < 5$) can be derived from the following equation (see Gersten [28])

$$\Theta^+\left(y^+, \mathrm{Pr}\right) = \mathrm{Pr} r\, y^+. \tag{2.52}$$

Thus, an universal logarithmic function for the temperature can be written as

$$\Theta^+\left(y^+, \mathrm{Pr}\right) = \frac{1}{\kappa_\Theta} ln\left(y^+\right) + C_\Theta^+\left(\mathrm{Pr}\right). \tag{2.53}$$

The constant κ_Θ is defined as $\kappa_\Theta = 0.41$ (Schlichting [83]). In contrast to the velocity, the temperature profile depends additionally on the Prandtl number Pr

$$C_\Theta^+\left(\mathrm{Pr}\right) = 13.7\mathrm{Pr}^{2/3} - 7.5 \qquad (\mathrm{Pr} > 0.5) \tag{2.54}$$

which has a major impact on the heat transfer.

2.5 Evaluation of heat exchangers

The basic equations the determine heat transfer in turbulent flows and especially its behavior at solid walls have been presented in the foregoing sections. When dimples are placed at the lower wall, the boundary layer profile will be disturbed since the surface depressions act as vortex generators. Hence, the heat transfer rates are increased. However, the disruption of boundary layer normally results in an increase of the overall flow resistance. Thus, it is evident that the designer of a new heat exchanger is focused to apply heat transfer augmentation devices with a low increase of the flow resistance to enhance the overall performance. This leads to the problem how to evaluate a heat exchanger in a physical correct sense. Therefore, a criterion has to be used which includes all relevant parameters which have impact on the overall performance. A detailed investigation of the different criteria is done by H. Herwig and his research group at the TU Hamburg-Harburg. Hence, only a short summary is given to make the reader familiar with the criteria used for calculation of the heat exchanger performance.

All criteria define the performance improvement of a modified heat exchanger relative to a standard heat exchanger. The commonly used criteria are based on the heat transfer rates, summarized by the Nusselt number Nu and overall flow resistance.

The flow resistance can be calculated in terms of pressure $\langle D_p \rangle$ and friction $\langle D_f \rangle$ force as

$$D_p = -\int_A p\overrightarrow{n}\,dA \tag{2.55}$$

$$D_f = \int_A \overrightarrow{\tau}\,dA, \tag{2.56}$$

where A, $\mathit{\Pi}$, $\overrightarrow{n}$ represent the surface area, mean pressure gradient and surface normal vector respectively. The non-dimensional resistance coefficient C_p and friction coefficient C_f are often used which can be formulated as

$$C_p = \frac{(\Delta p/\Delta x)}{0.5\rho u_b^2} \tag{2.57}$$

$$C_f = \frac{\tau_w}{0.5\rho u_b^2}\ . \tag{2.58}$$

In general, the design modifications to improve heat transfer rates involve an increase of the flow resistance inside the heat exchanger. Therefore, it seems to be reasonable to use the Nusselt number Nu and the flow resistance in terms of the fanning friction number ψ for evaluation of heat exchanger performance in a right way. The fanning friction factor is defined as

$$\psi = \frac{(\Delta p/\Delta x) \cdot D_h}{0.5 \rho u_b^2 L}. \tag{2.59}$$

Moreover, it is useful to evaluate the actual results in comparison to the results of the original heat exchanger (Nu_0,ψ_0). Hence, one of the most used criterion to establish heat exchanger performance is found through

$$f = \frac{Nu/\mathrm{Nu}_0}{\psi/\psi_0}\ . \tag{2.60}$$

A criterion is given by Gee and Webb [95],[26], who proposed the efficiency of a heat exchanger as

$$\zeta = \frac{Nu/\mathrm{Nu}_0}{(\psi/\psi_0)^{1/3}} \tag{2.61}$$

including the engine power within the term $(\psi/\psi_0)^{1/3}$ which is commonly known as thermo-hydraulic efficiency or thermo-aerodynamic performance. Further criterion like NTU (number of transfer units) can be found in the VDI Heat Atlas [92]. Nevertheless, the thermo-hydraulic criterion proposed by Gee and Webb [95],[26] is based on the first law of thermodynamics. In a thermodynamic sense this criterion is not useful and moreover it is not based on a clear physical background as it was shown by Kock [53]. Moreover, it was proposed that the thermodynamic and physical correct evaluation of the heat exchanger performance can be done by using the second law of thermodynamics in terms of entropy production rates. If the second law of thermodynamics is applied for a steady state flow with one inlet and one outlet, the entropy balance equation can be written as

$$\dot{m}(s_2 - s_1) = \frac{\dot{Q}}{T} + \dot{S}_{Pro}\ . \tag{2.62}$$

The changing of the entropy rate is based on the heat transfer through the boundaries $\frac{\dot{Q}}{T}$ and by entropy production inside the flow. It is well established, that the minimization of the entropy generation in any process leads to the conservation of useful energy. In reference to this work, entropy production $\dot{S}_{Pro}$ is generated due to irreversible dissipation of kinetic energy and heat transfer. Since entropy production is determined as irreversible, one part of usable energy called exergy is transferred to unusable energy, called anergy. It is called exergy loss in an energetic process and can be calculated as

$$\dot{E}_V = T_U \dot{S}_{Pro}. \tag{2.63}$$

The value T_U represents the environmental temperature. Hence, from an exergetic point of view, a heat exchanger is more efficient when the exergy loss is minimized.

A fundamental thermodynamic criterion to evaluate different heat transfer augmentation technique's using second law analysis has been proposed by Bejan [7], [8]. The aim is to minimize the entropy production and thus exergy loss in comparison to a defined reference case which is known as "thermodynamic optimization". Further Herwig et al. [32], [53] formulated the thermodynamic optimization method in combination with the RANS method and derived universal wall functions for the entropy production rates from asymptotic correlations. The method was proved to be correct and has been successfully applied to find the optimal designs of twisted tapes inside heat transfer pipes.

Despite the disadvantages of the criteria based on the first law analysis, the thermo-hydraulic performance is the most popular criteria to evaluate heat exchanger performance by engineers. Its main advantage is the direct connection to the points of interest: Nusselt number Nu and fanning friction factor ψ. Therefore, the application of the thermo-hydraulic performance will be used in this work to investigate the influence of dimples inside heat exchangers whereas the evaluation of dimples in terms of entropy production is done by Herwig et al. at the TU Hamburg-Harburg.

3 Modeling of turbulent motion and heat transfer

Computational Fluid Dynamics (CFD) is used in research and industry at every working process. The main part in this work is based on an instationary numerical method, known as Large Eddy Simulation (LES), to resolve all necessary vortex structures to determine the impact of dimpled surfaces on the flow field and heat transfer. In addition, steady state calculations (Reynolds-Averaged Navier Stokes (RANS) equations) for optimization process and basic analysis have been performed. The derivation of LES and RANS equations and their closure models are well described in the literature. Therefore, only a brief summary of the basic equations and discretization methods is given in this chapter. Further a short introduction to the framework OpenFOAM is appended.

3.1 Levels of flow simulation

Nowadays CFD is a very powerful method for simulation of complex flows. The field of CFD is widely spread on laminar / turbulent, compressible / incompressible, reacting, multiphase, visco-elastic and many other flows. It reduces the costs and time necessary for design and optimization of new machinery, allows to get a deep insight into flow behavior and diminishes the amount of experimental parameter studies. The most important questions is how to simulate the flow in complex geometries with a small numerical effort and a high accuracy. Fig. 3.1 presents the methods of flow simulation towards its precision and computational effort. The method with the highest precision and a huge computational effort is called Direct Numerical Simulation (DNS). The momentum Eq. 2.20 can be solved directly where all time and length scales of the turbulent flow (see Fig. 2.2) are fully determined. However, in the near future the DNS will be only applied to simple flow configurations of low Reynolds numbers and will be not useful for complex industrial applications (Pope [80]) due to its high computational effort. To overcome this disadvantage, the idea is to simplify the transport equations to a certain level where the numerical solu-

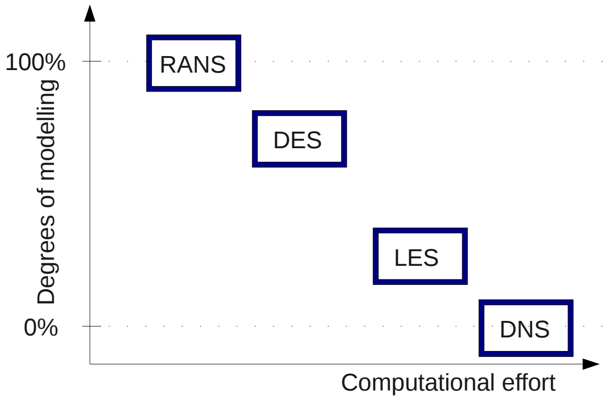

Fig. 3.1: Degree of turbulence modeling and computational effort.

tion time becomes realistic. Therefore, the LES is introduced. The basic idea is to resolve a large part of the three-dimensional turbulent motions and model so called small isotropic structures using Subgrid-Scale (SGS) models. The determination of the limit between large and small scale eddies is done by a filtering procedure. With the growing computational power the LES becomes more and more a mature technique to investigate unsteady flow phenomena in complex geometries. RANS method is a statistical approach in difference to the deterministic methods DNS and LES. The corresponding equations are derived by the application of Reynolds averging on the transport equations which includes that all turbulent lengthscales (shown in Fig. 2.2) have to be modeled. This approach leads to a fast numerical solution whereas the high impact of turbulence modeling could result in a low precision of the predicted fields when the grid resolution and used turbulence model are not well chosen. To combine the advantages from LES for the freestream flow and the advantages from RANS in the near wall area, the Detached Eddy Simulation (DES) can be used when the computational resources are not sufficient enough to apply the LES method to the whole domain.

3.2 Reynolds Averaged Navier Stokes equations

3.2.1 Reynolds averaging

The RANS equations are derived by application of Reynolds averaging to the governing equations described in section 2.2. The Reynolds averaging was introduced in section 2.3 (see Eq. 2.30) for turbulent flows. Due to the averaging process

$$\langle u_i'(\mathbf{x},t)\rangle \;=\; 0, \tag{3.1}$$

the information on fluctuations is lost and a time averaged solution of the flow fields is obtained. The continuity equation is written as

$$\frac{\partial\langle u_i\rangle}{\partial x_i} = 0 \tag{3.2}$$

and momentum equation as

$$\frac{\partial\langle u_i\rangle}{\partial t} + \frac{\partial\left(\langle u_i\rangle\langle u_j\rangle\right)}{\partial x_j} = -\frac{1}{\rho}\frac{\partial\langle p\rangle}{\partial x_i} + \frac{\partial}{\partial x_j}\left(\nu\frac{\partial\langle u_i\rangle}{\partial x_j} - \langle u_i' u_j'\rangle\right) + \langle f_i\rangle\ . \tag{3.3}$$

The energy transport equation (Eq. 2.24) yields to

$$\frac{\partial\langle T^+\rangle}{\partial t} + \frac{\partial\left(\langle u_i\rangle\langle T^+\rangle\right)}{\partial x_i} = \frac{\partial}{\partial x_i}\left(\frac{\nu}{\mathrm{Pr}}\frac{\partial\langle T^+\rangle}{\partial x_i} - \langle u_i' T^{+'}\rangle\right)\ . \tag{3.4}$$

Special attention has to be paid to the convective term of the momentum and energy equation. Due to the Reynolds averaging a new term appeared in Eq. 3.3 which is the unknown product of the fluctuating velocities $\langle u_i' u_j'\rangle$. It describes the effect of turbulent motion that have been filtered out by the averaging process and is called the Reynolds stress tensor. Analogously an unknown term appears $\langle u_i' T^{+'}\rangle$ in the energy transport equation which is called turbulent heat flux. Hence, with application of the Reynolds averaging new unknown values arise but no additional information or equations are derived. Thus, the system of transport equations is not closed. The presented turbulence models in the next section act therefore as closure models and are used to evaluate the turbulent stresses and turbulent heat flux in a time averaged form.

3.2.2 Closure models for RANS equations

A large number of turbulence models have been introduced over the last decades to close the system of the transport equations. The $k-\varepsilon-$Model (proposed by Launder and Spalding, Launder and Sharma [97]) and the $k-\omega$-SST-Model (proposed by Menter [74]) have been applied to simulate turbulent flows over dimpled surfaces. Both models are two-equation models which solve two additional transport equations and belong to the group of eddy viscosity models. Both models are based on the Boussinesq approximation to calculate the needed Reynolds stresses by a product of a single unknown value, the turbulent viscosity ν_t and the time averaged strain rate tensor $\langle S_{ij}\rangle$

$$\langle S_{ij}\rangle = \left(\frac{\partial\langle u_i\rangle}{\partial x_j} + \frac{\partial\langle u_j\rangle}{\partial x_i}\right)\ . \tag{3.5}$$

The Reynolds stresses are given as

$$-\langle u_i' u_j'\rangle = \nu_t\langle S_{ij}\rangle - \frac{2}{3}k\delta_{ij}\ . \tag{3.6}$$

It is obviously, that the modeling of the unknown stresses is replaced by the modeling of the turbulent viscosity ν_t. The determination of the turbulent viscosity ν_t for both models in case of incompressible flows is presented below.

$\mathbf{k}-\varepsilon-$Model The standard $k-\varepsilon-$Model includes two transport equations for the turbulent kinetic energy k and the turbulent dissipation rate ε to calculate the turbulent viscosity ν_t from dimensional analysis:

$$\nu_t = C_\mu \frac{k^2}{\varepsilon}, \tag{3.7}$$

using $C_\mu = 0.09$ as one of five model constants. The transport equation for k can be derived as

$$\frac{\partial k}{\partial t} + \langle u_j \rangle \frac{\partial k}{\partial x_j} = \frac{\partial}{\partial x_j}\left[\left(\nu + \frac{\nu_t}{\sigma_k}\right)\frac{\partial k}{\partial x_j}\right] + P_k - \varepsilon. \tag{3.8}$$

From left to right the terms represent the temporal deviation, the convection term, the diffusion term, the production rate

$$P_k = -\langle u_i' u_j' \rangle \frac{\partial \langle u_i \rangle}{\partial x_j}. \tag{3.9}$$

of the turbulent kinetic energy k (Wilcox [97]).

The transport equation of the dissipation rate ε can be derived as

$$\frac{\partial \varepsilon}{\partial t} + \langle U_i \rangle \frac{\partial \varepsilon}{\partial x_i} = \frac{\partial}{\partial x_j}\left[\left(\nu + \frac{\nu_t}{\sigma_\varepsilon}\right)\frac{\partial \varepsilon}{\partial x_j}\right] + C_{\varepsilon 1}\frac{\varepsilon}{k}P_k - C_{\varepsilon 2}\frac{\varepsilon^2}{k} \tag{3.10}$$

whereas the constants are defined as $\sigma_k = 1.0$, $\sigma_\varepsilon = 1.3$, $C_{\varepsilon 1} = 1.44$, $C_{\varepsilon 2} = 1.92$. The $k-\varepsilon-$ model shows good results for turbulent flow with no wall interaction since it is derived from the assumption of isotropic turbulence (Pope [80]). However, when the flow includes wall bounding, it can be shown that the $k-\varepsilon-$Model will fail to predict the correct stresses.

$\mathbf{k}-\omega$-SST-Model The $k-\omega$-SST-Model (SST-Shear Stress Model) was proposed by Menter [74] and can be interpreted as hybrid model which combines the $k-\varepsilon-$Model and $k-\omega$-Model to take advantage of both closure models. The $k-\omega$-SST-Model is applied inside the boundary layer whereas the $k-\varepsilon-$Model is used in the freestream flow. The transport equations of the turbulent kinetic energy k and specific dissipation rate ω can be written as (see Wilcox [97])

$$\frac{\partial k}{\partial t} + \langle u_j \rangle \frac{\partial k}{\partial x_j} = \frac{\partial}{\partial x_j}\left[(\nu + \sigma_k \nu_t)\frac{\partial k}{\partial x_j}\right] + P_k - \beta^* \omega k \tag{3.11}$$

$$\frac{\partial \omega}{\partial t}+\langle u_i \rangle \frac{\partial \omega}{\partial x_i}=\frac{\partial}{\partial x_j}\left[\left(\nu+\sigma_\omega \nu_t\right)\frac{\partial \omega}{\partial x_j}\right]+\frac{\gamma}{\nu_t}P_k-\beta\omega^2+2\left(1-F_1\right)\sigma_{\omega 2}\frac{1}{\omega}\frac{\partial k}{\partial x_j}\frac{\partial \omega}{\partial x_j}\ . \tag{3.12}$$

The switching between both turbulence models is realized using a blending function. The consideration of the transport of the turbulent shear stress yields to a modified calculation of the turbulent viscosity ν_t

$$\nu_t=\frac{a_1 k}{max\left(a_1 k;\Omega F_2\right)}\ . \tag{3.13}$$

For a detailed explanation of the constants and functions the reader is referred to Menter [75].

The $k-\omega$-SST-Model shows best results in comparison with other eddy viscosity turbulence models especially when wall bounding plays an important role. Nevertheless, the previous described closure models for RANS equations are proposed for high Reynolds number flows. The application of these models for low Reynolds number flows including wall bounding and heat transfer needs special treatment. The common approach of turbulence modeling near walls is usually done using wall functions (see sec. 2.4). Therefore, the first grid points have to be placed at a relatively large distance to wall in range of $y^+ = 30$ to $y^+ = 100$. The number of grid points will reduce significantly and nearly every turbulence model can be used in combination with wall functions. In contrast, it has been shown by Lai et al. [57] that wall functions show bad accuracy in flows with strong separation. Since in this work the turbulent flow over dimple curved surfaces including heat transfer has to be investigated, the application of wall functions is not trustful and will lead to wrong results (see Schnueckel [84]). Therefore, a low Reynolds number approach has been used to determine flow and temperature fields. The approach avoids the application of wall functions while solving the transport equations down to the wall. Hence, the first grid points have to be placed inside the viscous sublayer $y^+ \leq 5$ to capture the important flow features and to resolve the needed gradients for an accurate heat transfer prediction. It has to be ensured that the closure models are valid inside the viscous sublayer. This is usually done with the help of damping functions changing the responsible coefficients to obtain a satisfying solution near the wall. Otherwise the turbulent viscosity will be to high in the viscous sublayer due to its direct calculation from the shear stresses. However, the direct resolution of the near wall region has the disadvantage that the computational effort is much higher rather than using wall functions. Nevertheless, the investigated Reynolds numbers are moderate which allows the application of the low Reynolds number approach with a reasonable computational effort.

3.2.3 Modeling of turbulent heat transfer in RANS

The closure models for the momentum transport equation have been derived in the previous section. The modeling of turbulent heat flux for closure of the energy transport Eq. 3.4 is done analogously using the gradient transport hypothesis based on the Boussinesq approximation. Hence, the turbulent heat flux $\langle u_i' T^{+'} \rangle$ can be written as

$$-\langle u_i' T^{+'} \rangle = a_t \frac{\partial \langle T^+ \rangle}{\partial x_i} \qquad (3.14)$$

in analogy to the Fourier law (see Eq. 2.1). The coefficient a_t is referred as turbulent heat conduction coefficient and can be calculated as

$$a_t = \frac{\lambda_t}{\rho c_p} = \frac{\nu_t}{\mathrm{Pr}_t}, \qquad (3.15)$$

where ν_t is evaluated by the closure model from momentum transport and Pr_t is the turbulent Prandtl number. With assumption of constant material properties, the energy transport in terms of RANS can be formulated as

$$\frac{\partial \langle T^+ \rangle}{\partial t} + \frac{\partial \left(\langle u_i \rangle \langle T^+ \rangle \right)}{\partial x_i} = \frac{\partial}{\partial x_i} \left[\left(\frac{\nu}{\mathrm{Pr}} + \frac{\nu_t}{\mathrm{Pr}_t} \right) \frac{\partial \langle T^+ \rangle}{\partial x_i} \right] . \qquad (3.16)$$

The gradient diffusion approach in order to model the turbulent temperature flux is widely used due to its good performance, simplicity and numerical stability. However, it has to be noted that the assumption of a constant turbulent Prandtl number Pr_t is not correct since it varies with the flow properties and wall distance (Lyon [69]). Nevertheless, it has been shown that the approach works well for moderate Reynolds number flows and shows good results compared with empiric correlations.

3.3 Large Eddy Simulation

The LES is an intermediate technique in between the RANS and DNS method. The large scale structures are directly resolved whereas the effect of small scales is modeled. Since the small scales tend to be universal and homogeneous, the established models can be more unique and will require less adjustments for different flows as in comparison with RANS. A brief overview of the formulation of the LES equations and SGS models will be presented in the following sections.

3.3.1 Spatial Filtering

The separation of large and small scales is based on a filtering operation which is defined for an arbitrary variable ϕ in one dimension as

$$\overline{\phi}(x,t) = G * u = \int_{-\infty}^{+\infty} G(x-x')\phi(x',t)dx'. \tag{3.17}$$

The term G represents the filter function of the filter width $\overline{\Delta}$ and $*$ represents the convolution operator. The filtered variable $\overline{\phi}(x,t)$ can be formulated as spatial mean value and is denoted by an overbar

$$\phi(x,t) = \overline{\phi}(x,t) + \phi'(x,t). \tag{3.18}$$

The term ϕ' represents the fluctuation about the spatial mean value and includes all scales that are smaller than the filter width $\overline{\Delta}$. The value $\overline{\phi}(x,t)$ is commonly known as resolved part whereas $\phi'(x,t)$ as the unresolved part. The filter function can have different forms, like box or gaussian shape [80] whereas the box filter function in real space

$$G_B(x) = \begin{cases} \frac{1}{\overline{\Delta}} & \text{if } |x'| < \frac{1}{2}\overline{\Delta} \\ 0 & \text{otherwise} \end{cases} \tag{3.19}$$

is usually used in the Finite Volume Method (FVM). Box filtering is applied by using the underlaying grid with the grid space Δx_i as filter width $\overline{\Delta}$ for implicit low pass filtering of the variables. In most cases, e.g. for complex geometries, the used grid spacing is not homogeneous in all directions and thus the resulting nonuniform filter width will lead to commutation errors. It can be shown for uniform grids that the filter function G is only a function of $x - x'$ and differentiation and filtering commute. When non-uniform grids are used, commutation errors of second order $O(\overline{\Delta}^2)$ (Chosal [14]) are introduced. In consequence, it is difficult to separate numerical and filtering issues, e.g. numerical errors from the model performance. Nevertheless, it has to be noted that a filtered value will converge towards the unfiltered one as the filter width tends to be zero $\overline{\Delta} \rightarrow 0$. Thus, the LES converges to the DNS $\overline{u} \rightarrow u$ results when the filter width is getting smaller than the smallest scales (Kolmogorov scales in case of the velocity) of the flow.

3.3.2 Filtering of transport equations

The transport equations can be derived with application of the filtering operation on the governing equations in section 2.2. The LES equations of mass and momentum are written as

$$\begin{aligned}\frac{\partial \overline{u}_j}{\partial x_j} &= 0 && (3.20)\\ \frac{\partial \overline{u}_i}{\partial t} + \frac{\partial (\overline{u}_i \overline{u}_j)}{\partial x_j} &= -\frac{1}{\rho}\frac{\partial \overline{p}}{\partial x_i} + \frac{\partial}{\partial x_j}\left[\nu\left(\frac{\partial \overline{u}_j}{\partial x_i} + \frac{\partial \overline{u}_i}{\partial x_j}\right)\right] - \frac{\partial \tau_{ij}}{\partial x_j}. && (3.21)\end{aligned}$$

The derived filtered equations are identical with the unfiltered ones with exception of the term τ_{ij}. The tensor τ_{ij} is called SGS tensor and describes the influence of the unresolved small scales on the resolved large scales and is the result of the filtering operation applied on the convective term of the Navier-Stokes equation

$$\overline{u_i\, u_j} = \overline{u}_i\, \overline{u}_j + \tau_{ij}. \qquad (3.22)$$

The filtered temperature transport equation can be analogously written as

$$\frac{\partial \overline{T^+}}{\partial t} + \frac{\partial \overline{u_j}\overline{T^+}}{\partial x_j} = \frac{\partial}{\partial x_j}\left[\frac{\nu}{\mathrm{Pr}}\frac{\partial \overline{T^+}}{\partial x_j} - q_j\right]. \qquad (3.23)$$

Due to the filtering of the nonlinear convection term the unclosed term

$$\overline{u_j T^+} = \bar{u}_j\, \overline{T^+} + q_j \qquad (3.24)$$

arises. For closure of the filtered transport equations, SGS models have to be applied, which will approximate the influence of the small on the large scales in terms of $\overline{u_j T^+}$ and τ_{ij} using the filtered variables $\overline{u_i}$ and $\overline{T^+}$ respectively.

3.3.3 Closure models for LES

The functionality of the SGS models is analogously as it is in the case of RANS modeling. As main difference can be pointed out, that in case of LES the unclosed stresses represent a much smaller part of the turbulent energy spectrum. About 80% of the turbulent energy spectrum should be directly resolved within the LES. By Kolmogorovs first hypothesis, the behavior of the smallest scales is universal and as a result, it should be possible to construct a model applicable to all types of turbulent flows. Therefore, the introduced errors of the stresses from approximation using filtered values are less than in comparison to the modeled Reynolds stresses in RANS due to the uniqueness of the small scales, so that even simple SGS models could predict fairly good results for complex flows.

The Smagorinsky model proposed by Smagorinsky (1962) is one of the most used SGS models. It is based on the eddy viscosity assumption adopted from RANS modeling. The anisotropic residual stress tensor is modeled using the

Boussinesq approach which relates the residual and anisotropic stress to the resolved rate of strain

$$\tau_{ij}^{a} = \tau_{ij}^{Sgs} - \frac{1}{3}\tau_{kk}^{Sgs}\delta_{ij} = -2\,\nu_t\,\overline{S}_{ij} = -\nu_t\left(\frac{\partial \overline{u}_j}{\partial x_i} + \frac{\partial \overline{u}_i}{\partial x_j}\right). \tag{3.25}$$

The turbulent viscosity ν_t is determined using mixing length hypothesis from the filter length scale $\overline{\Delta}$ and a velocity scale $\overline{\Delta}|\overline{S}_{ij}|$ according to

$$\nu_t = (C_s\Delta)^2|\overline{S}_{ij}|\ . \tag{3.26}$$

The Smagorinsky constant C_s can be derived as $C_s = 0.17$ for turbulent homogeneous flows (see Pope [80]). However, the Smagorinsky constant C_s is a function of space and time for wall bounded flows and needs to be damped near the wall. Usually the van Driest damping function depending on the non dimensional normal wall coordinate y^+ is used

$$C_s(y^+) = C_0\left(1 - e^{-y^+/A^+}\right). \tag{3.27}$$

Another disadvantage besides the model constant C_s is that the dissipation is strictly positive ($C_s > 0$) which includes that no backscatter of the SGS kinetic energy can be considered. Nevertheless, the model is robust, effective and simple to apply since the turbulent viscosity ν_t can be added to the molecular viscosity ν which gives the effective viscosity $\nu_{eff} = \nu + \nu_t$.

The dynamic Smagorinsky model is an extension of the standard Smagorinsky model to estimate the constant C_s using a dynamic procedure introduced by Germano et al. [27]. Thus, the Smagorinsky constant C_s can be determined as a function of space and time $C_s(\mathbf{x}, t)$. The basic idea is to employ a second filter with a filter width $\hat{\Delta}$ which is set to the double length of grid scale $\hat{\Delta} = 2\overline{\Delta}$ denoted by $\hat{}$.

According to the Germano identity, the difference of both subgrid stresses can be calculated by taking the difference of T_{ij} and the test filtered tensor $\hat{\tau}_{ij}$

$$L_{ij} = T_{ij} - \hat{\tau}_{ij} = \widehat{\overline{u_i\,u_j}} - \hat{\bar{u}}_i\,\hat{\bar{u}}_j - (\widehat{\overline{u_i\,u_j}} - \widehat{\bar{u}_i\,\bar{u}_j}) = \widehat{\bar{u}_i\,\bar{u}_j} - \hat{\bar{u}}_i\,\hat{\bar{u}}_j\ . \tag{3.28}$$

The Germano identity can be applied to the original Smagorinsky model (Eq. 3.25).

$$L_{ij} = -2\,C_s^2\,\hat{\Delta}^2\,|\hat{\bar{S}}|\,\hat{\bar{S}}_{ij} + 2\,\widehat{C_s^2, \overline{\Delta}^2\,|\bar{S}|\,\bar{S}_{ij}} \tag{3.29}$$

which can be formally written as

$$L_{ij} = -2\,C_s^2\,M_{ij} \tag{3.30}$$

using the assumption that C_S is the same for the two different filter levels. To evaluate the model constant C_s^2, Lilly proposed a widely used procedure

$$C_s = -\frac{1}{2}\frac{L_{ij}\, M_{ij}}{M_{kl}\, M_{kl}}, \tag{3.31}$$

which is a least square solution minimizing the error $L_{ij} - 2C_s^2 M_{ij}$. Several authors suggested to apply a spatial averaging of C_s^2 in homogeneous directions to avoid large oscillations. Nevertheless, spatial averaging in homogeneous directions is not possible for complex geometries. The time averaging of the constant C_s is another option, but it is not consistent in respect to the Galilean invariance unless it is defined in a Lagrangian frame of reference (see Meneveau et al. [73]).

The dynamic mixed models have been developed to overcome the drawbacks of the eddy viscosity models (e.g. Smagorinsky model), which are not able to capture energy backscatter and normally overestimate the energy dissipation. The dynamic mixed models belong to the group of scale-similarity models and have been introduced first by Bardina et al. [6]. The SGS tensor is based on double filtering and can be formulated as

$$\tau_{ij} \approx \overline{\overline{u}_i\overline{u}_j} - \overline{\overline{u}}_i\overline{\overline{u}}_j \ . \tag{3.32}$$

The scale-similarity model underestimates the energy dissipation. Therefore, Zang et al. [101] proposed a mixed model which adds a dissipative part from the eddy viscosity model to enhance the dissipation. The increase of dissipation is captured by the Smagorinsky model within in the mixed model. Hence, the SGS tensor can be derived as

$$\tau_{ij}^{\mathrm{a}} = (\overline{\overline{u}_i\overline{u}_j} - \overline{\overline{u}}_i\overline{\overline{u}}_j)^a - 2(C_s^2\overline{\Delta})^2|\overline{S}|\overline{S}_{ij} \tag{3.33}$$

where $(\ldots)^a$ indicating the anisotropic part of the tensor. The similarity model represents the first part of the right hand side where the eddy viscosity model represents the last term of Eq. 3.33. Using the dynamic procedure proposed by Germano et al. [27] for the determination of the model constant C_s^2 in combination with the mixed models yields to

$$T_{ij}^{\mathrm{a}} = (\widehat{\overline{\overline{u}_i\overline{u}_j}} - \widehat{\overline{\overline{u}}}_i\widehat{\overline{\overline{u}}}_j)^a - 2(C_s\widehat{\overline{\Delta}})^2|\widehat{\overline{S}}|\widehat{\overline{S}}_{ij}. \tag{3.34}$$

Following the Germano identity is calculated by the difference of Eq. 3.34 and Eq. 3.33 as

$$L_{ij}^{\mathrm{a}} = T_{ij}^{\mathrm{a}} - \tau_{ij}^{\mathrm{a}} \tag{3.35}$$

which leads to

$$L^{\mathrm{a}}_{ij} = H^{\mathrm{a}}_{ij} + C_s^2 M_{ij} \tag{3.36}$$

whereas the tensor H_{ij} can be written as

$$H_{ij} = \widehat{\overline{\overline{u}}_i\overline{\overline{u}}_j} - \widehat{\overline{\overline{u}}}_i\widehat{\overline{\overline{u}}}_j \tag{3.37}$$

and the tensor M_{ij} as

$$M_{ij} = -2\widehat{\overline{\Delta}}^2\,|\widehat{\overline{S}}|\widehat{\overline{S}}_{ij} + 2\widehat{\overline{\Delta}^2|\overline{S}|\overline{S}_{ij}}, \tag{3.38}$$

respectively. To determine the model constant C_s^2, the least square method proposed by Lilly [63] is used which yields to

$$C_s^2 = \frac{M_{ij}(L^{\mathrm{a}}_{ij} - H^{\mathrm{a}}_{ij})}{M_{kl}M_{kl}}. \tag{3.39}$$

Nevertheless, the dynamic mixed model proposed by Zang et al. [101] is mathematically inconsistent using the grid filtered velocity to calculate the tensor T^{a}_{ij}. Vreman et al. [93] suggested an alternative method, henceforth called DMM, in a mathematical consistent way to express the scale-similarity and eddy viscosity part of the same filtering level in combination with the filtered velocity $\widehat{\overline{u}}$. Hence, the test filtered stress tensor might be written as

$$T^{\mathrm{a}}_{ij} = (\widehat{\overline{\widehat{\overline{u}}_i\widehat{\overline{u}}_j}} - \widehat{\widehat{\overline{u}}}_i\widehat{\widehat{\overline{u}}}_j)^a - 2(C_s\widehat{\overline{\Delta}})^2|\widehat{\overline{S}}|\widehat{\overline{S}}_{ij} \tag{3.40}$$

and the tensor H_{ij} changes to

$$H_{ij} = \widehat{\overline{\widehat{\overline{u}}_i\widehat{\overline{u}}_j}} - \widehat{\widehat{\overline{u}}}_i\widehat{\widehat{\overline{u}}}_j - (\widehat{\overline{\overline{u}_i\overline{u}_j}} - \widehat{\overline{\overline{u}}_i\overline{\overline{u}}_j})\ . \tag{3.41}$$

The dynamic calculation of the model constant is similar to Eq. 3.39. The values of C_s^2 vary strongly in space and can take on large magnitudes. In general, an averaging in homogeneous directions could be applied to stabilize numerical simulation. However, the application of spatial averaging is not possible in this work due to the complexity of the investigated dimple geometry. Kornev et al. [55] proposed a rigorous clipping procedure to prevent numerical instabilities.

However, it was found that using the DMM as *localized* DMM remains stable without a clipping procedure in the framework OpenFOAM. The constant C_s^2 was only bounded to be larger than zero and less than one ($0 \leq C_s^2 \leq 1$) to obtain no negative turbulent viscosity ν_t and to prevent numerical oscillations. But in contrast to the dynamic Smagorinsky model, the backscattering can be captured by the term $(\overline{\overline{u}_i\overline{u}_j} - \overline{\overline{u}}_i\overline{\overline{u}}_j)$ which leads to a fairly good agreement to DNS and experimental data especially when recirculation zones are present (Jahnke et al. [43]).

One-equation models are different compared to the eddy viscosity or scale similarity models. Within these models an additional transport equation is solved beside the filtered momentum equation, which takes the history and non local effects of the small scales into account. Solving the filtered transport equation for the residual kinetic energy in combination with an eddy viscosity approach leads to calculation of the turbulent viscosity ν_t (Chosal et al. [14]). The transport equation for residual kinetic energy is adopted from RANS closure models which can be formally written as

$$\frac{\partial k_{\mathrm{r}}}{\partial t} + \frac{\partial}{\partial x_j}(\overline{u}_j k_{\mathrm{r}}) = \frac{\partial}{\partial x_j}\left[(\nu + \nu_{\mathrm{r}})\frac{\partial k_{\mathrm{r}}}{\partial x_j}\right] + \mathcal{P}_{k_{\mathrm{r}}} - \varepsilon_{k_{\mathrm{r}}}. \tag{3.42}$$

The term $\mathcal{P}_{k_{\mathrm{r}}}$ represents the production and $\varepsilon_{k_{\mathrm{r}}}$ is the rate of viscous dissipation of the residual kinetic energy k_{r}. Hence, the turbulent viscosity can be calculated using the eddy viscosity approach as

$$\nu_{\mathrm{r}} = C_k k_{\mathrm{r}}^{1/2}\overline{\Delta}\,. \tag{3.43}$$

3.3.4 Modeling of turbulent heat transfer in LES

The spatial filtering of the energy transport equation leads to the term q_j which needs to be modeled. The turbulent heat flux is modeled by a gradient diffusion approach similar to the closure models in case of RANS (see section 3.2.3). It should be noted, that the model is mathematically in analogy to the Fouriers law of heat conduction. The turbulent heat flux q_j can be written as

$$q_j = -D_t\frac{\partial\overline{T^+}}{\partial x_j}\,, \tag{3.44}$$

where D_t is the turbulent diffusion coefficient which can be calculated using the turbulent viscosity ν_t and turbulent Prandtl number Pr_t from

$$D_t = \frac{\nu_t}{\mathrm{Pr}_t} = \frac{(C\overline{\Delta})^2|\overline{S}_{ij}|}{\mathrm{Pr}_t}\,. \tag{3.45}$$

The constant C is equal to the Smagorinsky constant C_s and is determined using the dynamic procedure of Germano et al. [27] as described in the previous section.

Numerical calculations using LES in this work have shown, that the calculated heat flux in LES can be predicted more accurately when using a dynamically determination of the turbulent Prandtl number Pr_t in space and time (Lilly [63]).

The Germano identity for the heat fluxes reads

$$L_{T^+j} = \widehat{\overline{u}_i\overline{T^+}} - \widehat{\overline{u}}_j\widehat{\overline{T^+}} \tag{3.46}$$

and the tensor M_{T^+j}

$$M_{T^+j} = -\widehat{\overline{\Delta}}^2|\overline{S}_{ij}|\frac{\partial\widehat{\overline{T^+}}}{\partial x_j} + \overline{\Delta}^2\widehat{|\overline{S}_{ij}|\frac{\partial\overline{T^+}}{\partial x_j}}. \tag{3.47}$$

The model constant C can be determined within the dynamic procedure of Germano in combination with the dynamic Smagorinsky model and can be further used to calculate the turbulent Prandtl number in space and time as

$$\frac{1}{\mathrm{Pr}_t} = \frac{1}{C}\frac{M_{T^+j}L_{T^+j}}{M_{T^+j}M_{T^+j}} \ . \tag{3.48}$$

In addition, the methodology of the dynamic mixed model proposed by Vreman et al. [93] is adopted to evaluate the turbulent heat flux q_j which can be derived from

$$q_j = \overline{\overline{u}_j\overline{T^+}} - \overline{\overline{u}}_j\overline{\overline{T^+}} - \frac{\nu_t}{\mathrm{Pr}_t}\frac{\partial\overline{T^+}}{\partial x_j} \ . \tag{3.49}$$

In case of the dynamic mixed model, the Prandtl number Pr_t is defined in the same manner as shown above

$$\frac{1}{Pr_t} = \frac{1}{C}\frac{M_{T^+j}(L_{T^+j} - H_{T^+j})}{M_{T^+j}M_{T^+j}}, \tag{3.50}$$

where the tensor H_{T^+j} can be calculated as

$$H_{\phi j} = \widehat{\overline{\widehat{\overline{u}}_j\widehat{\overline{T^+}}}} - \widehat{\overline{\widehat{\overline{u}}}}_j\widehat{\overline{\widehat{\overline{T^+}}}} - \widehat{\overline{\overline{u}_i\overline{T^+}}} + \overline{\overline{u}}_j\ \widehat{\overline{\overline{T}}^+} \tag{3.51}$$

and M_{T^+j} from Eq. 3.47 and L_{T^+j} from Eq. 3.46. Normally the constant C and the turbulent Prandtl number will be averaged in homogeneous directions to avoid large oscillations. Since in this work no spatial averaging was possible due to the complexity of the dimple, the turbulent thermal diffusivity was bounded to $D_t \geq 0$ to keep the numerical process stable. Moreover, it has been shown in this work that the application of the DMM for the unresolved stresses and turbulent heat flux shows very good agreement with empiric correlations and DNS results published in literature.

3.4 Numerical methodology

There are existing various methods like Spectral methods, Finite-Element-Method (FE) or Finite-Volume-Method (FVM) to solve the governing equations numerically. Spectral methods and FE methods are based on the idea to approximate the solution by predefined functions. The approximation in done by a linear combination of continuous functions (like Chebyshev polynomials) for the Spectral method whereas continuous functions for sub-domains are piecewise used for the FE method. Spectral methods can reach a high accuracy when the investigated domain is fairly simple and the solution is smooth. FE methods can be applied for complex geometries, but reveal a low accuracy and do not guarantee the conservation of mass in the domain which is important in case of fluid dynamics. Thus, the FVM, which is based on the integral formulation over sub-domains, is mostly used for CFD to ensure conservation laws on complex geometries with a satisfied accuracy. The spatial and temporal discretization has been studied thoroughly during the last decades. Therefore, only a brief summary of the spatial and temporal discretization technique will be schematically presented using a generic transport equation of the transported variable ϕ (e.g. mass, velocity) which reads

$$\frac{\partial \rho\phi}{\partial t} + \frac{\partial \rho u_i \phi}{\partial x_i} - \frac{\partial}{\partial x_i}\left(\rho\Gamma_\phi \frac{\partial \phi}{\partial x_i}\right) = S_\phi(\phi)\ . \tag{3.52}$$

The Eq. 3.52 can also be written in symbolic form using Nabla operator ∇ and velocity vector U as

$$\underbrace{\frac{\partial \rho\phi}{\partial t}}_{Temporal} + \underbrace{\nabla\cdot(\rho U\phi)}_{Convection} - \underbrace{\nabla\cdot(\rho\Gamma_\phi\nabla\phi)}_{Diffusion} = \underbrace{S_\phi(\phi)}_{Source}\ . \tag{3.53}$$

Due to the second derivative of the diffusion term, the nonlinear PDE requires discretization of at least second order to represent the terms with a satisfied accuracy. The discretization of each term is roughly presented.

The convective term of the transport equation is discretized using its integral formulation. The approximation of the convective volume flux through the faces is defined as

$$\int_V \nabla\cdot(\rho U\phi)dV = \int_A dA\cdot(\rho U\phi) \tag{3.54}$$

$$= \sum_f (\rho U)_f \phi_f \tag{3.55}$$

$$= \sum_f F\phi_f\ , \tag{3.56}$$

whereas F is the flux over the surface A of the control volume. The values ϕ_f at the surface A have to be determined using the cell values ϕ_P and ϕ_N of the neighbour cells. Thus, the value ϕ_f is determined by a linear interpolation (CDS) of the values of the neighbour grid points as

$$\phi_f = \phi_N \gamma_f + \phi_P (1 - \gamma_f) \ , \tag{3.57}$$

where the interpolation factor is defined by the distance of the neighboring cells as

$$\gamma_f = \frac{x_f - x_P}{x_N - x_P} \tag{3.58}$$

for a one dimensional case. The convective part dominates the flow and heat transfer at high Reynolds numbers. Therefore, it is very important to reduce numerical errors due to interpolation. It can be shown by Taylor series expansion of ϕ around the point P, that the CDS is of second order accuracy and can be applied for structured and unstructured meshes. Nevertheless, the CDS can reproduce large numerical oscillations when the gradients are not sufficiently resolved. One way to avoid large oscillations is to use first order schemes like the Upwind Differencing Scheme (UDS). The UDS can be used in terms of RANS but for LES it is problematic, since the flow fields will be drastically smoothed due to an increasing diffusion which can be fairly higher than the modeled turbulent diffusion. An elegant way to avoid numerical oscillations is the usage of TVD (Total Variation Diminishing) schemes which are a blend of UDS and CDS. Nevertheless, the CDS is used in combination with a sufficient fine mesh in this work which is the simplest way to prevent numerical oscillations.

The diffusive term of the transport equation can be derived from the integral formulation wit a linear variation of ϕ as

$$\int_V \nabla \cdot (\rho \Gamma_\phi \nabla \phi) dV = \int_A dA \cdot (\rho \Gamma_\phi \nabla \phi) \tag{3.59}$$

$$= \sum_f (\rho \Gamma_\phi)_f A_f \cdot (\nabla \phi)_f \ . \tag{3.60}$$

As it can be seen, the approximation of the diffusion term requires the value of normal derivatives of ϕ at the surfaces of the control volume. The gradient of ϕ can be calculated by the values at the grid points P and N of the neighboring cells for an orthogonal grid as

$$A_f \cdot (\nabla \phi)_f = A \, \frac{\phi_N - \phi_P}{\Delta c} \ , \tag{3.61}$$

whereas Δc is the length vector between the two grid points. For non-orthogonal meshes an explicit correction term has to be introduced which is described in detail by Ferziger [20].

The source term of the transport equations cannot be classified as convective, diffusive or temporal term. It is discretized and linearized as

$$S_\phi(\phi) = S_u + S_p\phi, \tag{3.62}$$

whereas S_u and S_p can be a function of ϕ. Hence, the source term can be written in the following way

$$\int\limits_V S_\phi(\phi)dV = S_uV + S_pV\phi_f. \tag{3.63}$$

The temporal discretization has to be at least at the same order as for the spatial derivatives in case of LES. The transport equations are filtered implicit in time. At a glance no restrictions are given to the applied time step as it is in the case of an explicit time discretization which is restricted to the Courant Friedrich Levy (CFL) criteria to ensure numerical stability

$$Co = \frac{\Delta t\,|u|}{\Delta x}. \tag{3.64}$$

The Backward Differencing (BD) method is applied in this work which can be derived using Taylor expansion at different time levels at the new time instant

$$\frac{\partial\phi}{\partial t} = \frac{3\phi^n - 4\phi^{n-1} + \phi^{n-2}}{2\Delta t} \tag{3.65}$$

whereas the CFL number is kept below one (CFL$\leq$ 1) to prevent numerical oscillations caused by CDS.

The pressure is normally derived from the equation of state and is a function of the density ρ and temperature T. Since for the incompressible case no equation for the pressure exists and no time derivative for the pressure can be calculated, the pressure becomes uncoupled and act as source term in the momentum equation. Therefore, the PISO (Pressure Implicit with Splitting of Operators) algorithm is used in the this work to couple the pressure to the velocity. In the first step, the momentum equations are solved with a predefined pressure. The calculated velocity field from the predefined pressure will not satisfy the equation of mass. Thus, an iteration process is introduced to drive the local velocity and pressure field towards one, that satisfies the continuity equations.

3.5 OpenFOAM

The framework OpenFOAM (Field Operation And Manipulation), released by OpenCFD Ltd under GNU Public License, has a aroused great interest especially for research groups in the last years and is used at the University of Rostock from the beginning of its public release. The simulation toolkit for continuum mechanics is based on object oriented language C++ and can be applied to a great variety of physical challenging tasks in engineering. In the author's opinion, the main advantage of OpenFOAM is the free access to the source code. Due to the clear syntax and structure of OpenFOAM one can easily add or delete terms to understand their impact on the numerical solution. Turbulence models, boundary conditions etc. can be easily implemented using the present source and existing base classes in OpenFOAM.

To show one example, the temperature transport equation in terms of RANS (see eq. 3.16) can be written in OpenFOAM syntax as

```
 fvScalarMatrix TEqn
(
    fvm::div(phi,T)
  - fvm::laplacian((nu/Pr+turbulence->nut()/Pr_t), T)
);
TEqn.solve();
```

which shows the simpleness of implementation in OpenFOAM. The definition of field values shows major advantage in data handling in comparison to the cell based structure in Fortran code's like FLOWSI. OpenFOAM is fully parallelized using MPI environment to run the solution processes on an arbitrary number of processors. Another important feature is the handling of different types of meshes which can either be generated in OpenFOAM itself or can be imported from 3rd party software e.g. IcemCFD. At time the code OpenFOAM is well established in research and industry and is used for numerical simulations in this work.

4 Proper Orthogonal Decomposition

The results of the processed data are commonly analyzed by visualizing snapshots and time averaged fields of the current flow field to determine main flow characteristics. However, there are existing methods which allow a more detailed analysis of the instantaneous fields recorded from experiments or numerical simulations to extract important mechanism which cannot be seen in a time averaged field. One of the most efficient tools for extraction of coherent structures is the Proper Orthogonal Decomposition method (POD). The POD method has been implemented into the framework OpenFOAM for flow fields calculated by LES to investigate the role of coherent structures over dimpled surfaces and their influence on the heat transfer mechanism.

4.1 Coherent structures

Since coherent structures play a significant role in the scalar and momentum transport, mixing processes and acoustics, the importance to detect and understand coherent structures has not to be further explained. In general, the anisotropic vortices arising from the wall in turbulent flows have small time and length scales, however, under special conditions (e.g. other surface structure) large scale coherent structures may occur inside the flow domain. Coherent structures are detected in a large variety of turbulent flows like hairpin vortices inside the boundary layer or vortex rollups inside turbulent shear flows (Balares [5], Roshko[82]). They can be defined as patterns of vortical motion which are clearly distinguished from the turbulent background (see Hussain [36]). The role of coherent structures have been thoroughly investigated and summarized by several authors (see Fiedler [23], Hussain [36], Roshko [82]). To study its interaction with the small scale (background) turbulence and interactions with each other, mathematical methods like the POD method have to be developed.

Detection of vortices

Since coherent structures contain of at least one vortex, the question *how to identify coherent structures* can be forwarded to the question *what is a vortex* (see Hussain [36]). The question is neither single or unique. Lugt [65] defined a vortex as a rotating motion of many particles around a common center. The definition implies that a vortex consists of closed streamlines. However, the vortex definition by Lugt [65] has been clearly analyzed and discussed by Jeong and Hussain [44], who further give a clear overview of the main methods to indicate a vortex. Since there exists a velocity gradient along the vortex radius it seems to be reasonable to use pressure isosurfaces to indicate the core of the vortex. Jeong and Hussain [44] showed several conditions where the pressure minimum will not identify the vortex core or will indicate other flow phenomena which cannot be characterized as a vortex. Nevertheless, the pressure isosurfaces give a first impression about the local flow characteristics. The most popular method for vortex identification is to calculate the vorticity field which can be defined as

$$\omega = \nabla \times U = \epsilon_{ijk} \frac{\partial u_k}{\partial u_j} \; . \tag{4.1}$$

Mainly the vorticity method can be applied to free flows. If wall bounding is applied (as in the presented work), the maximum vorticity will occur close to the wall since the strongest velocity gradients are found at the wall. Due to the fact that the vortex core can not be present direct at the wall, the method is not suitable for wall bounded flows. Jeong and Hussain [44] introduced two requirements for other vortex identification methods:

1. Vortex cores must have a net vorticity and a net circulation, so that potential vortices are excluded.
2. The extracted geometry of the vortex core has to be Galilean invariant.

It should be mentioned, that the above mentioned criteria (pressure isosurfaces and vorticity) do not satisfy the proposed requirements. An improved method to identify vortices which fulfill the proposed requirements was given by Hunt et al. [35] called $Q - criterion$. It is based on the application of the velocity gradient decomposition

$$\frac{\partial u_i}{\partial x_j} = S_{ij} + \Omega_{ij} \tag{4.2}$$

where S_{ij} is the strain rate tensor and Ω_{ij} the vorticity tensor. The $Q - criterion$ defines a vortex as a three dimensional region

$$Q = \frac{1}{2}[|\Omega_{ij}|^2 - |S_{ij}|^2] \geq \ 0 \tag{4.3}$$

where the norm of the vorticity tensor Ω_{ij} is larger than the norm of the strain rate tensor S_{ij}.

The most popular criteria for vortex identification is the $\lambda_2 - criterion$ proposed by Jeong and Hussain [44]. It is based on the search of the local pressure extrema across the vortex. The derivatives of the pressure (hessian matrix p_{ij}) are calculated by taking the gradient of the momentum equations and decomposing it into a symmetric and asymmetric part which yields to the vorticity transport equation

$$\frac{DS_{ij}}{Dt} - \nu S_{ij,kk} + \Omega_{ik}\Omega_{kj} + S_{ik}S_{kj} = -\frac{1}{\rho}p_{ij} \ . \tag{4.4}$$

If a local pressure minimum is present in a plane across the vortex, two negative eigenvalues of the pressure hessian matrix exist. By removing the unsteady irrotational straining term DS_{ij}/Dt and the viscous effects (since they have no impact to indicate vortices) from the equation above, a vortex is defined as a connected fluid region with two negative eigenvalues of $(S_{ij} + \Omega_{ij})$. There are only existing real eigenvalues because the sum of both tensors is symmetric. When the eigenvalues are ordered in terms of $\lambda_1 \geq \lambda_2 \geq \lambda_3$ one can define a vortex if the second eigenvalue λ_2 is less than zero.

Using the above named criteria for vortex identification, the characteristic vortices can be extracted for turbulent flows. Jeong and Hussain [44] showed that the $\lambda_2 - criterion$ and $Q - criterion$ work fairly well for wall bounded flows since they fulfill the Galilean invariance and have a net circulation. The best and well-known example for their performance is the extraction of so called *streaks* arising in the laminar sublayer for the turbulent flow in a plane channel. A detailed analysis of the streaks inside turbulent boundary layers was done by Jeong et al. [45], who showed that the streaks are unstable and thus have a particular influence in the formation the turbulent flow over wall bounded flows. Especially the impact of the streaks can be seen in the resulting heat flux distribution on the heated/cooled channel walls respectively.

One of the newest method to identify vortex structures is proposed by Haller et al. [30] using Lagrangian particle transport. Haller et al. [30] proposed to calculate the Finite Time Lyapunov Exponent from the particle trajectories to indicate the separation rate of the nearest particle paths. It characterizes the separation of particles over time providing a Galilean invariant Lagrangian view.

Today there exist a huge variety of criteria besides the above mentioned vortex criteria. The evaluation of vortex identification criteria within numerical simulations by comparing the resulting vortex patterns does not show an universal correct choice of one of the criteria. Wu et al. [99] mentioned that the extraction of vortex formations in turbulent flows depends on the intuitive and subjective view of the investigator.

4.2 Introduction to POD

POD is an elegant method to extract and order characteristic structures in terms of energy content of a three dimensional flow field. The method is commonly known as Principle Component Analysis (PCA) or Single Value Decomposition (SVD) and was firstly introduced by Karhunen [46] and Loève [64]. Lumley [66], [67], [68] proposed the POD as an objective tool to extracted structures ordered in terms of energy in extension to fluid dynamics. A detailed review and proof of the POD method have been done by Berkooz et al. [10], Holmes [34] and Aurby et al. [3], [2]. To study the dynamics of turbulent motion, the POD technique was firstly applied by Berkooz et al. [10], [9] and Sirovich et al. [85]. It has been thoroughly used to extract structure dynamics for turbulent shear flows by Kirby et al. [51] and Manhart et al. [72], for turbulent mixing layers by Lewalle et al. [58] and for turbulent channel flow by Moin et al. [76]. Due to its high computational requirements, the POD technique become popular in last ten years and is now a commonly used post-processing tool for detailed analysis of the flow phenomena. At time, the POD has been applied to many different flow fields obtained from experiments and numerical simulation to get a deep insight into flow physics and is present in a wide range of engineering problems.

4.3 Mathematical backround

The implementation of the POD method using flow fields from LES into the framework OpenFOAM has been done according to Manhart et al. [72] and Chatterjee [13]. The flow fields, e.g. velocity field $u_i(\mathbf{x}, t)$, are determined from numerical simulation by LES. The flow fields from LES at a limited number of time steps are stored at the hard disk which leads to the discrete POD method. For post processing e.g. the velocity field is decomposed into orthogonal base functions $\Phi_i^{(n)}(\mathbf{x})$ in space and uncorrelated temporal coefficients $a^{(n)}(t)$. Thus, the velocity field $u_i(\mathbf{x}, t)$ at each time step can be reconstructed by a linear combination of the eigenmodes and time coefficients as

$$u_i(\mathbf{x},t) = \sum_{n=1}^{N} a^{(n)}(t)\Phi_i^{(n)}(\mathbf{x}) \; . \tag{4.5}$$

The number (n) is equal to the number of modes extracted by the POD method which is the number of time instants used for decomposition in the discrete case. Lumley [68] proposed that the base functions $\Phi_i^{(n)}(\mathbf{x})$ can be calculated from the eigenvalue problem

$$\int\int\int_V R_{ij}(\mathbf{x},\mathbf{x}^{'})\Phi_j^{(n)}(\mathbf{x}^{'})d\mathbf{x}^{'} = \lambda^{(n)}\Phi_i^{(n)}(\mathbf{x}^{'}). \tag{4.6}$$

The term $R_{ij}(\mathbf{x},\mathbf{x}^{'})$ denotes the spatial correlation tensor which can be evaluated as

$$R_{ij}(\mathbf{x},\mathbf{x}^{'}) = \frac{1}{T}\int_T u_i(\mathbf{x},t)u_j(\mathbf{x}',t)dt \; . \tag{4.7}$$

In case of decomposing fields with a large number of discrete information (stored values at grid points) with a limited number of time instants it is efficient to compute the correlation tensor at a first step. Therefore, Sirovich [85] proposed the method is called 'method of turbulent snapshots' which yields the eigenvalue problem with the temporal correlation tensor $C(t,t^{'})$ in the form of

$$\int_T C(t,t^{'})a^{(n)}(t^{'})\; dt^{'} = \lambda^{(n)}a^{(n)}(t) \; . \tag{4.8}$$

The flow fields are collected and stored in matrix form for evaluation of the temporal correlation tensor $C(t,t^{'})$

$$C(t,t^{'}) = \int\int\int_V u_i(\mathbf{x},t)u_i(\mathbf{x},t^{'})d\mathbf{x}^{'} \; . \tag{4.9}$$

Since the form of the temporal correlation tensor is positive definite, the estimated eigenvalues are positive and the eigenvectors are orthogonal to each other. Hence, the obtained eigenvectors represent the orthogonal base functions (eigenmodes)

$$\Phi_i^{(n)}(\mathbf{x}) = \frac{1}{T}(\lambda^{(n)})^{-1}\int_T a^{(n)}u_i(\mathbf{x},t)dt \; . \tag{4.10}$$

The factor $1/T$ can be ignored in the discrete case, since it changes only the absolute values whereas the relative magnitudes remain equal. From a physical point of view, the mathematical property of orthogonality of the spatial and temporal modes

$$\int\int\int_V \Phi_i^{(n)}(\mathbf{x})\Phi_i^{(m)}(\mathbf{x}) = 0 \quad \text{if } n \neq m, \tag{4.11}$$

means, that the modes are uncorrelated which gives the possibility to investigate the spatial and temporal behaviour of the modes independent from each other.

Two advantages of the POD method can be pointed out. First the shape of each mode is evaluated by the POD method and is not predefined as for the wavelet analysis. Second the modes can be ordered in terms of energy content, which shows the impact of each mode for the reconstruction process of the original flow field. The time averaged energy content of each POD mode n can be calculated by its eigenvalue $\lambda^{(n)}$ which is derived from

$$\langle (a^{(n)})^2 \rangle = \lambda^{(n)}. \tag{4.12}$$

The sum of all eigenvalues represents the total turbulent kinetic energy in case of the velocity (under condition that the mean value is subtracted from the corresponding field). The collective contribution of the first N modes to the overall energy can be estimated as

$$q_N = \frac{\sum_{n=1}^{N} \lambda^{(n)}}{\sum_{n=1}^{M} \lambda^{(n)}} \tag{4.13}$$

where q_N is the sum of N eigenvalues referred to the total sum of all M positive eigenvalues. The error level of the reconstructed flow using the first N modes is estimated as $1 - q_N$. To solve the eigenvalue problem of Eq. 4.8, Octave libraries are linked directly to the OpenFOAM code for fast computation.

4.4 Application of POD at discrete fields

Before the POD method can be applied, the importance of the total time period T in Eq. 4.8 has to be pointed out. If POD is used to obtain a clear physically description of long term fluid motions, then the data should be collected over a sufficient time period which is longer than the time scale of the inherent dynamics of the flow. Therefore, one has to be careful to determine the total time interval of the averaging time when the flow dynamics are not quit clear.

In terms of LES the calculated fields are not stored at every time step. They are written to hard disk only at predefined equidistant time steps ΔT to reduce computational time and to keep disk resources at a low level. The choice of the time step ΔT should also be done carefully. It has to be ensured that the stored fields capture all relevant flow physics including all important time scales in order to keep errors of the POD analysis small.

In general, the fields used for POD are subtracted by their mean values to estimate the autocorrelation matrix. When the mean fields are not subtracted, the first POD mode $\Phi_i^{(1)}(\mathbf{x})$ represents the time averaged flow field (if the averaging time instants were long enough to capture the steady state solution). Then the second mode

contains the most energy in comparison to all higher modes but is orthogonal to the first mode. Thus, one can imagine that the starting coordinate system will be totally different compared to the case when the mean field are not subtracted due to the orthogonality of the modes. However, from rigorous mathematical description it can be shown that mean value have to be substracted from the current field, since the aim of the POD method is to search for the efficient mode to capture the most kinetic energy in terms of least mean squares. Since the analysis of the fluctuating pressure and velocity values is in the foreground in this work, the mean value is subtracted from each snapshot.
The following example is given to underline the necessary computational resources for POD. The number of grid points m is assumed at $3 \cdot 10^6$ and the saved time instants N at 10^3. Hence, the calculation of the eigenvalues of the matrix $m \times N$ with over $3 \cdot 10^9$ components is found to be very time and memory consuming. However, the autocorrelation matrix is directly evaluated from fields using the OpenFOAM syntax which reduces the computational time enormously. In order to reduce computation time additionally, only a part of the domain (like a box around the dimple) can be used to focus the POD on the space of interest.

4.5 Interpretation of POD modes

Since the POD analysis is based on a full mathematical procedure for decomposition of collected data, the interpretation of the physical meaning of the different POD modes and time coefficients for turbulent flow fields have to be reviewed. Several advantages and disadvantages can be pointed out if the discrete flow fields from LES are used for decomposition. Time resolved flow fields with a high spatial resolution are obtained from LES which give a deep insight into the presence of large and small scale eddies. Nevertheless, the visualization of large scale coherent structures using the methods described in section 4.1 are not straight forward. In most cases, the evolving structures include large time scales which cannot be clearly visualized using vortex extraction methods like the $\lambda_2 - \mathit{criterion}$ at single timesteps. The POD analysis combines the extension of coherent structures in space *and* time and focus on the energy content of the structures inside the flow field. It projects the snapshots of the flow field onto an orthogonal dynamical system of time independent of not predefined base functions which are sorted in terms of energy content. But it has to mentioned, that one eigenmode does not represent the physical flow field like e.g. streamlines. The original flow field can only be reconstructed by a linear combination with the temporal time coefficients. However, if the energy distribution decays rapidly over the number of modes, it can be assumed, that the first modes can be used to represent to flow field (commonly known as low order reconstruction). A rapid decay of the energy content is found in flows with a high regularization and dominant structures like turbulent mixing layers whereas highly chaotic flows show a slow decay in the energy content. Therefore, the POD is preferable for interpretation when the first POD modes include a high amount of the total energy. In addition it has to be noted, that no adjustable constants or mode structures are predefined like it is done for the wavelet analysis. One disadvantage of the method is the high amount of computational resources. Especially the hard disk storage is very large if one imagines that for POD of the velocity field 5000 snapshots are used and each snapshot requires about 100 MB hard disk space.

5 Experimental setup

5.1 Test facility

A test bench has been installed at the University of Rostock to investigate flow structures over dimpled surfaces using modern measurement techniques. The starting point was to plan and build up a test cabin providing electricity and water supply. Nevertheless, starting from the bottom has one advantage. The experimental setup has been constructed in a flexible way, where components, especially the test section, could be replaced easily by other configurations (like variation of dimple structures). A schematic flow chart of the closed-circuit water test bench is presented in the following Fig. 5.1. The head tank with an overflow inside, a settling chamber, the contraction valve followed by the entry section, a test section and a back tank with a metering system are the main parts of the test facility. A water reservoir, main pump, pipelines and four controlling valves are placed between each device to prevent outflow of water. Water is pumped from the reservoir into the head

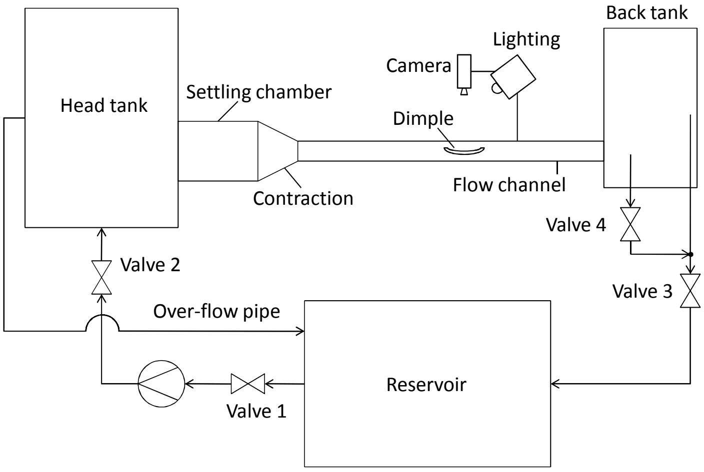

Fig. 5.1: Flow chart of the closed loop water channel.

tank by the main pump where a weir is installed to reduce turbulence and vibrations caused by the pump. In addition, a pipe is installed as a second overflow at a predefined height into the head tank for a special reason. One part of the water goes over the overflow back into the water reservoir whereas the other part flows over the weir into the settling chamber. The advantage of the construction is that a constant water level is permanently present to ensure constant massflow-rates inside the test section. The rectangular settling chamber has a dimension of 200x225mm connected to the rectangular test section with the dimension of 200x15mm. The geometrical dimensions are similar to that of Terekhov et al. [89]. The width $B = 200mm$ of the channel is chosen on the basis of numerical simulations to avoid influences of the sidewalls in the center of the test section. The construction of the valve was a challenging task. Insight the valve the turbulence level should be damped whereas at the outlet a block profile of the velocity is preferable for investigation of dimples with a defined boundary layer thickness. Therefore, a contraction contour using formula from Börger (1975) was used to design the inner contour of the valve. The profile was milled into laminated wood where afterwards a carbon fiber laminat of four layers was coated to ensure accuracy and stiffness of the valve. The test section consists of acrylic glass for visual access with an overall dimension of 1200x200x15 mm. The thickness of the acrylic glasses is about 15 mm to ensure the stability of the whole test bench.

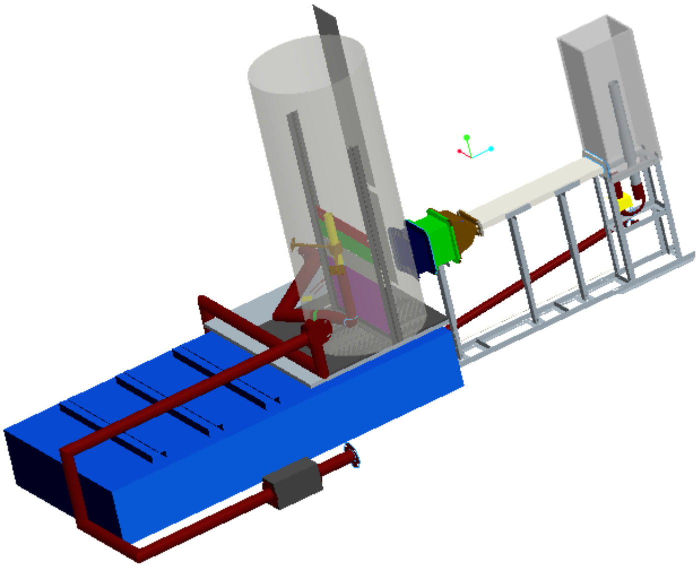

Fig. 5.2: Schematic sketch of the test bench.

The dimples, which are placed at the bottom of the test section, can be exchanged

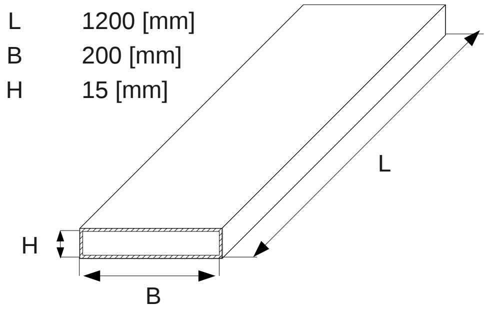

Fig. 5.3: Geometrical dimensions of the test section.

without having to dismantle the whole channel to ensure reproducibility and flexibility. The water of the test section enters the back tank where a second overflow is placed. The opening of the overflow was constructed to be large enough to ensure a constant water level at the back tank achieving a constant mass flow rate. The pressure resistance can be changed using valve no. 4 (see Fig. 5.1 in order to adjust the massflow rate which has to be achieved for the actual measurements. The range of the velocities inside the measurement section can be changed from 0 m/s to 1.5 m/s. Experimental results show a maximum turbulence level of about 5% at the inlet of the test section which is quite low and equal to that usual for wind tunnels.

5.2 Pressure and LDA measurements

Several pressure sensors have been placed at the lower surface of the channel to determine the pressure loss inside the test section. Bore holes with an inner diameter of $1.5mm$ are drilled into the test section and are connected via stable plastic tubes with an inner diameter of 4 mm to a measurement chart to determine the static pressure loss. The pressure bore holes are installed along the x-coordinate to calculate the pressure resistance coefficient C_p from a regression line (see Eq. 2.57). Piezo-resistive pressure sensors have been placed inside and outside of the dimples and are linked to a National Instruments A/D converter card to determine the pressure fluctuations. It allows the recording of pressure signals with a high frequency up to $200Hz$. Signal processing and system control was controlled by LABVIEW programs.

Laser Doppler Anemometry (LDA) technique as non-intrusive method is applied the measure the velocity profiles inside the test section. The 1D Neodym-YAG Laser with a wavelength of 532 nm, 12 mW power and a focal length of $400mm$ was mounted on a steering unit for exact positioning with a position accuracy of $0.1mm$.

The LDA system is a beam forward scattering system with a combined counter and tracker signal processor. It has to be noted that the focal point of the two laser beams is about five mm^3 which is found to be fairly high especially when the measuring point is located at the wall. The finite size of the control volume effects the measurements and is particularly important close to the wall since the velocity gradients reach its maximum in this part of the flow field. Moreover, the area's of interest have been painted with a diffusive black color to keep the effect of the reflections from the channel walls small. Nevertheless, exact measurements could not be obtained close to the walls to determine the wall shear stresses due to the large size of the control volume of the focal point and the impact of reflections. The signal at each measurement point was sampled over 10000 times ($Bursts$) in order to ensure a sufficient statistic. Further the Fast-Fourier-Transformation (FFT) is applied to extract dominant frequencies inside the dimples.

6 Heat transfer and flow structures of a single spherical dimple

The first part of the results is focused on the flow structures and heat transfer of a single spherical dimple placed in a narrow channel. To clarify the role of the vortex formations and its impact on heat transfer, experimental and numerical results are presented in the following sections.

6.1 Definition of the dimple standard case

The geometric dimensions of the dimples are chosen to match previously investigated dimples for verification and further investigations. A detailed experimental investigation has been performed by Terekhov et al. [89]. Therefore, the dimple standard case was chosen to match the geometrical configuration from Terekhov et al. [89]. The Fig. 6.1 represents the base geometry of the dimple referred to channel height H, dimple print diameter d and dimple depth h. The origin of the coordinate system is placed in the center at the bottom surface of the dimple . The x-coordinate is aligned in main flow direction whereas the y-coordinate is set normal to the surface and the z-coordinate in spanwise direction. Tab. 6.1 gives a summary of the geometrical dimple dimensions.

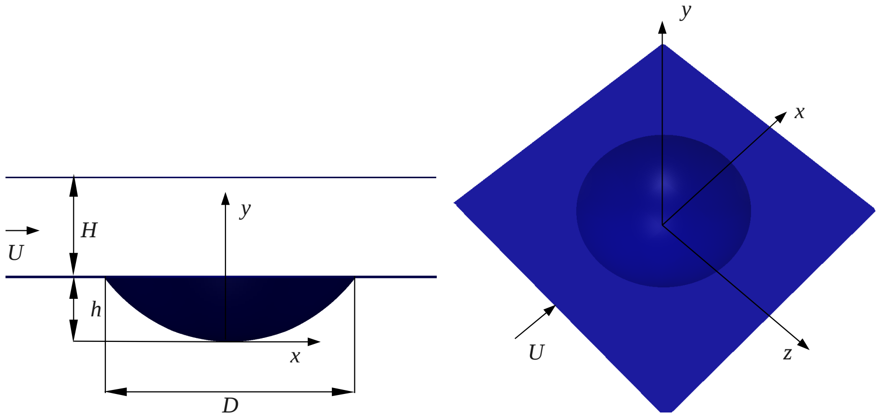

Fig. 6.1: Geometric dimensions of the single spherical dimple in a narrow channel.

Dimension	[mm]
H	15
h	12
d	46

Tab. 6.1: Geometrical dimensions of the dimple standard case.

The dimple depth to dimple print diameter ratio is defined as $h/d = 0.26$ and the dimple height to dimple diameter ratio as $H/d = 0.326$ which are commonly used dimple configurations cited in literature (e.g. Ligrani et al. [61]). The incident flow is adjusted to match a bulk velocity of $u_b = 0.88$ which corresponds to a velocity maximum of $u = 1.01 m/s$ assuming 1/7th power law for the velocity profile $(u(y)/u_{max} = (y/H)^{1/7})$ in the center of the channel. The Reynolds number Re_d calculated by the bulk velocity u_b, dimple print diameter d and kinematic viscosity ν is $\mathrm{Re}_d = 40000$ and the Reynolds number based on the channel height H is $\mathrm{Re}_H = 13043$ for the standard case. The Reynolds number Re_τ calculated from the friction velocity u_τ is determined as $\mathrm{Re}_\tau = 375$ using formula $\mathrm{Re}_\tau = 0.09\ Re_H^{0.88}$ (see Pope [80]) for a plane channel. It is very preferable since the turbulent channel flow at $\mathrm{Re}_\tau = 395$ is a well studied case in literature (see Kawamura et al. [47], Moser et al. [78]) and is often used as reference case for validation of numerical models. Tab. 6.2 summarizes the flow properties of the dimple standard case.

Tab. 6.2: Overview of the different Reynolds numbers for the dimple standard case.

Re_d	Re_H	Re_τ	u_b
40000	13043	375	0.88 m/s

6.2 Reference case: turbulent flow in a smooth channel

The simulations of the fully developed turbulent flow in a smooth channel at $\mathrm{Re}_H = 13043$ ($\mathrm{Re}_\tau = 375$) are carried out in accordance with the flow parameters which can be achieved in the present experiments to determine the reliability of the numerical methods. The mean values and higher order statistics are discussed and compared with empiric correlations and computations by Moser et al. [78] for $\mathrm{Re}_\tau = 395$. Since the Reynolds number Re_τ differs slightly, the reference data from Moser et al.

[78] is not exactly comparable to the present case but can be used for qualitative evaluation of the results.

Geometry

The domain of the chosen test case consists of two parallel walls with infinite dimensions. A sub-domain is extracted for the numerical simulations where periodic boundary conditions are applied in streamwise and spanwise direction. In contrast to Moser et al. [78], where the dimensions are set in reference to the non-dimensional channel height to $H = 2$, $L_x = 2\pi$ and $L_z = \pi$, the computational domain is down scaled and expanded in the present case since in the next step a dimple has to be placed at the lower wall. The channel height H is equal to that given test facility of $H = 0.015m$. The length in axial direction is set to $L_x = 0.16m$ and in spanwise direction to $L_z = 0.08m$. Thus, the ratio of channel length to channel height is about $L_x/H = 10.66$ which is fairly larger than $L_x/H = \pi$ as in the DNS computations performed by Moser et al. [78]. A disadvantage is that the expansion of the channel dimensions will require much more grid cells using LES method but ensures definitely the decrease of the autocorrelation functions to almost zero in streamwise and spanwise direction. A schematic sketch of the computational domain is presented in Fig. 6.2.

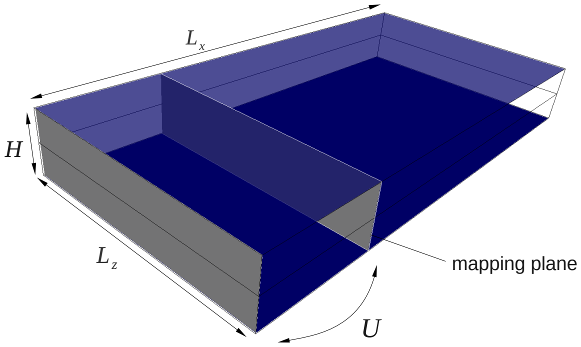

Fig. 6.2: Schematic sketch of the computational domain of the turbulent channel flow including the mapping plane for the precursor method.

Boundary conditions

The velocity can be treated periodically for the fully developed turbulent isothermal flow. However, periodic boundary conditions cannot be applied, when the incoming fluid is assumed to have a unity temperature and is heated up in the main flow direction (as it is the case of the numerical investigations of Isaev [42]). Hence, time resolved inflow conditions have to be set at the inlet boundary which is quite complicated in terms of LES for anisotropic flows. Moreover, to predict the exact growing of the thermal boundary layer thickness δ_T, it is obviously, that correlated inflow signals in space and in time are needed at the inlet. At time there are several methods to generate time resolved inflow conditions for LES whereas a detailed summary of the present inflow generation techniques was published by Tabor et al. [87]. The random generator is the simplest one and generates a turbulent uncorrelated noise of the velocity signal. Within this work it was shown, that the random generator reveals non-physical results since the turbulent signals are noncorrelated, have small scales proportional to cell sizes and are damped quickly behind the inlet due to the pressure correction method. Using a new inflow generation technique, called *method-of-turbulent-spots* proposed by Kornev et al. [54], physical results for the mean and rms values of the velocity could be obtained, but the growing of the temperature boundary layer thickness is found to be too sensitive in respect to the inlet conditions. To overcome the problem of setting time resolved inflow conditions, a method commonly known as precursor method was used. For this case a mapping plane is defined in line at a certain distance to the inlet inside the domain in order to copy the velocity field back to the inlet (see Fig. 6.2). It ensures a divergence free field and a fully developed state of the velocity profile. However, the bulk velocity u_b will decrease in time due to viscosity effects. To overcome this problem, an additional varying force, calculated from friction loss inside the precursor channel in every time step, is added in the momentum equation to keep flow rates at a constant level.

The non-dimensional temperature T^+ is set to $T^+ = 0$ at inlet whereas a constant temperature of $T^+ = 1$ is defined at the lower channel wall. The real temperature difference between the inlet and the lower wall is assumed to be small to keep the transport properties of the fluid constant. In most experiments a constant heat flux is realized as thermal boundary condition, but it has to be noted, that there will be only a maximum difference of 4% for the Nusselt number in turbulent flows whether a constant temperature or a constant heat flux is used as temperature boundary condition (see VDI Heat Atlas [92]). Tab. 6.3 summarizes the applied boundary conditions.

Grid resolution

Five different mesh resolutions of block-structured grids have been investigated to determine effects of resolution on mean values and high order statistics and to evaluate the necessary grid resolution. The mesh properties are given in terms of Δx_i^+

Tab. 6.3: Boundary conditions of fully developed turbulent flow in a plane channel for LES.

	upperwall	lowerwall	inlet	outlet
pressure	$\partial\overline{p}/\partial n = 0$	$\partial\overline{p}/\partial n = 0$	$\partial\overline{p}/\partial n = 0$	$\partial\overline{p}/\partial n = 0$
velocity	$\overline{u}_i = 0$	$\overline{u}_i = 0$	$precursor$	$\partial\overline{u}_i/\partial n = 0$
temperature	$\partial\overline{T^+}/\partial n = 0$	$\overline{T^+} = 1$	$\overline{T^+} = 0$	$\partial\overline{T^+}/\partial n = 0$

values based on the channel height H and the friction Reynolds number Re_τ in Tab. 6.4.

Tab. 6.4: Different mesh resolutions of fully developed turbulent flow in a plane channel for LES.

Mesh	Δx^+	Δy^+_{min}	Δz^+	N
C1	31.25	0.74	31.25	524288
C2	15.625	0.74	20.83	1572864
C3	15.625	0.372	20.83	3145728
C4	11.718	0.372	20.83	4718592
C5	7.812	0.372	15.625	8388608

A stretching normal to the wall is applied with a ratio of largest to smallest grid cell in wall normal direction of 7.5. The mesh resolution is homogeneous in streamwise and spanwise directions. For identification of the statistically steady state, the Reynolds stresses are averaged and evaluated on the fly during the simulation. Moreover, the statistical values related to velocity are averaged in homogeneous directions, in this case in streamwise and spanwise direction whereas only an averaging in spanwise direction could be applied for the temperature values. The simulations have been performed over a minimum time interval of at least $t^+ = 25$ (for the finest mesh C5). The non-dimensional time is defined in terms of the bulk velocity u_b and channel length L_x as

$$t^+ = \frac{t \cdot u_b}{L_x} \; . \tag{6.1}$$

Results

LES of turbulent flow between two parallel plates including heat transfer have been performed using three different SGS models, the dynamic Smagorinsky (DSM), the dynamic one equation eddy (oneEqEddy) and the dynamic mixed model (DMM). The obtained friction coefficient C_f has been compared to empiric correlation proposed by Dean

$$C_f = 0.0638 \times Re_H^{-0.25} \tag{6.2}$$

and has been calculated through the wall shear stress τ_w which is in turn related the pressure drop $\Delta p/\Delta x$

$$\frac{\Delta p}{\Delta x} = \frac{\tau_w}{H/2} \tag{6.3}$$

through the momentum balance (see Pope [80]) for the fully developed state. It is obviously that the pressure should decrease linearly in streamwise direction when the flow is fully developed.

The different SGS models have been applied for the meshes C1, C2 and C3, while for the meshes C4 and C5 only the DMM is used for closure of the momentum and energy transport equations due to the high computational resources. The obtained friction coefficients C_f for the investigated meshes are presented in Fig. 6.3.

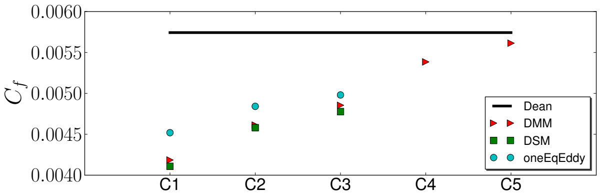

Fig. 6.3: Friction coefficient C_f for different mesh resolutions and different SGS models for a turbulent plane channel flow in comparison to empiric correlation proposed by Dean.

The friction coefficient C_f converges by increasing the mesh resolution for all SGS models towards the correlation of Dean whereas the oneEqEddy model show best performance compared to the DSM and DMM for the coarse meshes up to C3. Nevertheless, the obtained deviation of more than 20% to the empiric correlation on the coarse grids C1, C2 and C3 is too large and unacceptable for reliable investigations. The finest meshes C4 and C5 compare relatively well by a difference of 6.3% and 2.3% to the correlation of Dean due to the high wall resolution. Further it has to be noted, that the friction coefficient C_f determined from DNS data (Moser et al.[78]) is found 5.1% smaller than the calculated one from correlation of Dean. To conclude, the mesh resolutions of C4 and C5 seem to be sufficient to predict correct friction coefficients and thus correct pressure loss of the turbulent channel flow. The mean and rms values of the velocity for the resolved scales across the channel height are presented in Fig. 6.4.

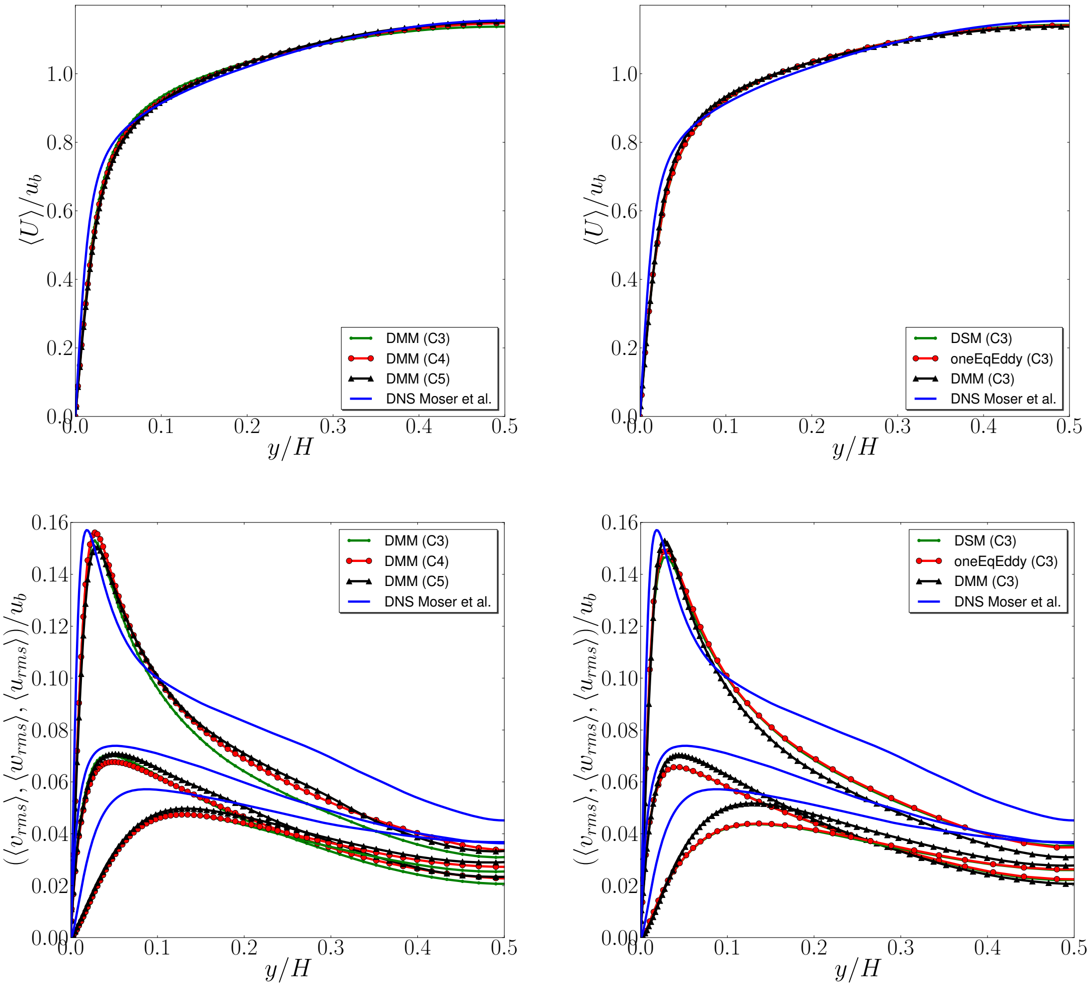

Fig. 6.4: Mean and rms values of the velocity normalized by the bulk velocity u_b from LES results using different SGS models and various grid resolutions for turbulent channel flow.

It is interesting to note, that the resolved mean and rms values show fairly good agreement to DNS data from Moser et al. [78], although the friction coefficient C_f reveals a strong grid dependence. Nearly no differences of the mean velocity could be observed for the DMM with varying grid resolutions. The results are normalized by the bulk velocity u_b since the usual normalization using friction velocity u_τ reveals a strong grid dependence and shows large deviations for the coarse grids. The reason for the small discrepancies to DNS data can be traced back to the small Reynolds number difference of $\mathrm{Re}_\tau = 375$ and $\mathrm{Re}_\tau = 395$. In addition, the second order statistics reveal no high differences in all simulations. The peaks of the turbulence intensity are close to DNS results due to the high wall resolution. Nevertheless, LES calculations underpredict the rms values in the buffer layer up to $y/H \geq 0.1$ due to the coarse resolution in the core region of the flow. But the results show, that the chosen wall resolution is capable of resolving near wall behavior of the turbulent flow with small discrepancies far away from the solid walls.

To evaluate the accuracy of the heat transfer rates, no adequate published data have been found to compare an evolving temperature boundary layer thickness for the present configuration. Therefore, empiric correlations for the flat plate are used to prove the Nusselt number Nu distribution in main flow direction at the heated wall. The question of comparability of turbulent channel flow and turbulent flow over a flat plate can be answered by the thermal boundary layer thickness δ_T. Since the channel height is fairly larger than the expected thermal boundary layer thickness, one can assume that the Nusselt number distribution is equivalent to that of the heated wall. The Nusselt number distribution Nu_x can be directly derived from laminar boundary layer theory for the laminar case using local Reynolds number in streamwise direction Re_x and the Prandtl number Pr (Baehr et al. [4]).

$$\mathrm{Nu}_x = 0.332 \cdot \mathrm{Re}_x^{1/2} \cdot \mathrm{Pr}^{1/3} \,, \tag{6.4}$$

The formula Eq. 6.4 is valid for $\mathrm{Re}_x < 6 \cdot 10^4$ and $0.6 < \mathrm{Pr} < 10$. Correlations for the turbulent case are found for a Reynolds number range of $5 \cdot 10^5 < \mathrm{Re}_x < 10^7$ and $0.6 < \mathrm{Pr} < 100$ by Chilton and Colburn (Baehr et al. [4])

$$\mathrm{Nu}_x = 0.0296 \cdot \mathrm{Re}_x^{4/5} \cdot \mathrm{Pr}^{1/3} \,. \tag{6.5}$$

The Nusselt number Nu is calculated within the LES using Eq. 2.9 and is presented in Fig. 6.5 in comparison to empiric correlations for the turbulent flow.

It is obviously that the DMM shows best performance to predict correct heat transfer rates in comparison to the other SGS models. It shows strong tendency towards correlation of Chilton and Colburn for the mesh C3, where the DSM and oneEqEddy model underpredict the expected Nusselt number distribution in flow direction. Moreover, convergence towards analytic correlation can be well reproduced when the mesh resolution is increased. The good performance of the DMM in respect to heat transfer can be explained by the dynamic adaption of the turbulent Prandtl number Pr_t which calculated dynamically in space and time within the

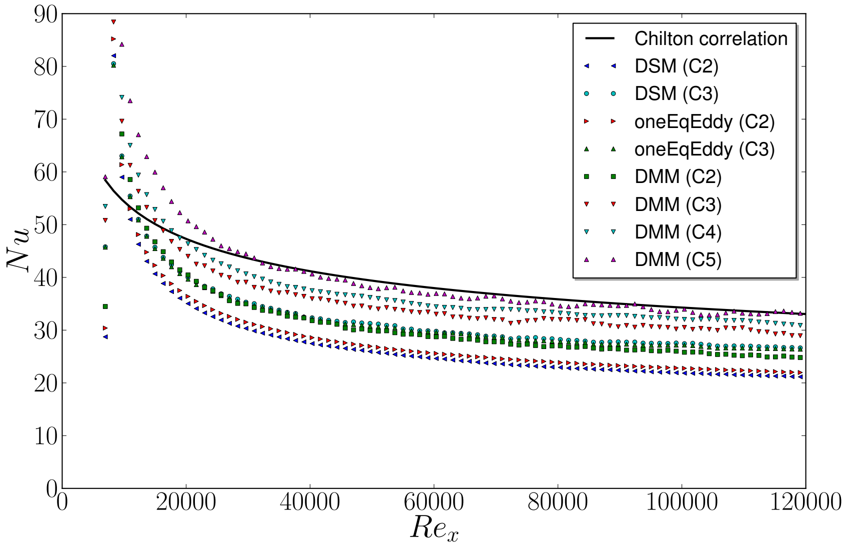

Fig. 6.5: LES results of Nusselt number Nu_x distribution at the heated wall in flow direction for turbulent channel flow using different SGS models and various grid resolutions in comparison to empiric correlations for the turbulent flow over a flat plate.

DMM (see sec. 3.3.3). This leads to a local determination of the turbulent Prandtl number Pr_t which is found very preferable in contrast to set the variable constant to $\mathrm{Pr}_t = 0.9$ as it is the case for the oneEqEddy model. But unfortunately it has to be mentioned that even the finest mesh resolution C5 is not sufficient enough to determine correct thermal boundary layer evolvement in main flow direction. The thin thermal boundary layer (which can be seen in Fig. 2.3) requires an even finer mesh resolution close to wall for the turbulent flow in a plane channel which leads to the conclusion, that in case when dimples are placed at the lower wall, the LES method can only be applied to determine qualitative heat transfer rates and not quantitative ones. Thus, the RANS method will be applied to determine overall heat transfer rates at the dimpled and flat channel wall. The validation of RANS method, especially for the heat transfer, is briefly summarized in appendix A.

6.3 Results

The numerical results of turbulent flow over a single dimple in a smooth channel including heat transfer using RANS and LES method are presented in this section. The focus is placed on the flow behavior and the formation of vortex structures inside and outside of the dimple and its impact on heat transfer. The POD analysis will give a deep insight into flow physics to clarify the role of asymmetric vortex structures with respect to heat transfer enhancement. Since the dynamic of the flow is in the foreground, the presentation of the results will be focused on LES results whereas RANS method is used to determine general influence of e.g. geometric parameters on integral values.

6.3.1 Validation of the numerical model

Domain size and grid resolution

As previously described, the geometry of the dimple was chosen to match experimental investigations performed by Terekhov et al. [89] and URANS computations performed by Isaev [40], [42]. The geometrical dimensions of the spherical dimple and channel are described in sec. 6.1.
The dimension in spanwise direction of $L_z/d = 1.74$ is equal to the turbulent channel flow where the length in axial direction is enlarged in front of the channel due to the inlet condition (precursor method) to $L_x/d = 4.34$. A schematic sketch of the computational domain is presented in Fig. 6.6.

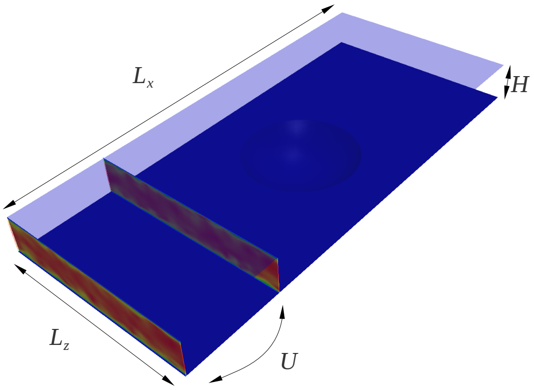

Fig. 6.6: Computational domain for LES calculations of turbulent flow over a single dimple.

A block-structured grid was chosen to keep the mesh size small where the dimple is discretized using an O-grid of eight blocks. A parametric mesh program was developed which allows the generation of meshes within the framework OpenFOAM in a very short time for a wide range of dimple geometries (Turnow et al. [91]). For further improvement of the mesh quality, the mesh motion technique in OpenFOAM was adopted to stretch predefined meshes onto a STL-surface solving a simple diffusion equation for the mesh movement. Hence, high quality meshes could be constructed with a special treatment of the dimple edges to capture flow separation including vortex shedding. The final mesh using mesh motion technique is presented in Fig. 6.7. It is obviously, that the changeover from the dimple edge towards the core flow is fairly smooth where grid lines follow the streamlines to keep nonlinear corrector loops for pressure correction low.

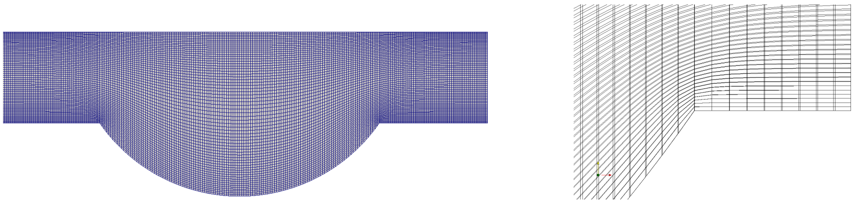

Fig. 6.7: High quality mesh of a single spherical dimple.

As it was shown in the previously presented results of the turbulent channel flow, a grid size of at least 4.7 mio cells is required for realistic determination of pressure loss inside the channel. It is a difficult situation, due to the fact, that the expected vortex dynamics has time scales up to $10s$ of realtime. The large time ranges could not be simulated using LES with timesteps smaller than $\Delta t = 1 \cdot 10^{-5} s$ due to the restricted computational resources. In this case, the simulations for a large time interval are carried out on coarse meshes which are found to be adequate to determine large scale motions inside the domain. The fine grids are used to determine local heat transfer rates and local physical phenomena inside the dimple. During this work a large number of meshes have been investigated. Finally three meshes have been determined to be adequate summarized in Tab. 6.5.

Tab. 6.5: Different mesh resolutions of a single spherical dimple for LES.

Mesh	N
A1	724288
A2	1572864
A3	4735648

Boundary conditions

The boundary conditions are similar to the turbulent channel flow described in sec. 6.2 and listed in Tab. 6.3. Periodic conditions are applied in spanwise direction neglecting the influence of the sidewalls. The position of the mapping plane for the precursor method was found to be sensitive since the spherical dimple influences the pressure field upstream. When the mapping plane is set too close in front of the dimple, the pressure disturbances will be copied to the inlet and thus will effect the whole flow dynamics. To ensure a homogeneous turbulent channel flow in front of the dimple, the mapping plane was put at $x/d = 1.02$ upstream from the front edge of the dimple (Fig. 6.6).

Results

Comparisons of the numerical results obtained from LES and RANS with experimental data and empiric correlations from literature are presented for further verification.

To get an overview of the grid dependency, the mean velocity profiles and its corresponding rms values across the channel height H at the center of the dimple at $\mathrm{Re}_d = 40000$ for the different meshes are presented in Fig. 6.8.

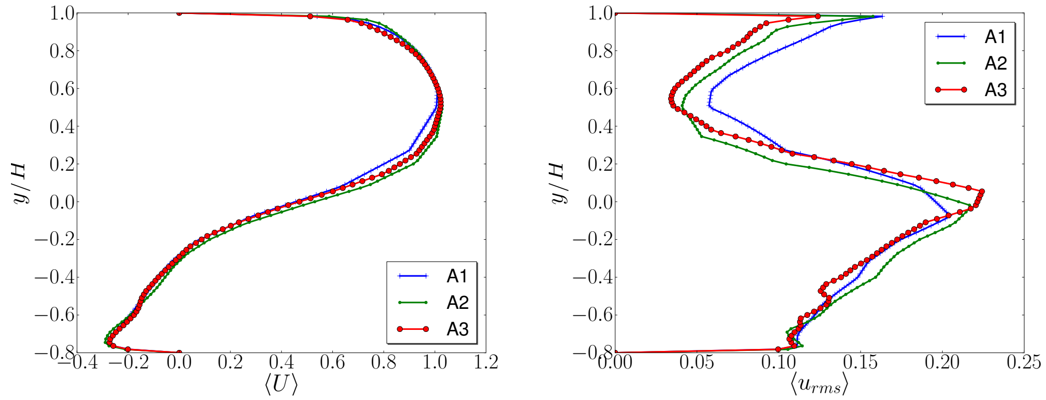

Fig. 6.8: Mean velocity profiles and its rms values across the channel height at the center of the dimple at $\mathrm{Re}_d = 40000$.

The dividing surface between the dimple and the channel is located at $y/H = 0.0$. The results obtained from three different meshes using LES show no large differences for the mean and rms values. In addition, the enlargement of the recirculation zone is found nearly equal for all three cases. Hence, one can assume that all grid resolutions seem to be adequate to capture all relevant flow physics inside the dimple. The same conclusion can be derived from mean and rms profiles of other positions inside and outside the dimple. In case of RANS, the grid dependency studies showed a sufficient mesh resolution of 1'272'864 cells using a $k-\omega$-SST-Model formulated for low Reynolds numbers presented in appendix A.

In Fig. 6.9 and Fig. 6.10 the profiles of the mean velocity and the turbulent kinetic energy at different streamwise positions $x/d = 0.0$ and $x/d = \pm 0.217$ within the midplane $z/d = 0.0$ of the dimple across the channel height obtained from

RANS and LES are compared to the LDA measurements by the Rostock group, to experimental data provided by Terekhov et al. [89] and to URANS calculations by Isaev [40].

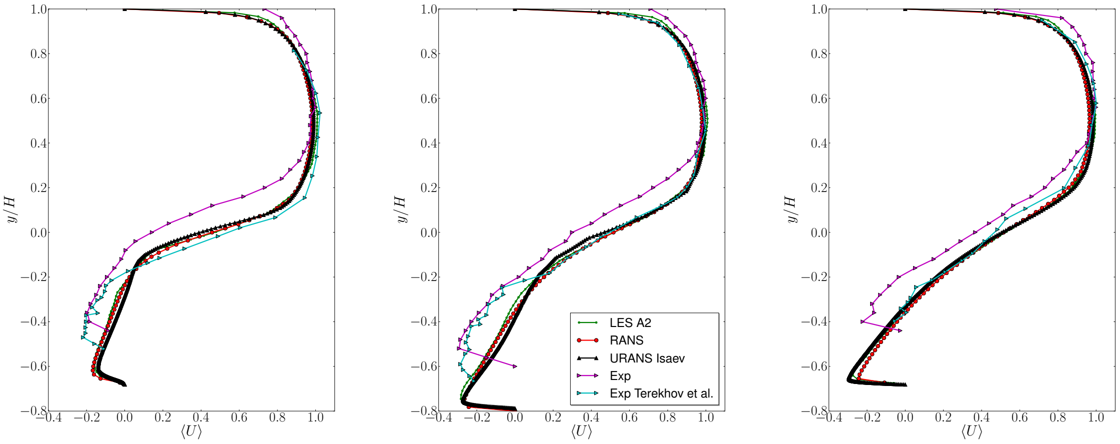

(a) $x/d = -0.217$ (b) $x/d = 0.0$ (c) $x/d = 0.217$

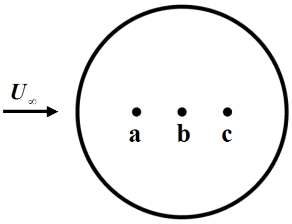

Fig. 6.9: Mean velocity profiles obtained from LES, RANS and LDA measurements for different positions in streamwise direction at the midplane $z/d = 0.0$ inside the dimple across the channel height in comparison to Terekhov et al. [89] and Isaev [40].

Numerical results obtained from LES and RANS show good agreement to the experimental data. Discrepancy with measurements can be observed in the near wall region inside the cavity. Whereas all simulations show nearly the same behavior for the mean velocity profiles, the experimental ones differ slightly to each other. The most probable reason for the discrepancy between theory and experiment are the typical LDA measurements problems in close proximity to the wall in narrow channels (explained in sec. 6.3.3). Personal communications to Terekhov confirmed the same discrepancies in the published data. Further the results reveal the presence of a recirculation zone inside the dimple with maximal negative velocities up to $u_x = -0.4\ m/s$. It is obviously that the extension of the recirculation zone shrinks normal to the wall in streamwise direction.

In contrast to the mean profiles, differences can be observed in the position of the magnitude of the turbulent kinetic energy k inside the dimple presented in Fig. 6.10.

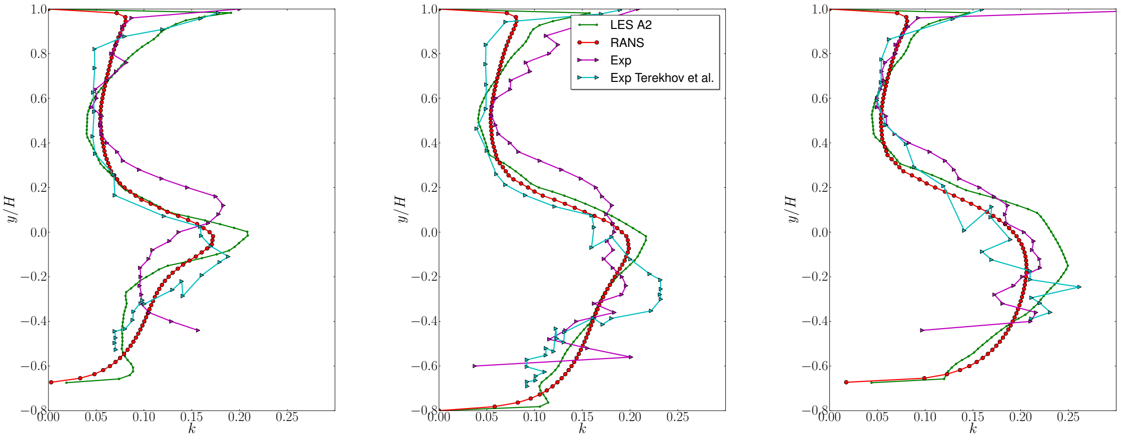

(a) $x/d = -0.217$ (b) $x/d = 0.0$ (c) $x/d = 0.217$

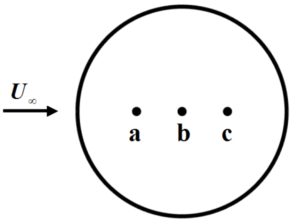

Fig. 6.10: Profiles of the turbulent kinetic energy k obtained from LES, RANS and LDA measurements for different positions in streamwise direction at $z/d = 0.0$ across the channel height in comparison to Terekhov et al. [89] and Isaev [40].

The presence of a shear layer between the recirculating flow and main channel flow leads to an increase of the fluctuations. The highest magnitude of pulsations can be found near the dividing surface between the channel and dimple where the magnitudes of the peaks are nearly equal. It is interesting to note, that the position of the peak is about $y/H = -0.2$ down from the dividing surface in measurements from Terekhov et al. [89] which is contradictory to the obtained numerical results. LES and RANS predict the largest fluctuations exactly on the dividing surface. Indeed, the maximum pulsations occur in the area of the strongest velocity gradients which is in accordance with well tried turbulence closure models. As it can be seen in Fig. 6.9, the strongest velocity gradients of the mean velocity are detected at the dividing surface $y/H = 0.0$ in numerical calculations and as well as in the performed experiments.

The results presented in Fig. 6.9 and Fig. 6.10 show, that LES and RANS methods are capable of predicting the correct flow field in a dimpled channel with a satisfactory accuracy and can be applied for further heat transfer investigations.

Pressure loss and heat transfer

The pressure and friction coefficients C_p, C_f and the Nusselt number Nu in flow direction at the mid-plane $z/H = 0$ are compared to measurements and empiric correlations.

The pressure coefficients C_p obtained from numerical simulations and experiments, from the measurements from Terekhov et al. [89] and from correlation proposed by Dean are presented in Fig. 6.11. The origin of the coordinate system is placed at center of the dimple.

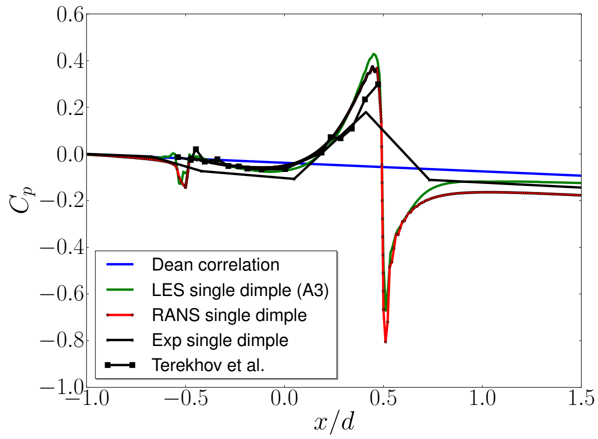

Fig. 6.11: Pressure coefficient C_p along the centerline in streamwise direction at the lower channel for a spherical dimple obtained from LES (A3), RANS and Experiment in comparison to correlation from Dean and experimental data by Terekhov et al. [89].

The pressure loss obtained from simulations and experiments upstream the dimple is equal to the pressure loss of a smooth channel as proposed by the empiric correlation of Dean. A small pressure decrease is observed at the leading edge at $x/d = -0.5$ since the flow becomes separated. The pressure coefficient C_p experiences an exponential increase further downstream equal to measurements of Terekhov et al. [89]. This effect is caused by the stagnation of the main channel flow which collides with the dimple surface. A dramatic pressure loss happens further downstream at $x/d = 0.5$ due to the flow separation where the flow passes over the trailing edge of the dimple. Afterwards the pressure gradient tends to be same as predicted by the correlation of Dean for a smooth channel. Moreover, the peak of the pressure obtained from numerical simulations matches nearly that of measurements from Terekhov et al. [89]. In contrast, the peak could not be found in the present pressure measurements since the distance between the sensors were too large. It is obviously that the overall pressure coefficient C_p obtained from RANS reveals higher than for LES and measurements. The reason of the discrepancy is found within the prediction of the flow structures in RANS which will be extensively discussed in the next section.

Snapshots of the pressure field in case of LES and time averaged pressure field from RANS at the lower channel wall are presented in Fig. 6.12. The zones of high pressure are located at the downstream side. Whereas only a small asymmetry is obvious in LES, a clear asymmetric formation of the pressure is depicted in terms of RANS. The reason for this phenomena can be found in the formation of the vortex structures which will be clarified in the next sections.

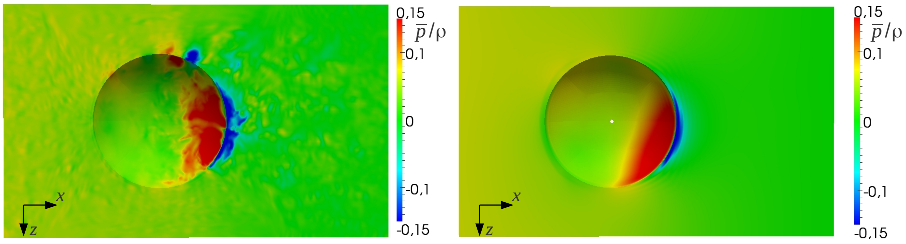

Fig. 6.12: Pressure distribution at the dimpled channel wall flow from LES (left) and RANS (right) at $\mathrm{Re}_d = 40000$.

In the Fig. 6.13 the Nusselt number Nu and friction coefficient C_f obtained from LES using different mesh resolutions and RANS in comparison to empiric correlations along the centerline in main flow direction at the dimpled wall are presented.

The influence of the mesh resolution can be seen in the distribution of the friction coefficient C_f and the Nusselt number Nu distribution in case of LES. The friction coefficient for the mesh A3 upstream the dimple in the range of $x/d = -1.0$ to $x/d = -0.5$ is slightly lower than that obtained from Dean correlation for the smooth surface. The discrepancies are enlarged for the coarse meshes A1 and A2 in case of LES. In contrast to LES, the RANS calculations overpredict the empiric correlation. When the fluid enters the recirculating zone of the dimple, the friction coefficients are lower compared to a smooth wall since the velocities are reduced inside the recirculation zone. A strong peak can be detected at the trailing edge due to the fact, that the fluid is accelerated near the wall when it is ejected out of the dimple.

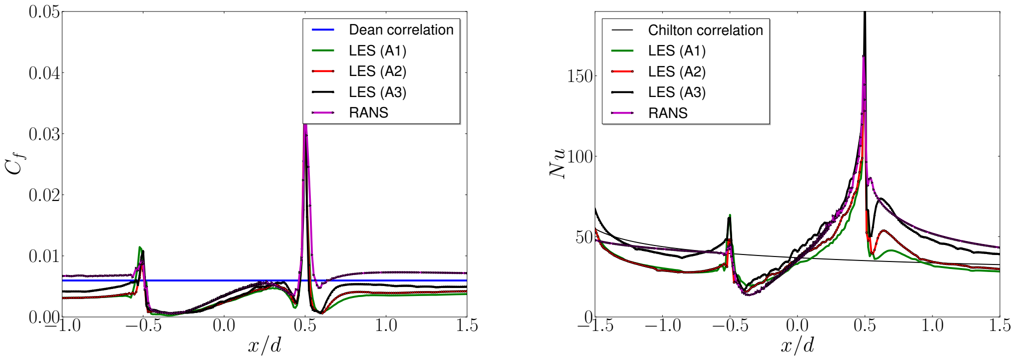

Fig. 6.13: Nusselt number Nu distribution along the centerline in flow direction at the lower channel with an inserted spherical dimple obtained from LES using different mesh resolutions and RANS in comparison to Chilton correlation for a flat plate (eq. 6.5).

The meshes A1 and A2 underpredict the heat transfer rates in case of LES whereas the mesh A3 shows only small differences with empiric correlation proposed by Chilton and Colburn for the flat plate upstream the dimple. A small increase of the heat transfer can be detected at the leading edge of the cavity due to the pulsations induced by the flow separation. Afterwards a strong decrease of heat transfer is present since the fluid is heated up in the recirculating zone and thus temperature differences decrease resulting in a lower heat flux. Since the recirculation zone takes over 80% of the whole dimple, a strong increase of heat transfer rates can only be found around the downstream edge. The cold channel flow attaches the back side of dimple with a high velocity causing vortex shedding at dimple trailing edge which causes a local increase of the heat transfer up to $\mathrm{Nu}/\mathrm{Nu}_0 = 2.81$. It is interesting to note, that in case of LES a small recirculation zone occurs at the trailing edge which causes a small decrease in the heat transfer rates. Since the dimple acts as vortex generator, the main increase of heat transfer can be found shortly downstream the dimple. Results from LES and RANS show that the increase of heat transfer is fairly high and can be up to $\mathrm{Nu}/\mathrm{Nu}_0 = 1.5$ even downstream the dimple at $x/d = 1.5$. In Fig. 6.14 a snapshot of the local Nusselt number Nu distribution using LES (left) and the time averaged Nusselt number Nu obtained using RANS (right) are presented. Whereas in RANS an asymmetric distribution of the Nusselt number Nu can be observed, LES results show only a small asymmetric distribution of the heat transfer. The same effects have been found in the pressure distribution as previously described and relies on the vortex formations inside the dimple.

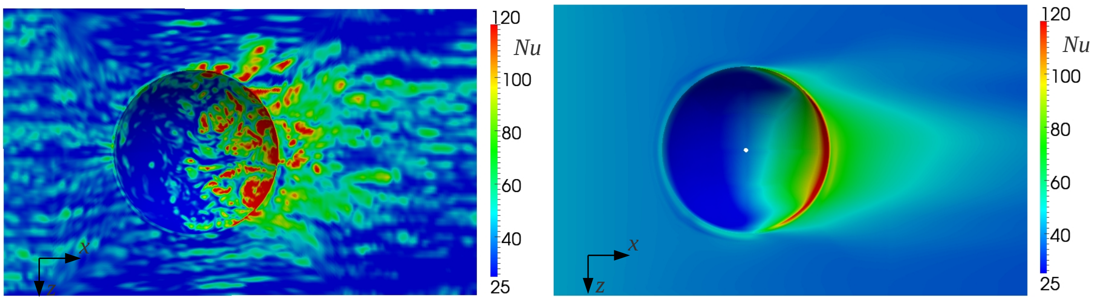

Fig. 6.14: Snapshots of Nusselt number Nu distribution at the dimpled channel wall flow from LES (left) and RANS (right) for turbulent flow at $\mathrm{Re}_d = 40000$ over a single spherical dimple.

6.3.2 Vortex structures

Basically the physics of the flow inside the dimple is complicated and is still not completely understood. Main attention of papers published in the literature has been paid to the heat and mass transfer effects averaged in time whereas the unsteady processes and their role in the heat transfer enhancement have not been thoroughly investigated. Since the form of the vortex has a strong impact on the heat transfer, as already shown in the Nusselt number distribution, the deep understanding of the flow physics inside of the dimple is important for the further improvements of the heat exchanger efficiency. The LES method gives the opportunity to investigate time resolved evolution of vortex formations. A detailed insight will be given for spatially resolved pressure distributions and instantaneous flow structures inside and around the dimple.

The profiles of the mean velocities presented in Fig. 6.9 show clearly the creation of a large recirculation zone where the time averaged zone occupies about 80% of the cavity. It can be seen from the presented velocity profiles, that the flow is fully symmetric in spanwise direction. However, concerning the vortex structures form appearing within the dimple there is a clear discrepancy between RANS and LES results. Depending on the depth to diameter ratio h/d the flow experiences a bifurcation in RANS. Whereas at a small ratio $h/d < 0.2$ the flow is found to be fully symmetric, at a ratio of $h/d = 0.2$ the flow experiences a topological change and becomes asymmetric with the creation of a vortex mono structure inclined to the mean flow direction at an angle of approximately $\alpha = \pm 45^\circ$. The choice between $\alpha = +45^\circ$ and $\alpha = -45^\circ$ is arbitrary and depends on the numerical simulation. Streamlines for two different dimple depth's $h/d = 0.13$ and $h/d = 0.26$ using RANS method are presented in Fig. 6.15 respectively.

But in contrast to RANS, the clear asymmetric structure is not predicted in the

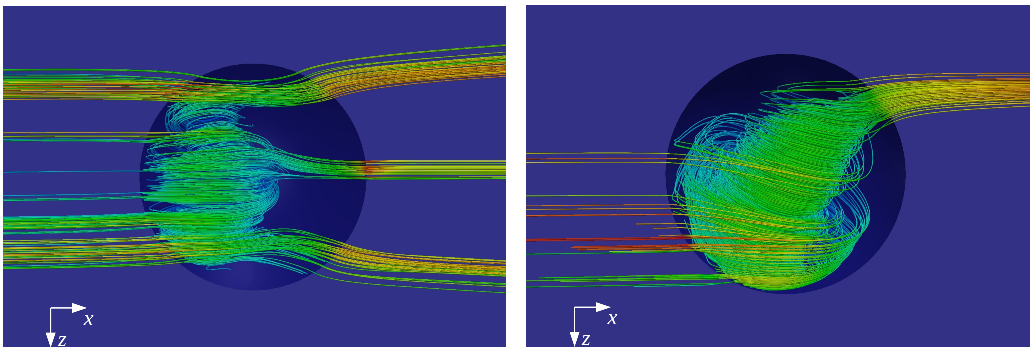

(a) $h/d = 0.13$ (b) $h/d = 0.26$

Fig. 6.15: Streamline patterns for turbulent flow over a single dimple for different dimple depths using RANS method at a Reynolds number $\mathrm{Re}_d = 40000$.

snapshots and time averaged velocity and pressure fields using LES method. The flow shows chaotic behavior and is dominated by small scale eddies. Instantaneous streamlines and λ_2-structures underline the highly turbulent state. Since instantaneous snapshots of the flow field look very chaotically, the analysis is performed using time averaging over varying time intervals to estimate a certain regularity of the flow. The Fig. 6.16 shows streamlines inside a cavity at a ratio of $h/d = 0.26$ at a Reynolds number of $\mathrm{Re}_d = 40000$ averaged within three seconds of real time at different time instants.

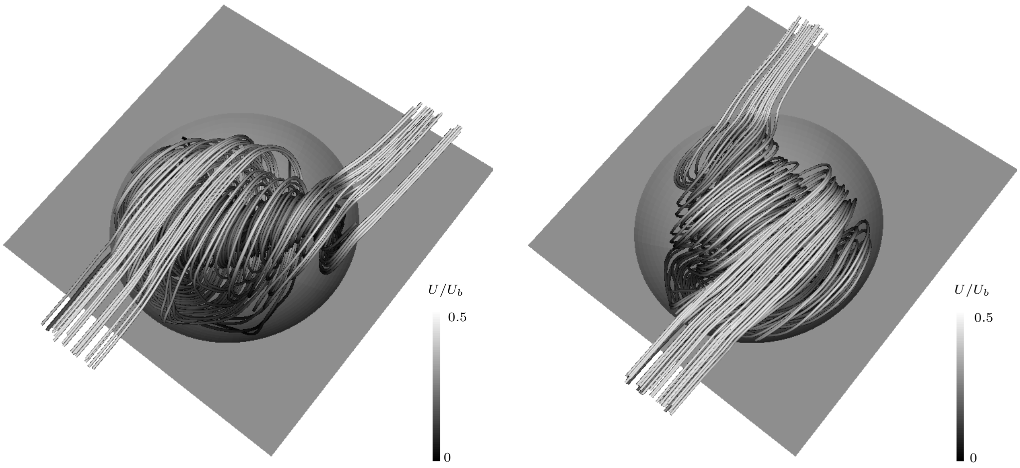

(a) (b)

Fig. 6.16: Streamlines obtained from LES velocity field averaged over three seconds of realtime for different flow periods inside a dimple at $h/d = 0.26$ for a Reynolds number of $\mathrm{Re}_d = 40000$.

It is obviously that LES also reveal the formation of asymmetric structures in phase averaged streamline patterns, but in contrast to RANS they are sufficiently unsteady. Streamlines indicate the asymmetrical vortex structures inclined to the mean flow switching its position from $\alpha = +45°$ to $\alpha = -45°$. As seen from instantaneous streamlines patterns, the fluid enters directly from the channel into the dimple and rotates within the recirculation zone and finally leaves the dimple at one side. Hence, for a dimple with a depth to diameter ratio of $h/d = 0.26$, numerical results from LES confirm the generation of unsteady asymmetric monocore vortex structures with a predominant transversal direction. However, the time averaged flow field over a sufficiently long time period is nearly symmetric which is in accordance with the performed measurements. In this context the results obtained from LES and measurement observations contradict to RANS ones which predict the asymmetry even in the time averaged flow pictures. Thus, LES reveals the generation of unsteady asymmetric monocore vortex structures with a predominant transversal direction which are responsible for the appearance of organized self-sustained oscillations. The vortex switching is also reflected in the time history of the longitudinal velocity U_x recorded from LES simulations at two symmetric points in spanwise direction $x/H = 0, y/H = 0, z/H = \pm 0.217$ at the dividing surface between the channel and dimple presented in Fig. 6.17.

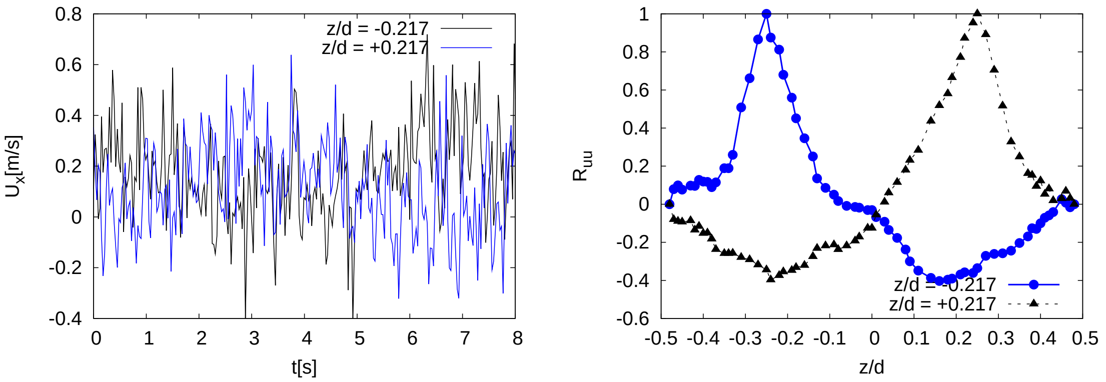

Fig. 6.17: Time history of longitudinal velocity U_x recorded at two symmetric points $x/d = 0, y/d = 0, z/d = \pm 0.217$ at $\mathrm{Re}_d = 40000$ (left) and correlation function R_{uu} at both points in spanwise direction (right).

Two following conclusions can be drawn from the velocity history and autocorrelation functions R_{uu}. First, the presence of long period self-sustained oscillations is obvious from the velocity history. Second, there is a sort of opposition-of-phase of the flow inside the dimple. The autocorrelation functions R_{uu} reveal a strong decrease in spanwise direction for both points where the correlated values become negative. The physical interpretation can be derived as follows and is sketched in Fig. 6.18. Once the flow is accelerated at the point $z/d = -0.217$, it is decelerated or even changes the direction against the main flow at the point $z/d = 0.217$. This effect can be explained by consideration of the mutual position of the vortex structure. The vortex is inclined both in horizontal and vertical directions. The inlet of the vortex is located deeply inside of the dimple whereas the outlet is above the dimple edge at the downstream side (shown in Fig. 6.16). Such a vortex induces both, positive and negative longitudinal velocities depending on the point of its location. The point $z/d = +0.217$ at the position $\alpha = +45^o$ (Fig. 6.16 left) lies above the vortex axis (green line in Fig. 6.18) which induces a positive velocity. The other point at $z/d = -0.217$ can be located either under the vortex or close to the vortex axis. In the first case there is a negative induced velocity, in the second case the induced velocity is lowered but still positive. The whole situation is changed when the vortex position is switched in spanwise direction. But for both cases the product of pulsations is negative. As a result the autocorrelation functions show negative values in spanwise direction with symmetry towards the midplane of the dimple. Thus, the asymmetric structure has not only an angle of $\alpha = \pm 45^o$ in axial direction, but also an angle of approximately $\alpha = 15^o$ in spanwise direction towards the lower channel wall. Moreover, the analysis shows that the vortex reveals a steady outflow of the dimple. The flow enters the dimple at one side, rotates inside the cavity while moving steadily towards the outflow and finally leaves the dimple with an orientation in streamwise direction. Interesting to see that the axis of the outcoming vortices are aligned with the main flow direction which is advantageously in respect to the induced pressure loss.

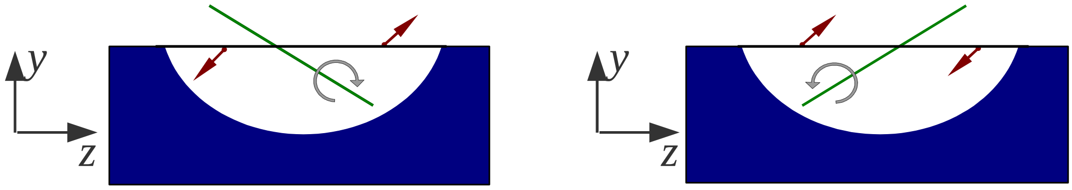

Fig. 6.18: Physical mechanism of the opposite-of-phase motion inside the dimple for the dominant modes.

Statistical data has been collected for determination of the shifting frequencies from LES calculations at two spatial points $x/H = 0.217, y/H = 0, z/H = \pm 0.326$. The data base consists of 60'000 equidistant time steps for a dimensionless time of $t^+ = 1760$ (see Eq. 6.1) which reflects a total real time of about $30s$. Fig. 6.19 presents the frequency spectrum for a Reynolds number $\mathrm{Re}_d = 40000$.

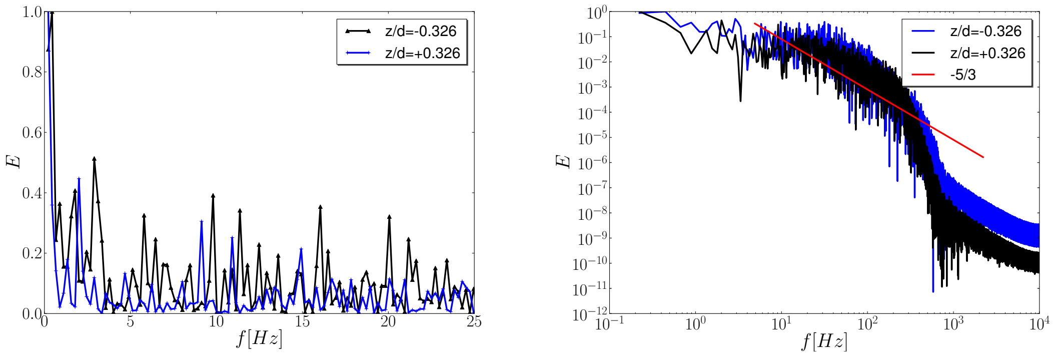

Fig. 6.19: Frequency (left) and energy (right) spectra of the longitudinal velocity U_x recorded at two symmetric points at $x/d = 0.217, y/d = 0, z/d = \pm 0.326$ at $\mathrm{Re}_d = 40000$.

Strong peaks can be observed at $f = 0.223Hz$ (corresponding Strouhal number $\mathrm{St} = f \cdot H/u_b = 0.0038$) in the frequency spectrum. These auto oscillation frequency is also found in experiments by Terekhov et al. [89] and is described as long period oscillations. Investigations documented periodical outbursts of vortices coming from the trailing edge using hydrogen bubbles for visualizations. LES clearly represents the low frequency component. The corresponding phase averaged streamlines are presented in Fig. 6.16 showing the asymmetry of the flow field and underline the oscillations of the monocore vortex structure in time towards the main flow. These valuable observations have now been quantified properly using LES method for the first time. In addition, the power spectra presented in Fig. 6.19 reproduces the inertial subrange with an $\omega^{-5/3}$ slope which underlines the accuracy of the present calculations.

From frequency analysis one may conclude, that the flow reveals the presence of a dominant mode with a low frequency at $f = 0.223Hz$. However, the switching process occurs *not* with a dominant frequency like for the Karman vortex street but reveals an intermittent character. Nevertheless, the simulations could not been carried out more than $30s$ of real time due to the limited computational resources. Thus, the shifting frequency will be further quantified using dye injection method discussed in the next section.

Another interesting flow feature is the appearance of the shear layer and its coherent vortex structures between the main channel and recirculating flow. Vortex rollups are generated within this shear layer enhancing fluctuations inside the dimple. The evolving structures are typical for flows with mutual velocities. Balares et al. [5] analyzed the coherent structures for free shear flows in detail where no solid walls bound the computational domain. The characteristic stages inside a shear layer can be determined either by Q-criterion or by iso-surfaces of the pressure as presented in Fig. 6.20.

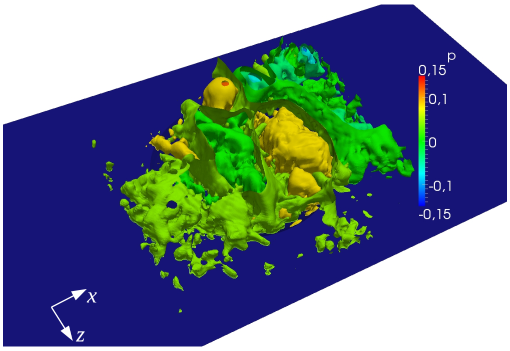

Fig. 6.20: Isosurfaces of the pressure field from LES at a time instant inside a single dimple at $\mathrm{Re}_d = 40000$.

The evolving vortex rollups are clearly represented in the pressure fields inside the spherical dimple. The structures are bound in spanwise direction due to the solid walls of the dimple whereas the growth of the shear layer thickness is limited by the downstream side of the dimple. When the flow attaches the dimple surface, the enrolling vortex structures break down and the fluid is forced either to move out of the dimple or to enter the recirculation zone. It is very interesting to note, that the characteristic vortex structures inside the shear layer cannot be observed in time averaged flow fields obtained from RANS. It has been found out using LES, that the behavior of the shear layer plays an important role for the orientation of the asymmetric vortex structure and its oscillation towards the main channel flow. The reason for this untypical phenomenon can be found in the inhomogeneity of the vortex structures generated inside the shear layer. The inhomogeneity of vortex rollups is a result of the vortex structures coming from the turbulent channel flow upstream the dimple. The evolution of coherent structures (commonly known as streaks) inside a plane turbulent channel flow in front of the dimple can be visualized using λ_2-criterion presented in Fig. 6.21 (b). As it can be seen, large scale structures evolve at the channel surface which strike into the shear layer breaking up the vortex rollups and leading to a strong inhomogeneity.

The asymmetric formation of the vortex inside the dimple can be explained as follows. First the attached fluid becomes an additional velocity component in spanwise direction towards the midplane of the channel for both sides due to the curvature of the dimple sphere sketched in Fig. 6.21 (a).

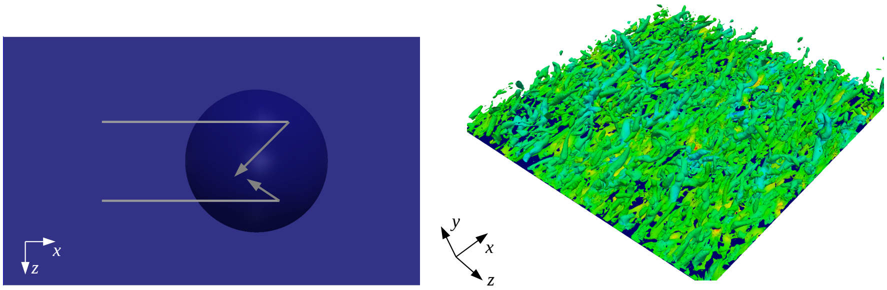

(a) (b)

Fig. 6.21: (a) Sketch of rebound velocities from the attached fluid at the dimple downstream side. (b) λ_2-structures inside a turbulent channel flow at Reynolds number $\mathrm{Re}_H = 13042$.

Second the formation of the asymmetric vortex structure is a result of the different magnitudes of the spanwise velocities acting on the recirculation flow inside the dimple. When the fluid enters the dimple, the existing vortex structures inside the shear layer decelerate the incoming flow differently due to their inhomogeneity (see Fig. 6.19) in spanwise direction which finally results in different attachment points of fluid at the downstream side of the cavity. Hence, different spanwise velocities are present due the different impact angles of the dimple curvature. When different velocities effect the reverse flow, the flow turns into a following asymmetric stable position.

The investigations of turbulent flow using LES over a single spherical dimple show the following main features:

- Formation of asymmetric structures inside the dimple with only one outflow
- Vortex shedding at the dimple trailing and leading edge
- Evolution of a bounded shear layer with inhomogeneities in spanwise direction
- Switching of the asymmetric vortex structure in time with respect to the main channel flow

6.3.3 Experimental confirmation of numerical results

Flow visualization

From several authors (e.g. Terekhov [89], Isaev [42]) it was found that asymmetric vortex structures occur inside a spherical dimple up to a certain Reynolds number.

To clarify the structures in a first view in the experiments, flow visualizations based on dye injection have been performed for a single dimple in dependence of the Reynolds number. Therefore, several bore holes were drilled into the acrylic glass inside and outside of the dimple with a diameter of $0.5mm$ to keep the influence of the bore holes small. All bore holes are connected via flexible tubes to a distribution device to have the opportunity of dye injection at one or more position at the same time. A small lift pump was installed to drive the dye through the pipes with a limited speed. The dissolution of high concentrated potassium permanganate ($KMn0_4$) was used to provide good visibility. A common Sony Camcorder with 12x optical zoom and a resolution of 1.07 megapixel has been placed 600 mm above the test section to record the dye filaments. Several lamps have been installed to avoid reflections from the dimpled surface. Flow visualizations have been performed for different Reynolds numbers up to $\mathrm{Re}_d = 60000$ to investigate the dynamics of the asymmetric flow structures in a spherical dimple. The different positions of the boreholes are sketched in Fig. 6.22.

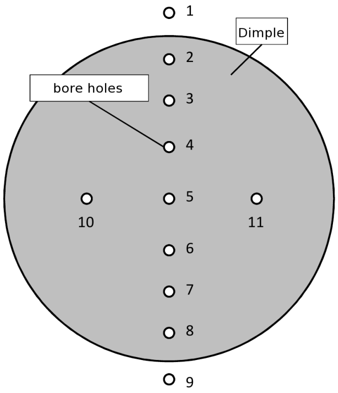

Fig. 6.22: Positions of the boreholes for dye visualization inside and outside the dimple.

For low Reynolds numbers flow ($\mathrm{Re}_d \leq 200$) over the single dimple the streamlines are symmetric and parallel containing only small fluctuations near the downstream edge of the dimple. As the velocity is increased for Reynolds numbers between ($200 \leq Re_d \leq 1000$), the flow over the dimple becomes separated at the leading edge of the dimple and a recirculation zone arises inside the cavity. The size of the separated region is growing up to the highest Reynolds number $\mathrm{Re}_d = 60000$. At first, two symmetrical vortices can be seen with its axis in transverse direction linking both vortices together. The flow structures are stable and symmetric towards the spanwise direction. With an increasing Reynolds number more than $\mathrm{Re}_d \geq 1000$, the flow inside the dimple losses its symmetrical character and becomes unsymmetrical, but remains in a stable position. The observation of asymmetry and stability is in accordance with RANS calculations. It has to be noted, that the incoming flow is fully symmetric, the channel and dimple geometry is fully symmetric, but in contrast the evolving vortex structure insight the dimple is *asymmetric*. Up to a Reynolds number $\mathrm{Re}_d = 10000$, which is still in the transitional range, the asymmetric vortex formations become unstable and change their directions towards the mean flow without any external impact. In case of $\mathrm{Re}_d = 20000$, the shifting of the vortex occurs non-periodic at large time periods in the range $20s$ to $30s$. For the defined standard case with a Reynolds number of $\mathrm{Re}_d = 40000$, the time periods of the shifting of the vortex axis towards the main flow becomes smaller within the range of $5s$ to $20s$ and is further referred as *low* frequency or as self-sustained oscillation. These low frequency components found from dye experiments confirm the results obtained with LES in the previous section. The two asymmetric vortex positions are presented in Fig. 6.23 in original color and in black/white color to highlight the structures using three different positions for dye injection.

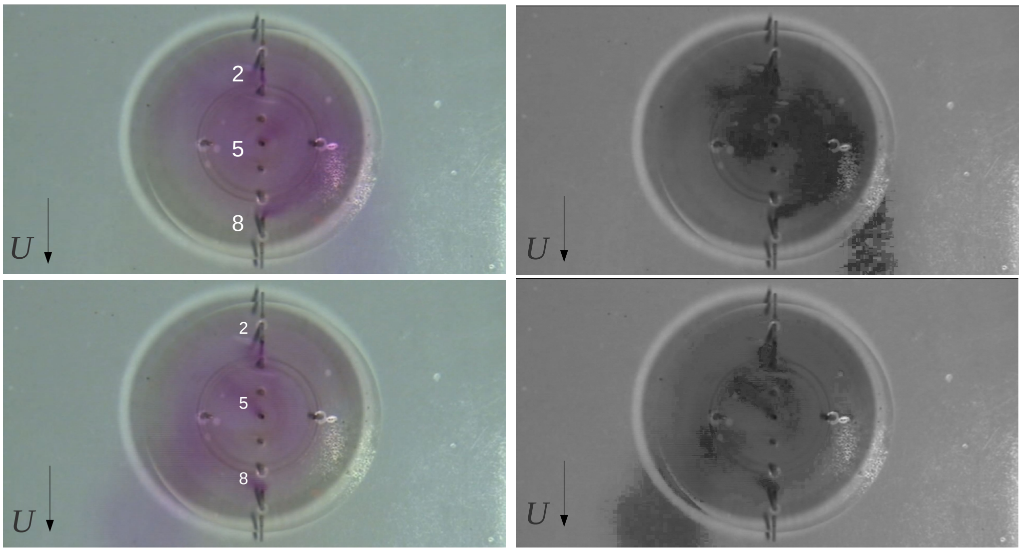

Fig. 6.23: Flow structure inside a single dimple for $\mathrm{Re}_d = 40000$ using dye injection method at different points.

It is obviously, that the position of the vortex changes in time. From position 5 and 8 the dye moves to the left or right side of dimple in direction of the main flow whereas the injected dye from position 2 goes into the opposite direction. Since the position 2 is located near the trailing edge of the dimple it can be concluded, that the recirculation zone nearly covers the whole dimple. Thus, the stagnation point of the attaching fluid is fairly close to the dimple downstream edge. Using slow motion feature from video records one can explicitly determine the path lines of the dye. It can be seen that the injected dye is steadily leaving the dimple depression since the colour of the fluid inside the dimple is not concentrated which is preferable in terms of heat transfer. From the dye injections it is interesting to note, that the flow can only exit at one corner of the dimple as it was shown by the numerical simulations in the previous section.

Fig. 6.24 presents snapshots from the asymmetric structure inside a single dimple using different dye injection positions including the axis of the asymmetric structure towards the main channel flow.

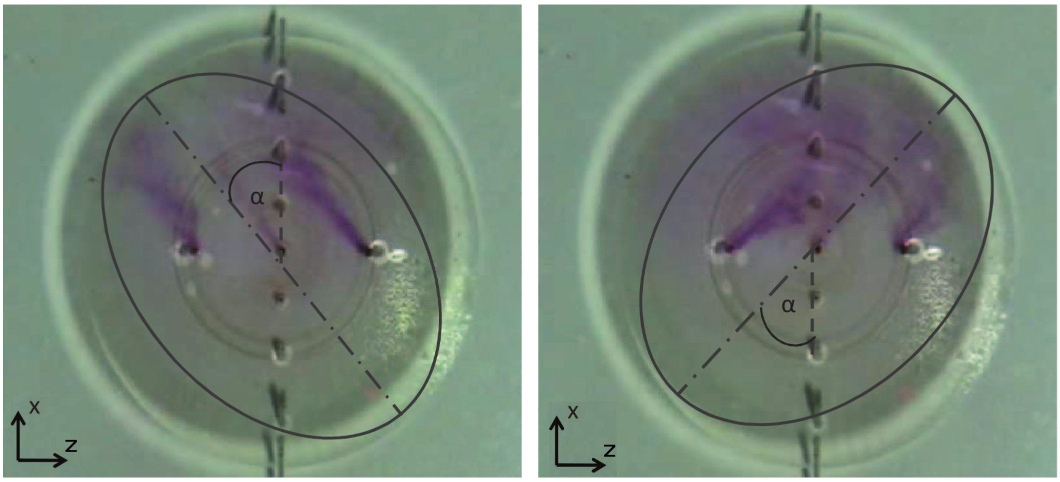

Fig. 6.24: Flow structure inside a single dimple for $\mathrm{Re}_d = 40000$ together with the inclination angle towards the main flow.

The angle α_v of the structure is about $\alpha = \pm 45^\circ$ towards the mean flow direction (x-axis) for each position. It should be noted again that the changing of the angle α_v of the structure changes in time in the range of $5s$ to $20s$ with no preferable direction which is in accordance with experimental observation by Terekhov et al. [89] and numeric simulations using LES. The flow visualizations give a clear impression of the flow behavior for laminar and turbulent flow over a single dimple and outlines the important features for correct interpretation of the LDA and pressure measurements and numerical simulations.

LDA Measurements

LDA measurements have been performed at the described test facility (see section 5.1) for the dimple standard case at a Reynolds number $\mathrm{Re}_d = 40000$ for isothermal conditions. The measurements provide an independent data base for validation of the numerical methods and confirmation of the numerical simulations.

To analyze the asymmetry of the vortex structure inside the dimple, measurements of the velocity profiles at the center of the dimple with an offset of $z/H = \pm 0.217$ in spanwise direction have been performed. The mean profiles and its rms values are presented in Fig. 6.25 (a) where the center of origin is placed in the dividing surface of the channel and dimple. It is interesting to note that no significant differences between both profiles could be observed. Hence, the mean averaged profile of the velocity is symmetric in spanwise direction. Although the dye visualization clearly indicates the presence of instantaneous asymmetric vortex structures, the averaged flow is, due to persisting switching of vortex structures, symmetric. The observations confirm the numerical results obtained from LES.

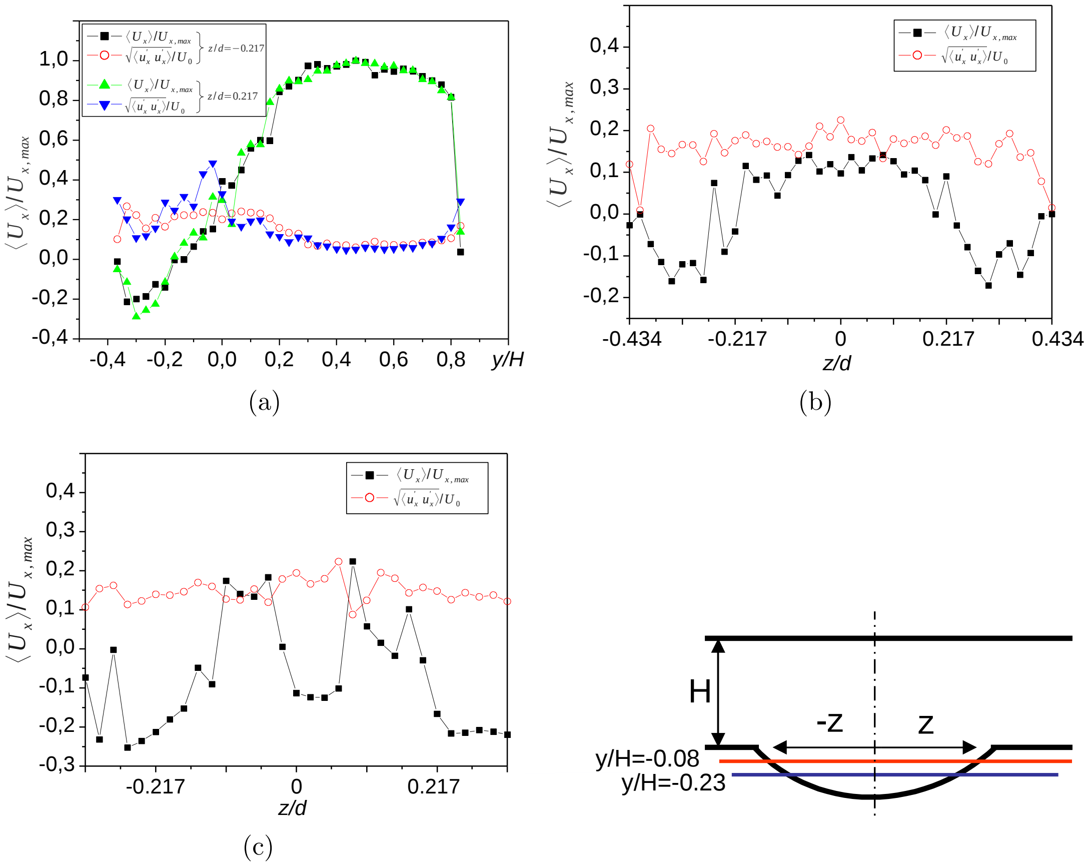

(a) (b) (c)

Fig. 6.25: Velocity and rms profiles at two different points at $z/d = \pm 0.217$ across the channel height from LDA measurements (a). Distribution of axial velocity U_x and rms values from LDA measurements in spanwise direction for two different channel heights at $y/H = -0.08$ (b) and $y/H = -0.23$ (c).

To recheck the symmetry of mean profiles inside the cavity, measurements of the axial velocity U_x in spanwise direction (z-axis) at two different channel height $y/H = -0.08$ and $y/H = -0.23$ inside the dimple at have been performed and are presented in Fig. 6.25 (*b*) and Fig. 6.25 (*c*) respectively. The profiles confirm, that time averaged profiles are symmetric towards the spanwise direction. Deep inside the dimple at $y/H = -0.23$ a significant decrease of the velocity at the center $z/H = 0.0$ can be detected whereas two peaks depart from the center at $z/d = \pm 0.1$ exist. Using experience from dye visualization one can see, that two peaks of the velocity profiles cannot be present at the same time instant. Hence, one can conclude, that the vortex structure insight the dimple has a certain angle towards the main flow which causes one of the two peaks depending on its angle $\alpha_v = +45°$ or $\alpha_v = -45°$. The mean profiles in comparison to experimental data from Terekhov et al. [89] are presented in appendix B. Since time resolved data is recorded via LDA measurements, investigations of the time signal using FFT analysis have been performed at two different points at the center for different heights. More than 30000 bursts have been detected within a total measurement time of at least $20s$ of real time. The time signals are recorded at non-equidistant time steps. To keep errors of the FFT at a low level, the time signals have been approximated using splines to obtain equidistant time steps. A detailed error analysis has been performed by Frenz [25]. The corresponding energy spectra are presented in Fig. 6.26.

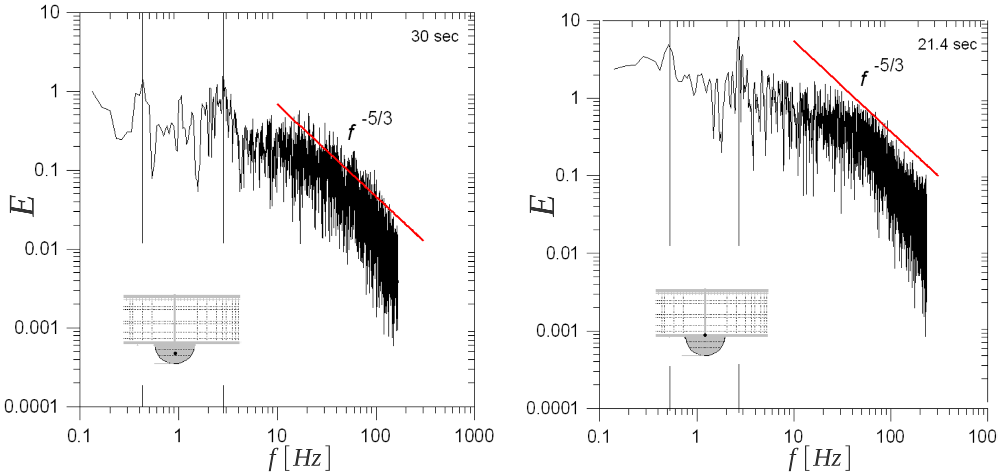

(a) $y/H = -0.4$ (b) $y/H = 0.1$

Fig. 6.26: Energy spectra of velocity signal recorded from LDA measurements at two different positions inside the dimple at $\mathrm{Re}_d = 40000$.

Two dominating frequencies $f = 0.4Hz$ and $f = 2.9Hz$ at both points for both spectra can be observed. The frequency $f = 0.4$ clearly represents the shifting of the asymmetric structure inside the dimple. It has to be noted, that from LES calculations a frequency $f = 0.223Hz$ is obtained for points located at $z/d = \pm 0.217$ shifted in spanwise direction. Hence, the vortex switching occurs at the points $z/d = 0.0$

with a double frequency of $f = 0.4Hz$. Moreover, the second frequency of about $f = 2.9Hz$ represents the shedding of the vortex structures inside the shear layer between the main channel and recirculating flow. The corresponding Strouhal number $\mathrm{St}_d = 0.152$, calculated by the dimple print diameter d, could not be clearly identified in the numerical simulations and is therefore questionable. Chang et al. [12] investigated the turbulent incompressible flow over a rectangular two-dimensional shallow cavity with a ratio of $L/d = 2$ inside a channel at a Reynolds number $\mathrm{Re}_H = 3360$. The Strouhal number is determined as $\mathrm{St}_d = 0.51$ which is in accordance with other data published in the literature. Therefore, in our opinion the predicted frequency of $f = 2.9Hz$ reveals not correct in the experiments. But in contrast the frequency spectra obtained from LES (see Fig. 6.19) shows magnitudes around $f = 10Hz$ which corresponds to a Strouhal number of $\mathrm{St}_d = 0.52$ and compares well to data from Chang et al. [12].

To summarize the results from LDA measurements, the dye visualizations of structures inside the dimple proved to very important for correct interpretation of the different velocity profiles. Imagine one would not know about the presence of asymmetric structures, one would conclude on the basis of mean profiles, that the flow is fully symmetric which leads to a wrong interpretation of flow characteristics. Therefore, the combination of dye investigations and LDA measurements is desirable and confirms the numerical results obtained using LES method.

Pressure distribution

The pressure distribution at the bottom surface for a single dimple at $\mathrm{Re}_d = 40000$ have been investigated experimentally in addition to dye visualizations and LDA measurements. This work was done mainly by Dr. Voskoboinick. Static pressure sensors have been installed at the midplane at the bottom surface of the channel in main flow direction. The pressure should be decreasing linearly in flow direction when the flow is fully developed for a turbulent channel flow as derived from the momentum balance. The gradient of the regression line of the pressure decrease for a smooth channel can be compared to empiric correlation proposed by Dean [1978] (see Eq. 6.2). In Fig. 6.27 the obtained pressure coefficients C_p for a smooth channel and for a single dimple are compared.

First it can be observed that the pressure gradient obtained from measurements for a smooth channel captures the correlation of Dean with a small deviation of 3.2% for a total length of $x/d = 12$. The measurements have been done carefully, but nevertheless the results are found to be very sensitive since the measured pressure

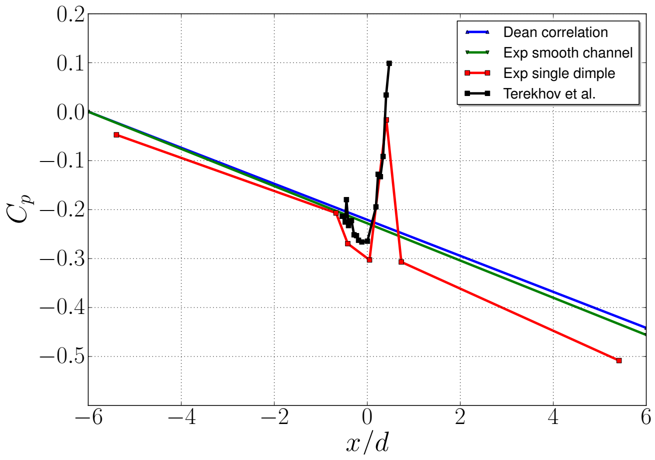

Fig. 6.27: Distribution of the pressure coefficient C_p at the lower wall along the centerline in flow direction obtained from experiments for a smooth channel and a spherical dimple in comparison to empiric correlation of Dean and measurements from Terekhov et al.[89]

differences are relatively small. Second, when a single dimple is placed onto the surface, the pressure drop increases of about 13.7% in a distance of $x/d = 5.0$ in comparison to a smooth channel. A visible decrease of pressure can be found inside the dimple which is nearly about 75% of the whole dimple length in axial direction from $x/d = -0.5$ to $x/d = 0.5$. A high peak can be observed further downstream at the downstream edge of the dimple. The peak reveals the point where the main flow attaches the dimple surface. Due to the flow separation at the downstream edge, a large decrease of pressure is present which is lower than the overall pressure drop for the smooth channel. The pressure gradient decreases further downstream of the dimple equally to that of the smooth channel wall.

To study the role of asymmetric vortex structures and its alternation, piezo-resistive pressure sensors have been installed inside and outside the dimple. In Fig. 6.28 (a) the different positions of the pressure sensors are presented. Fig. 6.28 (b) the demonstrates the rms values for a wide range of Reynolds numbers Re_d.

The positions 1 and 2 are located upstream the dimple representing measurements in a smooth channel which can be compared to data from literature presented in Fig. 6.28 (c). From the authors point of view, the measurements performed by Farabee [19] and DNS by Kim [50] are most trustful. Fig. 6.28 (c) presents the rms values of pressure fluctuations for the equivalent Reynolds numbers Re_τ based on the friction velocity. The measurements compare well with experimental data of Farabee [19]. In addition, the DNS results (Kim [50]) reveal a magnitude of the

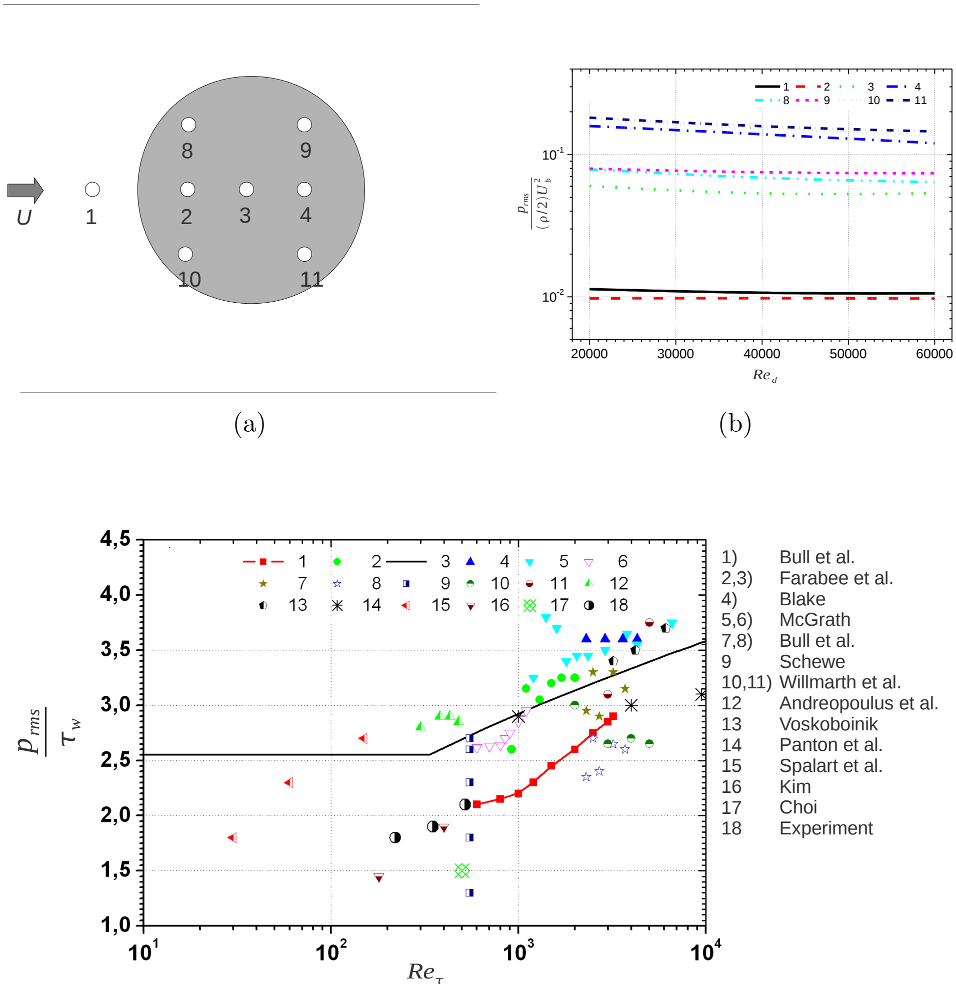

(a) (b)

(c)

Fig. 6.28: Different locations of dynamic pressure sensors (a). Distribution of rms values of the pressure signal inside and outside a single dimple for various Reynolds numbers starting from $\mathrm{Re}_d = 20000$ up to $\mathrm{Re}_d = 60000$ at different positions inside the dimple (b) and in comparison to published data for a smooth channel for position 1 and 2 (c).

pressure direct at the wall of about $p_{rms}/\tau_w = 1.5$ for a Reynolds number $\mathrm{Re}_\tau = 185$ (nearly equal to $\mathrm{Re}_d = 20000$) which matches fairly well with the performed experiments of $p_{rms}/\tau_w = 1.4$. It is interesting to note that the magnitude of the fraction $p_{rms}/(0.5\rho/u_b^2)$ value does not change significantly in each location for the investigated range of Reynolds numbers. Thus, the wall pressure fluctuations p_{rms} are found to be linear proportional to $(0.5\rho/u_b^2)$. Further it is obviously that the pressure fluctuations inside the dimple are significantly higher than those for the smooth channel. Especially at the downstream edge high magnitudes occur due to the impingement of the main flow, which are one order of magnitude higher than for the smooth channel. It is evident that at the bore hole in position 9 and 11 the highest fluctuations are present.

In addition, the time signals, cross-correlations and energy spectra from pressure signals have been analyzed to determine time flow physics and dependencies between the pressure signals at different positions. In Fig. 6.29 the pressure time signals at different positions inside the dimple for $\mathrm{Re}_d = 40000$ are presented.

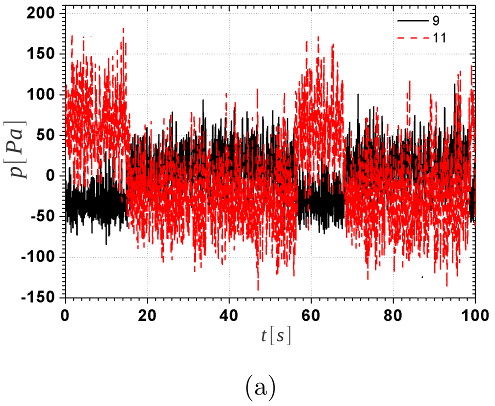

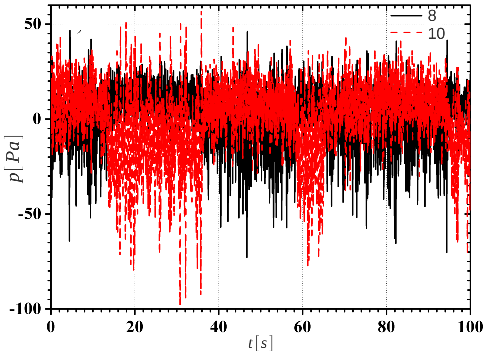

(a) (b)

Fig. 6.29: Time signals of the pressure at different positions at $x/d = 0.32$ (a) and $x/d = 0.32$ (b) at $z/d = \pm 0.32$ inside the dimple for a Reynolds number $\mathrm{Re}_d = 40000$.

The presence of an asymmetric vortex structure inside the dimple can be directly seen by the opposite signs of the pressure signal. The main flow attaches the dimple surface at one side whereas the flow is entering the recirculation zone at the opposite side and forces a decrease of the pressure. The time signals clearly show, that the shifting of the vortex is not periodical which is in accordance with visual observations using dye injection and numerical simulations using LES. The preferred direction of the vortex structure is about $\alpha_v = -45°$ for position 8 and 9 in the experiments probably due to some inhomogeneities of the main flow. However, this concludes that in an averaged sense one will determine a frequency of the vortex shifting, but in reality the alternation process is intermittent.

To investigate the correlation between the different positions, the cross-correlations are calculated. Fig. 6.30 (a) represents the cross correlation coefficient R_{ij} between position $9-11$, $4-9$ and $4-11$ in spanwise direction at $x/d = 0.32$ whereas Fig. 6.30 (b) shows the function between position $8-10$, $8-3$ and $10-3$ in spanwise direction at $x/d = 0.0$ and Fig. 6.30 (c) the positions $2-3$, $2-4$ and $3-4$ in axial direction at the centerline. A clear dependence between the pressure signals is obvious in spanwise direction due to the alternation of the vortex structure from $\alpha_v = \pm 45°$ towards

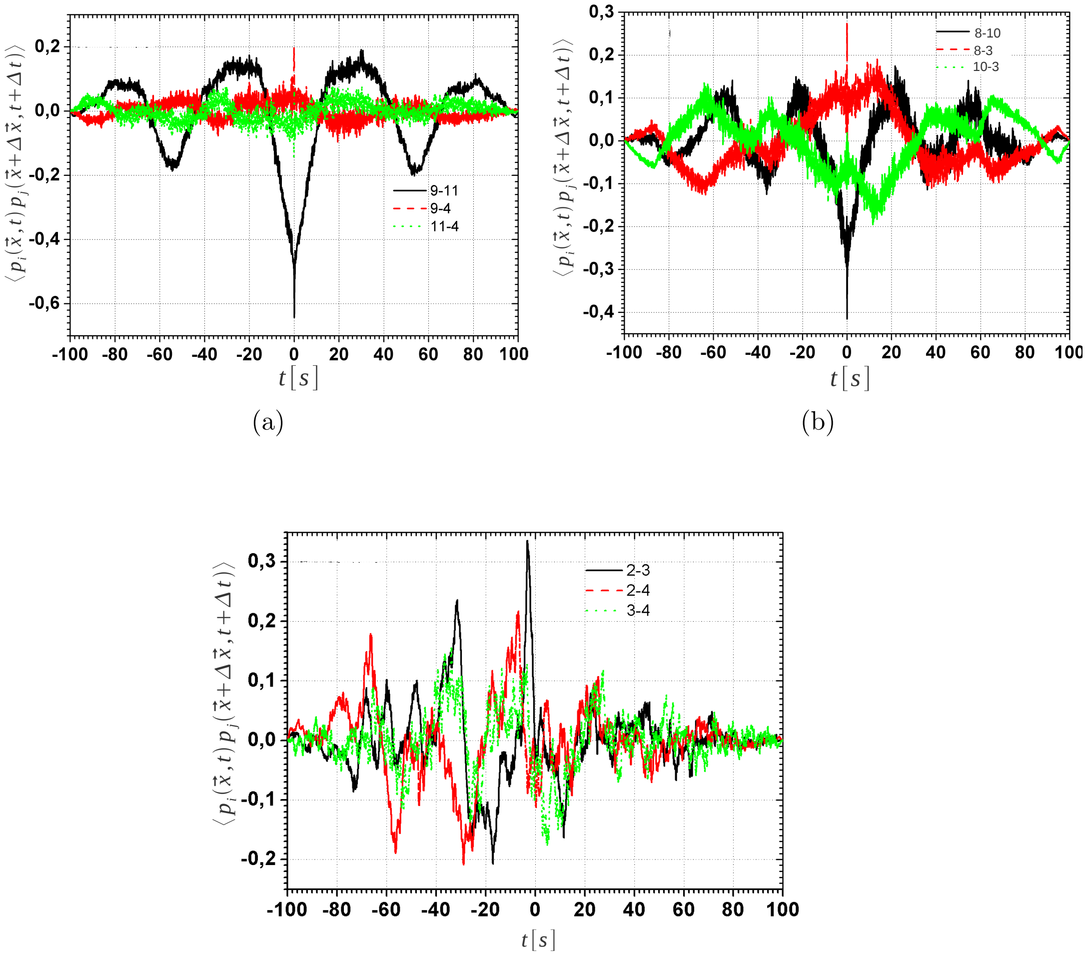

(a) (b)

(c)

Fig. 6.30: Cross-correlation of pressure fluctuations for different positions inside a single dimple at $\mathrm{Re}_d = 40000$.

the main flow. The drastic alternation reveals a time range of the vortex shifting up to $16s$ from cross-correlation of location $9-11$ which confirms the previous observations. The cross-correlation coefficients $R_{9,11}$ and $R_{8,10}$ show a high magnitude and are negative when the time switching period Δt tends to be zero. This implies, that both pressure signals are of opposite signs which significantly represents the appearance of opposite-of-phase motion inside the dimple. When the time shifting period Δt is increased to more than $15s$ both cross-correlation coefficients become positive which additionally underlines the changing of the vortex axis.

The cross-correlation coefficients in flow direction show a different distribution. First, the coefficients are positive for small time differences Δt and decay rapidly. Second, for positive time differences the correlations coefficients are found to be

very small whereas when time shifting Δt becomes negative, a clear dependence of the pressure signals can be identified. The physical reason for such behavior can be found in the flow direction inside the dimple. Within the recirculation zone the fluid moves against the main flow direction, thus only a correlation of pressure signals $R_{2,4}$ can be found for previous times in position 4 to position 2.
The energy spectra of the pressure signals from different locations inside the dimple are presented in Fig. 6.31.

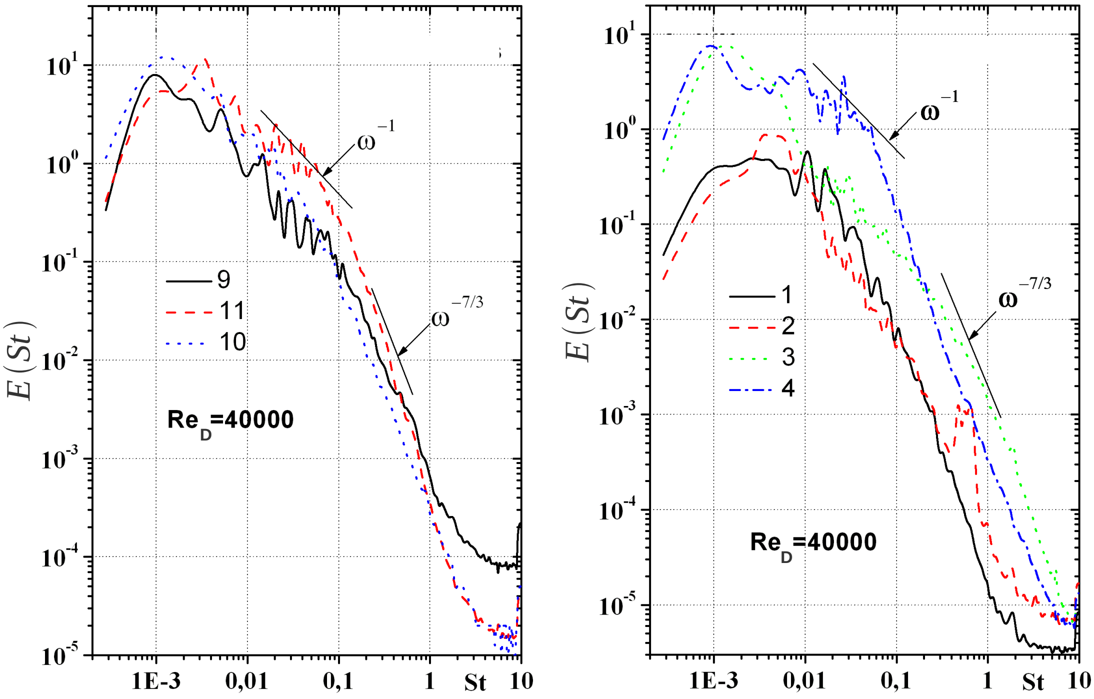

(a) (b)

Fig. 6.31: Energy spectra of the pressure for different positions inside the dimple for at $\mathrm{Re}_d = 40000$.

The typical slope of ω^{-1} and $\omega^{-7/3}$ can be reproduced within the energy spectra of the pressure fluctuations at the wall which can also be found in DNS data published by Kim [50] for a turbulent channel flow at $\mathrm{Re}_\tau = 185$. The energy spectra for positions 9, 10 and 11 do not change qualitatively, but the magnitude of fluctuations in position 11 is slightly be higher than for the others compared in Fig. 6.31 *a*. It is interesting to note, that the pressure fluctuations have a peak at a Strouhal number St = 0.0025 for position 11 and at a Strouhal number St = 0.0015 for position 9 what is in accordance with the switching frequency of the asymmetric vortex structure inside the dimple found from numerical simulations. The energy spectra of the pressure fluctuations at positions in axial direction (see Fig. 6.31 *b*) shows that the magnitudes at the positions 3 and 4 are higher than for the positions 1 and 2 since the main flow attaches the dimple surface at the downstream side. It is interesting to note that the peak for the positions 3 and 4 are at the same range as for position 1 and 2 and reveal a corresponding Strouhal number of around $\mathrm{St} = 0.001$ which is found to be smaller than for positions 9 and 11 respectively since at the midplane positions the switching of the vortex occurs twice.

All performed measurements including dye visualizations, LDA and pressure measurements represent the strong asymmetry of the vortex structure inside the dimple. The alternation of the inclination angle of the vortex axis could be observed using time resolved measurement techniques. Hence, the experimental observations confirm the numerical results obtained from LES for clarification of the instantaneous flow structures inside the spherical dimple. Moreover, the predicted steady flow structure within RANS calculations could be disproved. Frequency analysis of time signals from measurements and LES reveal the same frequencies concerning the shifting of the asymmetric vortex structure whereas for both methods its alternation occurs not with a constant period but rather was found to be intermittent.

6.4 POD analysis

Three dimensional discrete POD analysis is carried out on LES pressure and velocity fields to identify spatio-temporal structures hidden in the random fluctuations. The POD method has been briefly introduced in chapter 4. Since the method requires high computational resources to calculate the spatial correlation tensor $R_{ij}(\mathbf{x}, \mathbf{x}^{'})$, the computational domain is downsized to the area of $z/d = 1.5$ and $x/d = 2.5$ around the spherical dimple because the focus in this work is placed on the behaviors of the separated shear layer and asymmetric vortex formations inside the dimple and not on the plane channel flow. The downsizing will reduce the computational time significantly.

Eigenvalues

A priori the number of snapshots over the selected time range, which are necessary to capture all relevant flow processes, are not known. From the previous calculations it has be shown, that the switching of the asymmetric structure appears within a time range of $5s$ to $20s$. But due to the limited computational resources, only 2600 samples with a time interval of $\Delta t = 0.005s$ (equal to $13s$ of realtime) have been selected for the POD analysis. The mean values are substracted from the current field as described in section 4.4. Hence, the sum of the eigenvalues $\lambda^{(n)}$ in terms of the velocity represents the kinetic energy. Fig. 6.32 shows the distribution of the eigenvalues for the first 1000 modes for the decomposed pressure and velocity field.

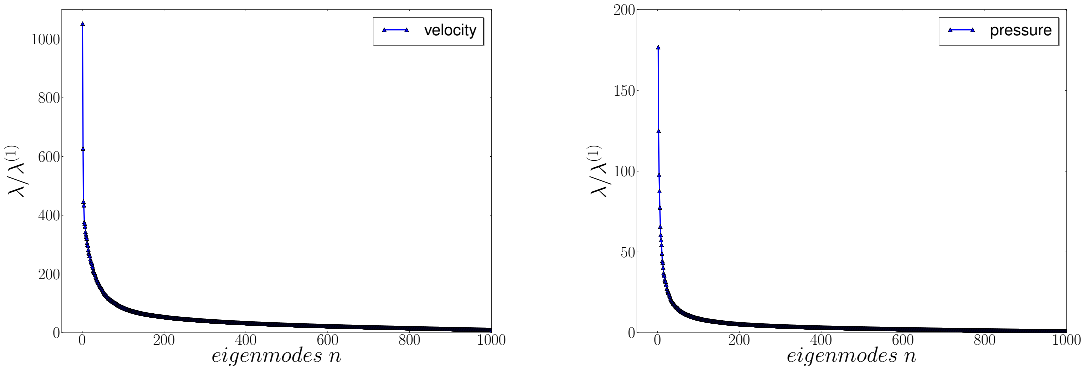

(a) (b)

Fig. 6.32: Energy distribution of the eigenvalues for the velocity and pressure eigenmodes.

The decay of the velocity and pressure eigenvalues remains very rapid. The collective contribution of the energy shows that 173 modes for the velocity and 112 modes for the pressure are needed to capture at least 50% of the total energy. It is preferable for POD decomposition to capture most of the energy within the first modes. As it can be seen from the energy decay, the first three modes are dominant for the velocity and pressure containing significant larger energy than the following modes. Therefore, one can conclude that the first three eigenmodes represent significant flow features inside the single dimple.

Eigenmodes

The streamline patterns of the first four eigenmodes of the velocity are presented in Fig. 6.33.

The structure corresponding to the first eigenmode $\Phi_u^{(1)}$ looks like a “tornado” taking its origin inside the dimple and penetrating into the channel. This kind of structure can be interpreted as a tornado-like structure or a so called mono cell structure analogously to the structure described by Isaev [42]. The structure is centered at the midpoint of the cavity and rotates around the y-axis normal to the channel surface. It transports the fluid from the dimple into the channel flow at an angle of approximately $\alpha = 30°$ towards the channel wall. The streamlines coming into the dimple from the adjacent plate surface indicate clearly, that the structure

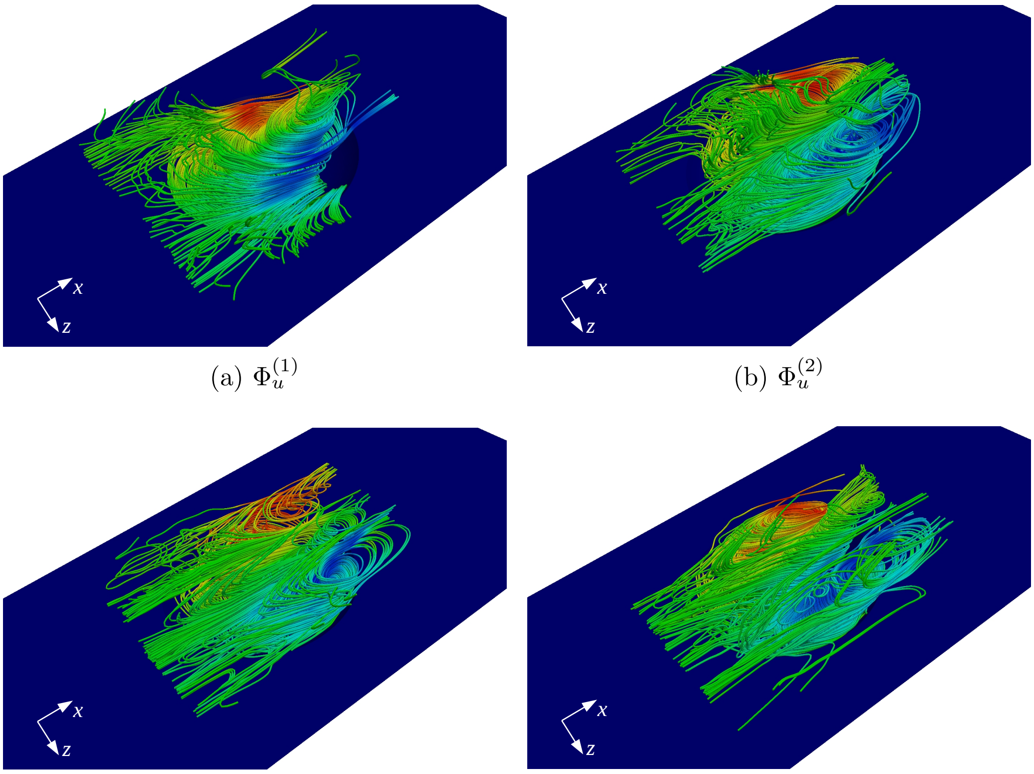

(a) $\Phi_u^{(1)}$ (b) $\Phi_u^{(2)}$

(c) $\Phi_u^{(3)}$ (d) $\Phi_u^{(4)}$

Fig. 6.33: Streamlines of the spatial eigenmodes n for the decomposed velocity.

has a significant impact on the flow inside and outside the dimple. Moreover, it obviously causes an increase of the heat transfer efficiency since the fluid is steadily moving out keeping temperatures difference high inside the dimple. The structures corresponding to the modes $\Phi_u^{(2)}$, $\Phi_u^{(3)}$ and $\Phi_u^{(4)}$ can be seen also as tornado like spatial structures. In contrast to the first mode structure they are symmetric towards the midplane. Hence, all high energy containing structures reveal a permanent outflow of the dimple which is preferable in terms of heat transfer by transporting the hot fluid out of the dimple.

The Fig. 6.34 represents the iso-surfaces of the first four pressure eigenmodes.

The roll-up processes inside the shear layer arising from the recirculating flow and the main channel at the dividing surface are clearly represented by the pressure eigenmodes $\Phi_p^{(2)}$, $\Phi_p^{(3)}$ and $\Phi_p^{(4)}$. The different stages of the shear layer structures are covered by the shifted structures in flow direction of mode $\Phi_p^{(2)}$ and $\Phi_p^{(3)}$. However, the mode $\Phi_p^{(1)}$ shows an interesting structure. Four strong cores arise inside the dimple where pressure values are of opposite signs at downstream and upstream side respectively. Appearance of these cores can be explained by the analysis of the temporal correlation coefficients $a^{(n)}$ of the first velocity and the first pressure mode.

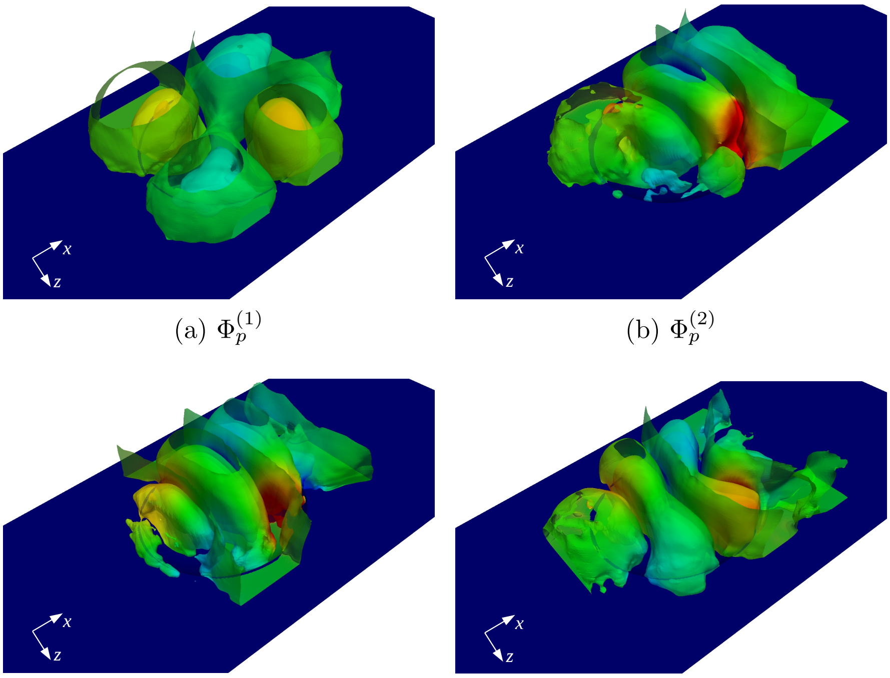

(a) $\Phi_p^{(1)}$ (b) $\Phi_p^{(2)}$

(c) $\Phi_p^{(3)}$ (d) $\Phi_p^{(4)}$

Fig. 6.34: Isosurfaces of the first four pressure eigenmodes.

The temporal correlation coefficients for the first four eigenmodes of the pressure and velocity are presented in Fig. 6.35 (a) and (b).

A drastic alternation from negative to positive values can be observed for the temporal coefficient $a^{(1)}(t)$ for the velocity. Physically, the change of the sign of $a^{(1)}(t)$ shows that the first eigenmode $\Phi_u^{(1)}$ steadily changes its rotation (see Fig. 6.33 (a)). To a certain extent, the results are consistent with the results obtained from the direct analysis of structures from LES and experiments. The switching of rotation direction can be detected after six seconds of realtime in Fig. 6.35 (a). The change of the rotation direction of the first eigenmode $\Phi_u^{(1)}$ is an additional explanation of long period oscillations with the opposition-of-phase motion. It leads to periodic transversal fluctuations and outbursts at the downstream side of the cavity which have been observed in measurements and LES. However, it should be noted that such structure cannot be seen in the streamline patterns. The so called tornado-like structures widely mentioned in the literature seem to be a fiction rather than real existing coherent structures. The first mode structures reflect therefore a collective combination of vortices of different size and orientations producing the self-sustained oscillations conducted with the opposition-of-phase motion. Coming back to the explanation of the four pressure cores presented in Fig. 6.34 (a). The normalized correlation coefficients of the first eigenmode $\Phi_u^{(1)}$ and $\Phi_p^{(1)}$ are presented

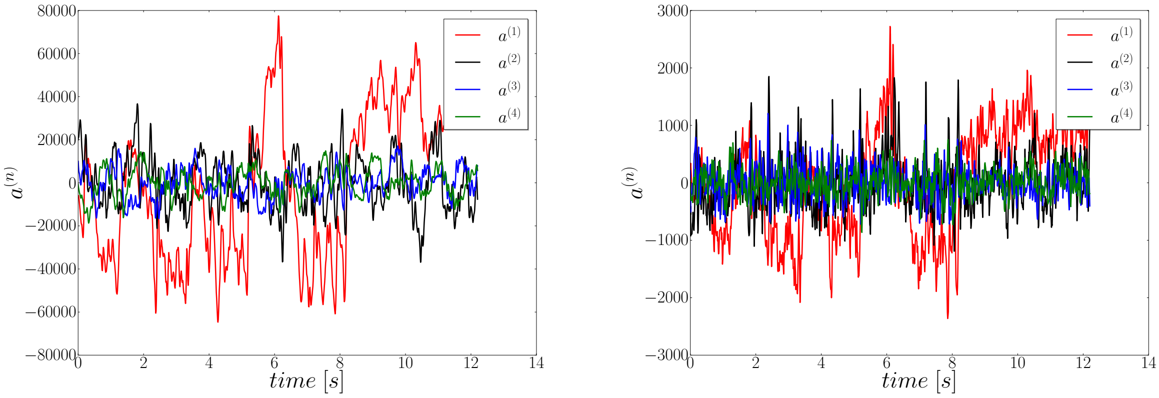

(a) velocity (b) pressure

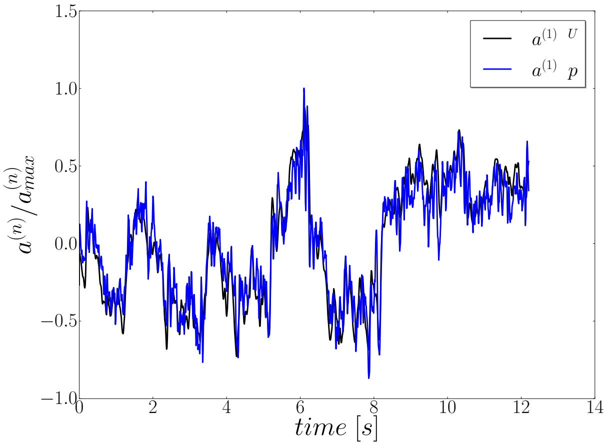

(c) correlated time coefficients

Fig. 6.35: Temporal correlation coefficients $a^{(n)}(t)$ for the first modes of the velocity and pressure field (a), (b). Normalized correlation coefficients of the first modes of pressure and velocity (c).

in Fig. 6.35 (c). A strong correlation between temporal coefficients of both modes reflects the direct relation between the two eigenmodes of the pressure and velocity. The velocity eigenmode $\Phi_u^{(1)}$ shown in Fig. 6.33 (a) causes the pressure field structure $\Phi_p^{(1)}$ shown in Fig. 6.34 (a) since the rotation of $\Phi_u^{(1)}$ changes in time.

Conclusion

The POD analysis confirms, that the flow is characterized by the instability of the asymmetric vortex structure inside the dimple and the instability of the shear layer structures. The first eigenmodes of the velocity and pressure contain significantly larger energy in comparison with the following modes and thus represent the main

flow features. The changing of the asymmetric vortex structure towards the main flow can be observed in the streamline patterns and iso-surfaces as well as in the temporal coefficient $a^{(1)}(t)$ for the velocity and pressure. The shifting of the asymmetric vortex structure is found as the overall dominant process appearing as tornado-like structure inside the dimple changing its rotation in time. The corresponding pressure mode shows four concentrated cores inside the dimple with opposite signs in respect to the current direction of the asymmetric vortex structure. The eigenmodes $\Phi_p^{(2)}$, $\Phi_p^{(3)}$ and $\Phi_p^{(4)}$ of the pressure represent the shear layer instabilities with a spatial shifting of the characteristic roll-up structures in axial direction. The evolving structures inside the shear layer are convected downstream and impinge the downstream side of the dimple causing high heat transfer rates.
Hence, the eigenmodes underline and confirm the results of the direct analysis for the turbulent flow over a spherical dimple.

6.5 Heat transfer and pressure loss

The forgoing analysis was focused on the flow structures. To evaluate the overall performance of the heat exchanger configuration, integral values of pressure and friction loss and heat transfer rates have to be determined. Therefore, the values of the pressure and friction forces D_p and D_f from Eq. 2.55 and Eq. 2.56 and the integral heat transfer enhancement Nu_m (see Eq. 2.12) are determined using LES and RANS at a Reynolds number $\mathrm{Re}_d = 40000$. Surface integrated values have been use for the comparison of the heat transfer rates between dimples and the smooth channel. It concludes, that the increase of the surface due to the dimple geometry is *not* taken into account for the integral values in terms of heat transfer. Therefore, the presented results of the heat transfer enhancement include only its increase from vortex formations. An area of about $(x/d = 2.5) \times (z/d = 1.5)$ is chosen for integration presented on the left side of Tab. 6.6. The selected area includes the heat transfer rates inside and behind the dimple and neglect the area upstream the dimple.

The integral values obtained from LES show a strong grid dependency in respect to flow resistance and heat transfer. The pressure distribution on the solid walls attains a maximum pressure resistance of $D_p/D_c = 1.721$ in case of LES(A3) and $D_p/D_c = 1.898$ in case of RANS where the value D_c covers the friction forces of smooth channel wall. The increase of the pressure resistance of about 72% determined in case of LES is fairly high for the investigated dimple configuration and totally contradicts to the often proposed thesis using dimples for drag reduction. Further it is noticeable

Tab. 6.6: Comparison of pressure and shear forces (D_p and D_f) for the dimpled wall and enhancement of heat transfer in terms of area-averaged Nusselt number Nu_m in comparison to a flat plate for the selected area of average (left) for a single spherical dimple at $\mathrm{Re}_d = 40000$.

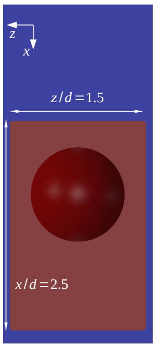

	LES (A1)	LES (A2)	LES (A3)	RANS
D_p/D_c	1.636	1.679	1.721	1.898
D_f/D_c	0.772	0.881	0.914	0.921
$\mathrm{Nu}_m/\mathrm{Nu}_{m0}$	0.959	1.048	1.141	1.259

that the determination of the pressure resistance could not be estimated in the experiments using measurements only at the baseline in streamwise direction since the flow is not fully developed. In contrast to the significant increase of the pressure resistance, a decrease for the friction resistance could be observed. The friction force D_f ranges from $D_f/D_c = 0.772$ to $D_f/D_c = 0.954$ with mesh refinement in case of LES where RANS predict a ratio of $D_f/D_c = 0.921$. The friction values are fairly lower than for a smooth wall due to the existing recirculation zone inside the dimple.

The results of integral heat transfer rates have to be taken into account for evaluation of the heat exchanger performance. The integral Nusselt number Nu_m compared to a smooth wall for the selected area presented in Tab. 6.6 ranges between $\mathrm{Nu}_m/\mathrm{Nu}_{m0} = 0.959$ for the mesh A1 to $\mathrm{Nu}_m/\mathrm{Nu}_{m0} = 1.142$ for the A3 in case of LES whereas RANS results yield to an increase of $\mathrm{Nu}_m/\mathrm{Nu}_{m0} = 1.259$. As explained in the previous section, the results obtained from RANS are more trustful than in case of LES since the needed grid resolution for LES in terms of heat transfer exceeds the available computational resources.

The reason for weak performance of the heat transfer enhancement arises in the definition of the established test case. Due to the fact that the fluid is heated up only at a small distance upstream the dimple, the temperature boundary layer is still small including already high heat transfer rates even for the smooth wall. Thus, the influence of the dimple to increase heat transfer rates becomes fairly small as it is presented in Tab. 6.6. Further the numerical simulation of an evolving temperature boundary layer is still complicated in terms of time resolved inflow conditions and requires high grid resolution in case of LES to resolve the gradients inside the temperature boundary layer.

In summary, the integral results show that the thermo-hydraulic performance of the current setup is very poor. The increase of the heat transfer of about 25.9% (in case of RANS) compared to a smooth wall does not reflect the real potential of dimples to enhance heat exchanger performance. To analyze the performance of a single spherical dimple in fully developed temperature boundary layers further simulations have been carried out. Hence, the precursor method to generate inflow conditions is not only used for the velocity but also for the temperature. The calculation of the heat transfer becomes much more simpler in respect to grid resolutions for LES since the temperature gradients are not that sharp as for an evolving temperature boundary layer. LES calculations have been performed using the grid (A3). Since the temperature acts as passive scalar, the pressure and friction resistance remain constant for a fully developed temperature boundary layer whereas only the results for the heat transfer rates are changed. Simulations for a fully developed boundary layer show an increase of heat transfer of about $\mathrm{Nu}_m/\mathrm{Nu}_{m0} = 1.67$ compared to an equivalent smooth wall which is significantly larger than $\mathrm{Nu}_m/\mathrm{Nu}_{m0} = 1.142$ as it is the case for an evolving temperature boundary layer.

Another interesting point is the role of the asymmetric structures inside the dimple. It was found from time resolved heat flux analysis at the heated channel wall, that the heat transfer is mainly dominated by the direct attachment of the flow and its vortex shedding at the downstream side of the dimple. However, the shifting of the asymmetric structure towards the streamwise direction could not be detected in the time history of the heat transfer rates during the LES simulations. Thus, a significant enhancement due to the shifting of the asymmetric vortex structure could not be observed. Nevertheless, the vortex shifting drives the hot fluid out of the dimple which is found to be preferable in terms of heat transfer enhancement and also to prevent fouling effects.

6.6 Summary

Comparison of numerical results obtained from LES and RANS with the performed experiments and data published in literature confirmed, that the established methods are capable of predicting flow physics and heat transfer rates in a channel with a single spherical dimple with a satisfactory accuracy. LES reveals the presence of self-sustained oscillations with opposite-of-phase motion inside a single dimple. The same conclusion has been drawn in measurements using LDA technique, visual observations using dye injections and pressure measurements. Analysis of flow structures using instantaneous streamline patterns and pressure isosurfaces shows clearly the presence of an asymmetric vortex structure which is inclined in respect to the incoming flow. Although the instantaneous flow is asymmetric, however, the flow averaged over a sufficiently long time period is nearly symmetric. In this context LES and measurement results contradict to RANS simulations which predict the asymmetry even in the averaged flow pictures. Moreover, the reason for the shifting of the asymmetric vortex structure is determined within the shear layer structures and its direct impact on the attachment point of the incoming fluid at downstream side of the dimple. The POD analysis revealed the formation of tornado-like spatial structures inside the dimple. The first eigenmode of the velocity corresponds to a mono structure steadily changing its rotation in time. The structure clearly reflects the mono cell structure inside the dimple and its switching in time. The second mode corresponds to a twin structure located symmetrically inside the dimple. Iso-surfaces of the pressure eigenmodes represent the formation of a shear layer arising between the main channel and recirculating flow inside the cavity.

In respect to heat transfer enhancement, the asymmetric vortex structures are preferable in terms of steadily driving the hot fluid out of the dimple. A significant increase of the heat transfer rates due to the long period oscillations could not be found since the time scale of the heat transfer mechanism is much smaller than shifting time of the asymmetric vortex structure. The augmentation of heat transfer is relatively small ($\mathrm{Nu}_m/\mathrm{Nu}_{m0} = 1.142$) compared to smooth surface for temperature boundary layer evolving shortly upstream the dimple. In contrast, when the temperature profile is fully developed, the heat transfer can be increased up to $\mathrm{Nu}_m/\mathrm{Nu}_{m0} = 1.67$.

7 Heat transfer and flow structures of dimple packages

Vortex structures and heat transfer mechanism of turbulent flow over a staggered dimple array in a narrow channel have been investigated using numerical and experimental methods. LES calculations are performed for Reynolds numbers $\mathrm{Re}_d = 10000$ and $\mathrm{Re}_d = 20000$ and are analyzed in details to get a deep insight into flow physics and heat transfer mechanismn. Simulations are verified by equivalent experiments using LDA and pressure measurements in combination with DNS data published by Moser et al. [78] and Kawamura [47] for a smooth channel. In addition, the POD method is applied on resolved LES fields to identify spatial-temporal structures hidden in the random fluctuations of the pressure and velocity fields.

7.1 Definition of the package standard case

A new test section was designed where about 700mm of the lower channel wall are exchangeable to vary the dimple configurations. The geometric parameters and the standard dimple arrangement are sketched in Fig. 7.1. The arrangement of spherical dimples and their geometric properties are chosen similar to these used in

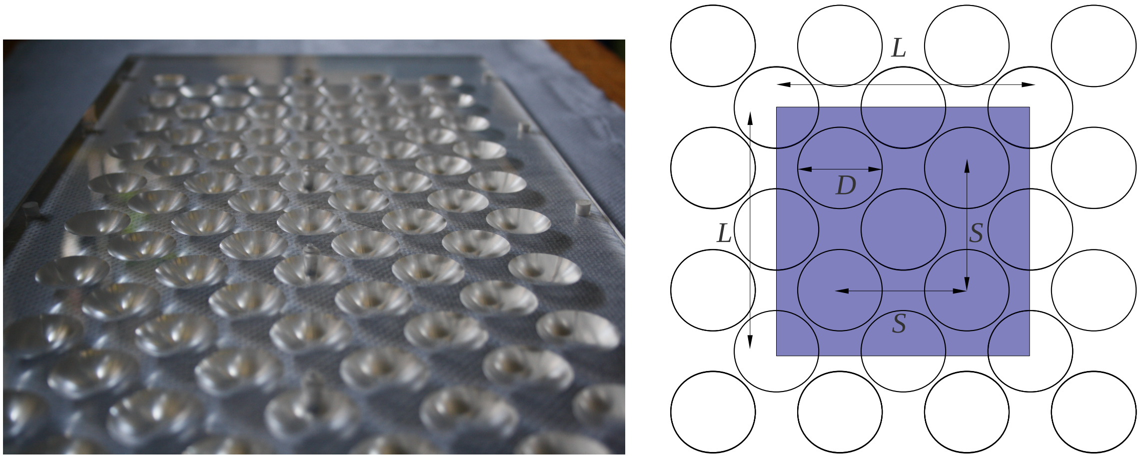

Fig. 7.1: Geometry specifications of the staggered dimple arrangement.

experiments performed by Ligrani [61] and Mahmood [70]. Tab. 7.1 summarizes the geometrical dimensions. About 30 rows of dimples in flow direction and five rows of dimples in spanwise direction were drilled into the lower wall to ensure the fully developed state of the flow within the measurement section. LDA measurements are performed at different positions to analyze the flow structures inside and outside the dimples and for further validation of the numerical methods.

Tab. 7.1: Geometric parameters of the standard dimple package.

d	h/d	H/d	L/d
23 mm	0.26	0.652	4.66

7.2 Reference case: periodic channel flow

To ensure reliability of the applied numerical methods, the turbulent flow between two parallel smooth plates, commonly known as turbulent channel flow, have been investigated. The case is well-known in literature and is mainly used for validation of numerical methods. The geometric dimensions $4.66L/H \times H \times 4.66L/H$ of the plane channel have been chosen similar to geometric parameters of the selected area of the dimple packages. The simulations are carried out at Reynolds number $\mathrm{Re}_H = 13043$ ($\mathrm{Re}_\tau = 375$). The mean and rms values are discussed and compared to analytic correlations and to DNS computations from Moser et al. [78] for the Reynolds number $\mathrm{Re}_\tau = 395$. Since the reference data from Moser et al. [78] is not exactly comparable to the present case due to the small Reynolds number difference, it can only be used for qualitative evaluation of the results.

Geometry and boundary conditions

The domain of the test case consists of two parallel walls with infinite dimensions. Only a sub-domain is included for numerical simulation where periodic boundary conditions are applied in streamwise and spanwise direction. Fig. 7.2 presents the computational domain.

In contrast to the previous investigations for a single dimple, the temperature profile is fully developed. It gives the possibility to apply periodic boundary conditions for the temperature as well. Hence, the precursor method becomes unneeded what reduces the computational resources enormously by keeping the computational domain small. The temperature is set constant to $T^+ = 1$ at the lower and constant

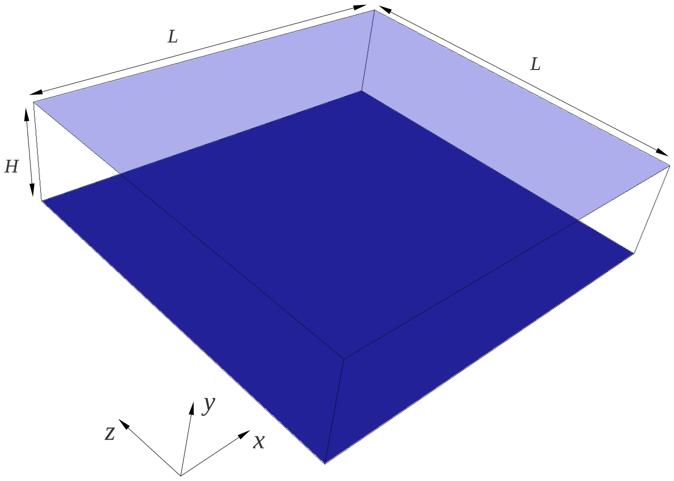

Fig. 7.2: Computational domain of the turbulent flow between two parallel plates.

to $T^+ = 0$ at the upper channel wall. A precise definition of the turbulent channel flow has been described by Jahnke [43] and Moser et al. [78]. Tab. 7.2 summarizes the applied boundary conditions.

Tab. 7.2: Boundary conditions for LES of fully developed turbulent flow in a plane channel.

	upper wall	lower wall	inlet	outlet
pressure	$\partial \overline{p}/\partial n = 0$	$\partial \overline{p}/\partial n = 0$	periodic	periodic
velocity	$\overline{u}_i = 0$	$\overline{u}_i = 0$	periodic	periodic
temperature	$\overline{T^+} = 0$	$\overline{T^+} = 1$	periodic	periodic

Grid resolution

Two different mesh resolutions have been investigated to evaluate the needed grid size. The mesh properties are given in Δx_i^+ values based on the channel height H and the Reynolds number Re_τ calculated from DNS results presented in Tab. 7.3.

The mesh resolution is homogeneous in streamwise and spanwise direction. A stretching of the grid points normal to the wall is applied whereas the ratio of largest to smallest grid cell in wall normal direction is set to a factor of 7.5. Since wall resolved LES computations were conducted, it was important to place at least three grid points into the viscous sub-layer. For identification of the statistically steady state, the Reynolds stresses are averaged and evaluated on the fly during the simulation. Moreover, the statistic values are averaged in homogeneous directions

Tab. 7.3: Different grid resolutions for LES of fully developed turbulent flow in a plane channel.

Mesh	$N_x \times N_y \times N_z$	Δx^+	Δy^+_{min}	Δz^+
D1	$128 \times 64 \times 128$	14.4	0.42	14.4
D2	$256 \times 80 \times 256$	7.2	0.14	7.2

(streamwise and spanwise).

Results

The profiles obtained from LES have been compared to DNS data provided by Moser et al. [78] for the velocity and to DNS data published by Kawamura [47] for the temperature. The DMM is used as closure model. It was shown from previous calculations (see section 6.2), that the best results have been achieved using the DMM for closure of the filtered momentum and temperature transport equations in comparison to other models.

The mean values of the velocity and temperature are presented in Fig. 7.3 and Fig. 7.4 respectively.

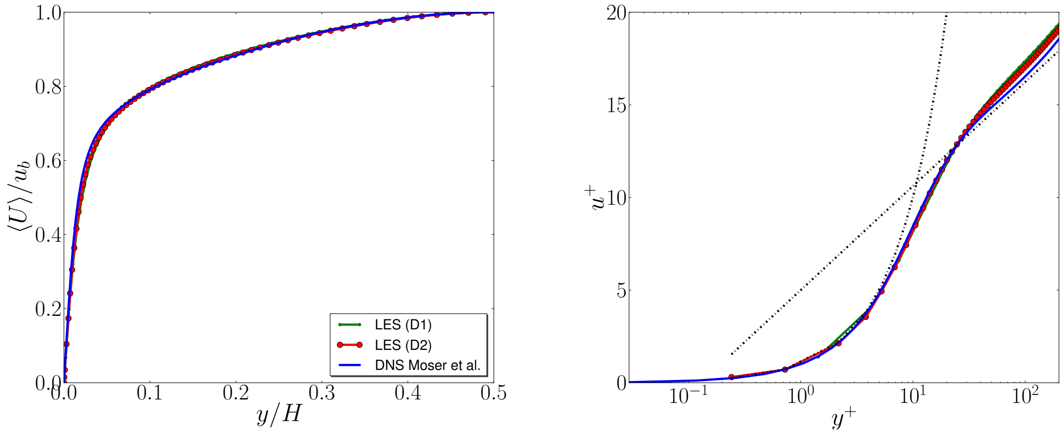

Fig. 7.3: Averaged velocity profiles normalized by the bulk velocity u_b using different mesh resolutions for the turbulent channel flow at $\mathrm{Re}_H = 13043$.

The mean profiles of velocity and temperature show no discrepancies to DNS results published by Moser et al.[78] and Kawamura [47] for both investigated grid resolutions. To analyze the near wall behavior, the mean values of temperature and velocity are plotted over y^+ values in semi-logarithmic axis. It is obviously that

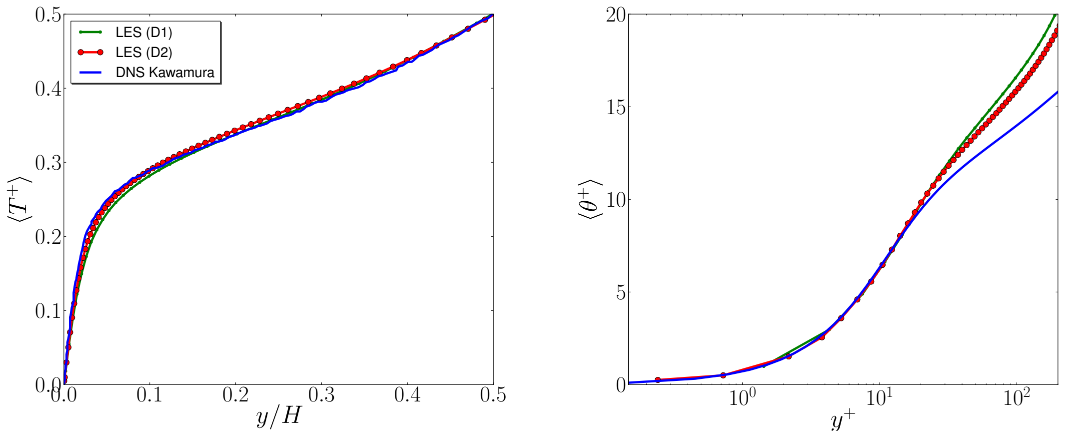

Fig. 7.4: Averaged temperature profiles using different mesh resolutions for the turbulent channel flow at $\mathrm{Re}_H = 13043$.

the mean profiles of the velocity match the DNS results in the near wall region. The viscous sublayer and the log-law region are well predicted using the DMM. Slight discrepancies can be found in the near wall region for the temperature profile. Whereas in the viscous sublayer the mean profile is in an excellent agreement to DNS results, some discrepancies can be observed in the turbulent region. However, a tendency towards the DNS results can be reached by increasing the mesh resolution. Nevertheless it has to be mentioned, that the LES results compare well with DNS profiles in the viscous sublayer which leads to an accurate prediction of the temperature gradients near the wall. The rms values of the velocity are presented in Fig. 7.5.

The rms values show qualitatively the same distribution as the DNS results. Again it should be noted, that the present calculations refer to the Reynolds number $\mathrm{Re}_\tau = 375$ which differs slightly to the DNS data at a Reynolds number $\mathrm{Re}_\tau = 395$. Thus, the profiles obtained from LES had to be slightly smaller than the predicted ones from DNS. The results show the expected tendency with only small differences between both mesh resolutions.

For analysis of the flow resistance and heat transfer, the integral values are compared to empiric correlations taken from the literature. Tab. 7.4 compares the results of the friction coefficient C_f obtained from numerical simulation and pressure measurements to empiric correlation proposed by Dean $C_f = 0.06138\ \mathrm{Re}^{-1/4}$.

The friction coefficients obtained by experiments and simulations over-predict the values calculated by Dean's formula with a maximal deviation of about 6.9%. It

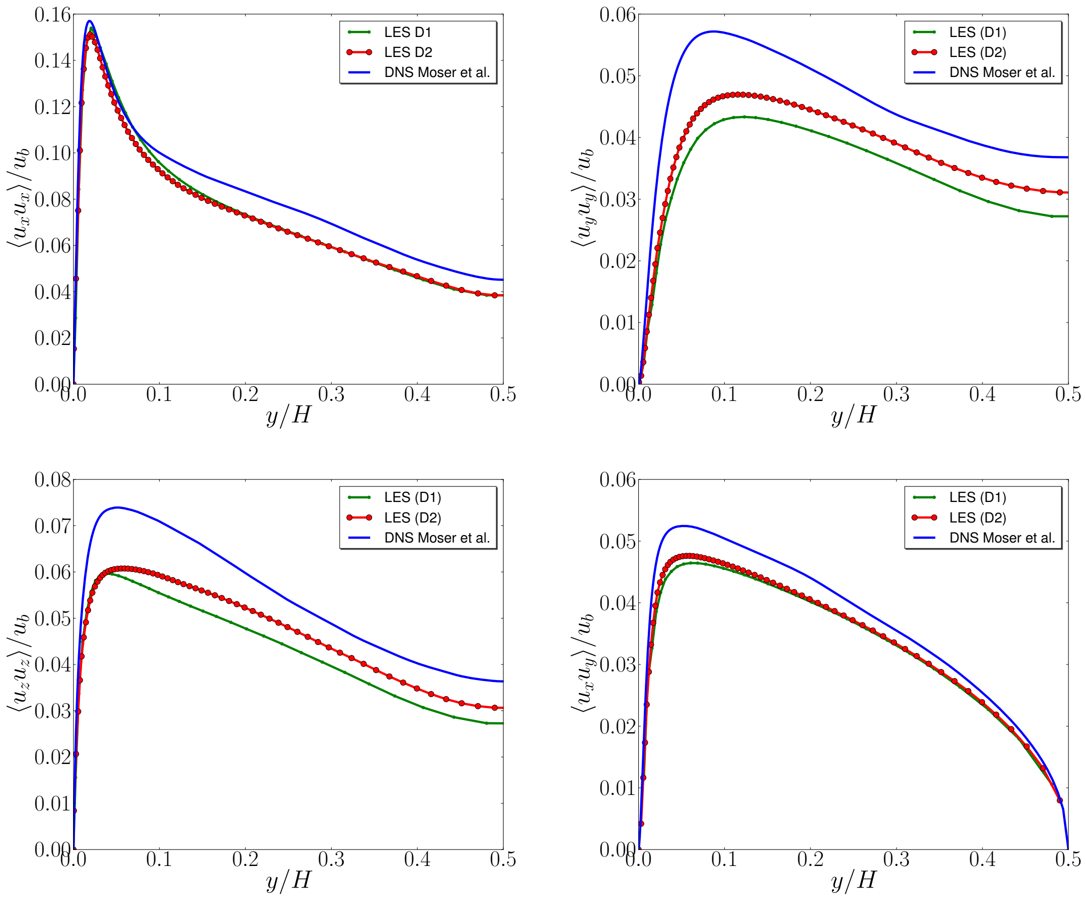

Fig. 7.5: Rms profiles using different resolutions for the turbulent channel flow at $\mathrm{Re}_H = 13043$.

Tab. 7.4: Comparison of the friction coefficient C_f obtained from LES and experiment to empiric correlations proposed by Dean for the turbulent channel flow at $\mathrm{Re}_H = 6521$ and $\mathrm{Re}_H = 13042$.

		C_f	Dean
$\mathrm{Re}_H = 6521$	LES (D1)	0.0724	0.06835
	LES (D2)	0.0681	
	Exp	0.0692	
$\mathrm{Re}_H = 13042$	LES (D1)	0.0614	0.05748
	LES (D2)	0.0591	
	Exp	0.0602	

shows that applied methods are capable of capturing the pressure loss inside a smooth channel.
Further the empiric correlations of Gnielinsky

$$Nu = \frac{(\xi/8)\ \mathrm{RePr}}{1 + 12.7\sqrt{\xi/8}\ (\mathrm{Pr}^{2/3} - 1)}(1 + (d_h/l)^{2/3}) \tag{7.1}$$

and Dittuis-Boelter

$$Nu = 0.023\ \mathrm{Re}^{0.8}\ \mathrm{Pr}^{0.4} \tag{7.2}$$

have been used for comparison of the heat transfer rates and are summarized in Tab. 7.5.

Tab. 7.5: Comparison of Nusselt number Nu_m obtained from LES with empiric correlations from Gnielinsky and Dittuis-Boelter for a turbulent channel flow at $\mathrm{Re}_H = 6521$ and $\mathrm{Re}_H = 13042$.

		Nu_m	Boelter	Gnielinsky
$\mathrm{Re}_H = 6521$	LES (D1)	24.47	22.39	24.04
	LES (D2)	23.78		
$\mathrm{Re}_H = 13042$	LES (D1)	39.58	38.97	38.87
	LES (D2)	39.12		

Discrepancies between the integral heat flux obtained from the numerical simulation compared to the empiric correlations are within 1% range which underlines the quality of the present calculations. To summarize the results, the channel flow calculations reveal a fairly good agreement to DNS data and empiric correlations.

7.3 Results

7.3.1 Validation of the numerical model

The computational domain could not cover the whole experimental test setup consists with 30 rows of dimples in case of LES. Therefore, only a part of the domain within the fully developed range is extracted. Fig. 7.6 presents the computational domain.

The length and width of the domain is set to $L/H = 4.66$. The diameter d of the dimple was kept constant at $d = 23mm$ whereas in this work three different dimple depths $h/d = 0.196$, $h/d = 0.26$ and $h/d = 0.326$ have been investigated. However, the geometrical parameters of the spherical dimple analyzed in the previous section

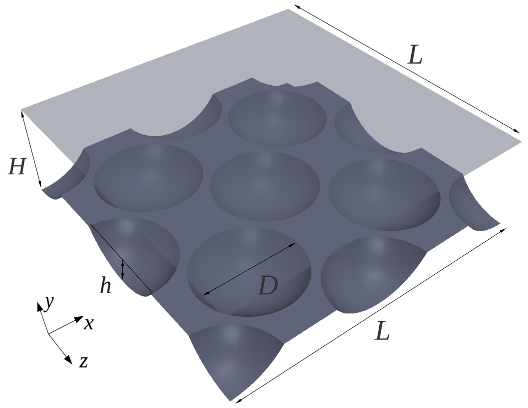

Fig. 7.6: Computational domain of a dimple package at the lower channel wall for LES.

could not be adopted for dimple packages due to the geometric limitations of experimental test section. The application of dimples with a print diameter of $d = 46mm$ inside a channel with a spanwise dimension of $200mm$ will allow a maximum of three dimples in a row. Numerical simulations based on URANS calculations from Isaev revealed, that the influence of the sidewalls on the flow field for this configuration cannot be neglected.
Since the analysis of the flow structures and heat transfer is in the foreground, the size of the computational domain should be chosen carefully. In most previous works (see Elyyan [18]), time resolved computations of heat exchangers using dimples or protrusions have been performed where either one half or only one whole dimple was included in the computational domain. The reduction of the domain undertaken in these works is not acceptable for the present work since the integral values differ significantly with variation of the domain size. It was shown, that the generated vortex structures inside the dimpled channel can have large length scales which cannot be captured in small domains. Therefore, an enlarged domain including several dimples was chosen to ensure a free evolution of the vortices.

No slip boundary condition were applied at the lower and the upper walls for the velocity whereas the temperature is fixed to $T^+ = 1$ at the lower (hot surface) and to $T^+ = 0$ at the upper channel wall (cold surface). To drive the flow with a constant massflow rate, the overall losses are calculated within the domain and simply added as driving force into the momentum equation. The standard Reynolds number $\mathrm{Re}_d = 20000$ calculated by the dimple diameter corresponds to a Reynolds number $\mathrm{Re}_H = 13043$ based on the channel height H.

On the basis of the turbulent channel flow calculations, a block structured curvilinear grid consisting of 13’196’000 cells was chosen for further investigations of the dimpled channel. Grid dependency studies showed, that a high mesh resolution is required to capture all relevant flow physics like vortex shedding at the trailing edge for a correct estimation of the local heat transfer rates. To escape numerical errors caused by large aspect ratios of the grid cells, mesh motion functionality based on a grid diffusion equation was applied. At first, a block-structured grid is generated for flat channel and than at the second step, the mesh is stretched onto the dimpled surface. As result, the grid lines nearly follow the streamlines inside the dimples and large aspect ratios of the grid cells are avoided. Special attention is paid to the resolution of the dimple edge to resolve the flow separation and shear layer gradients with a proper accuracy. Since a wall resolved LES is applied, the $y^+ \leq 1$ condition for the first grid point was satisfied to ensure a correct estimation of the local heat flux.

The velocity profiles obtained from LES are compared to LDA measurements. Experimental velocity profiles at different positions in flow direction showed, that the differences of the velocity profiles inside and outside the dimple between these positions become very small after the tenth row of dimples. This observation is in accordance with Ligrani [60], who found the fully developed state of the flow after the 13th row of dimples. Therefore, the experimental profiles are taken from the 18th row of dimples which is definitely within the fully developed range. The comparison of the velocity profiles obtained from LES and LDA measurements inside the dimple for two Reynolds numbers is presented in Fig. 7.7.

Mean and rms profiles of the velocity at $\mathrm{Re}_H = 6521$ show a good agreement between experiment and simulation. However, the rms values obtained from LES are twice as high as the experimental ones at Reynolds number $\mathrm{Re}_H = 13042$. Most probably reason for this discrepancy is the non-sufficient accuracy of measurements. Indeed, the rms values obtained from LES for a smooth channel flow at $\mathrm{Re}_H = 13042$ reveal a high peak near the upper channel wall with a strong decrease towards the center of the channel. The strong decrease of fluctuations could not be observed when dimples are placed at the lower wall. Hence, it can be assumed that the perturbations are increased in the whole channel when dimples are placed at the lower wall which leads to a significant enhancement of the mixing processes. Since the measurements could only be performed for isothermal flow, the verification of the heat transfer rates has been carried out using experimental data published by

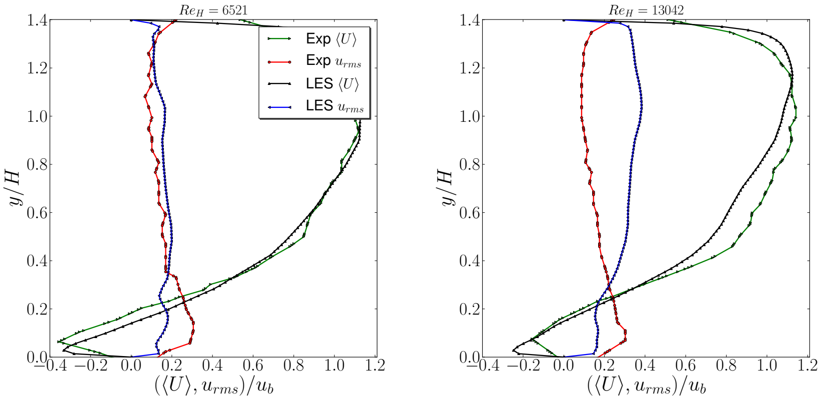

Fig. 7.7: Velocity and rms profiles across the channel height for dimples with a ratio of $h/d = 0.26$ at two different Reynolds numbers in the fully developed range. $y/H = 0.0$ is located at the dimple bottom.

Ligrani [60] presented later in section 7.5.

7.3.2 Vortex structures

The most detailed experimental studies of unsteady flow phenomena on dimpled packages have been performed by Ligrani [60]. Flow visualizations using smoke patterns revealed a primary vortex pair and two additional secondary vortices arising at the spanwise edges of each dimple. The visual results showed, that the typical vortex structures are symmetric and show a periodic behavior for dimples with a ratio $h/d = 0.2$ at $\mathrm{Re}_H = 1250$. For high Reynolds number flow the visualization using smoke injection becomes impossible due to the high mixing inside the channel. Unfortunately, these first valuable observations of an array of dimples have never been quantified properly and analyzed using modern non-intrusive measurement techniques and advanced numerical technologies like LES and DNS. To clarify the role of the vortex formations in respect to the heat transfer on staggered dimple packages, numerical simulations and velocity measurements have been performed in this work.
At first, the time averaged values are analyzed with variation of the dimple depth to investigate main flow features at a Reynolds number $\mathrm{Re}_d = 20000$. Fig. 7.8 presents the mean pressure distribution with slices of the mean velocity for different dimple depths.

The direct impact of the dimple geometry on the pressure field can clearly be seen at the lower channel wall where a symmetrical distribution towards the dimple center plane for all investigated dimple depths is present. The highest pressure values are

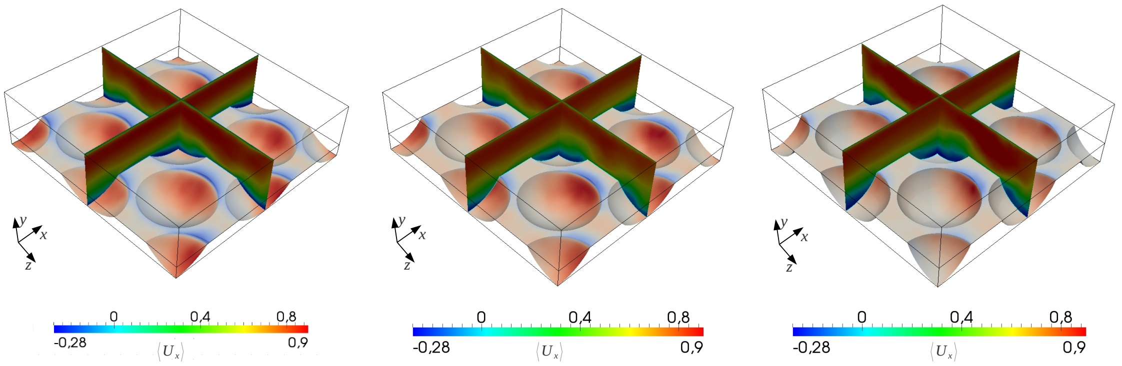

(a) $h/d = 0.196$ (b) $h/d = 0.26$ (c) $h/d = 0.326$

Fig. 7.8: Time averaged pressure distribution with slices of the mean velocity of dimple packages for various dimple depths at $\mathrm{Re}_d = 20000$.

found at the downstream side of the dimple due to the attachment of the incoming flow.

The commonly used vortex identification methods like λ_2 or Q criterion applied for the dimple package reveal that the flow inside the cavities is mainly dominated by small scale eddies. Fig. 7.9 showed the λ_2 and Q structures for the dimple $h/d = 0.26$ at a Reynolds number $\mathrm{Re}_d = 20000$.

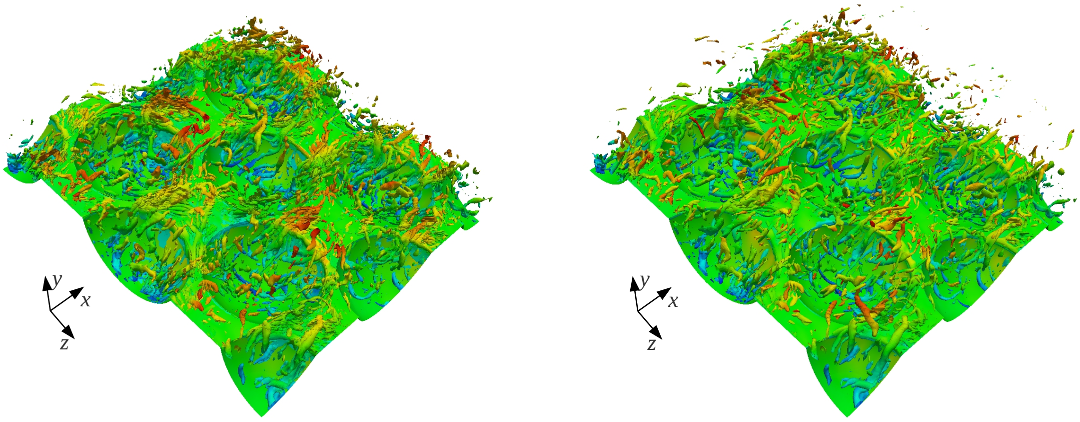

(a) λ_2 - structures (b) Q - structures

Fig. 7.9: Visualization of vortex structures using λ_2 and Q criterion for turbulent flow over a dimple package at $\mathrm{Re}_d = 20000$.

The instantaneous flow fields do not show the presence of large scale structures inside the cavities like for the single spherical dimple as shown in the previous chapter. Any kind of order is prevented due to irregular perturbations coming from dimples located upstream. However, some instantaneous cell patterns caused by dimples with different depths can be recognized in the streamline pictures averaged over 0.39s realtime presented in Fig. 7.10.

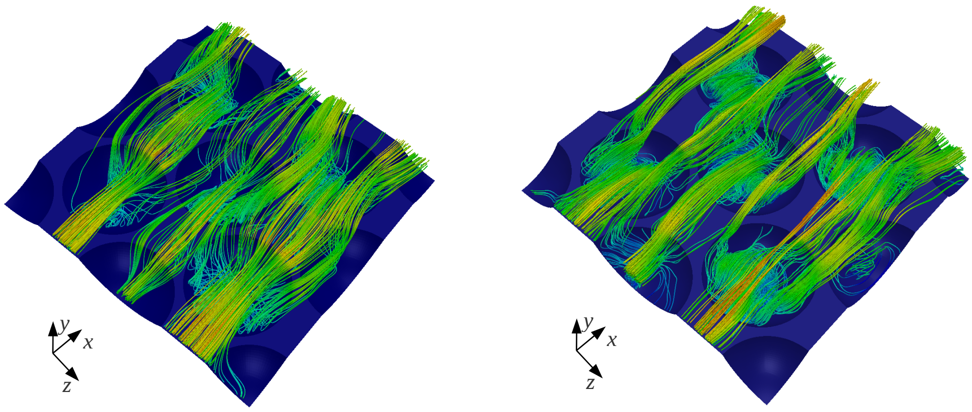

(a) $h/d = 0.196$ (b) $h/d = 0.26$

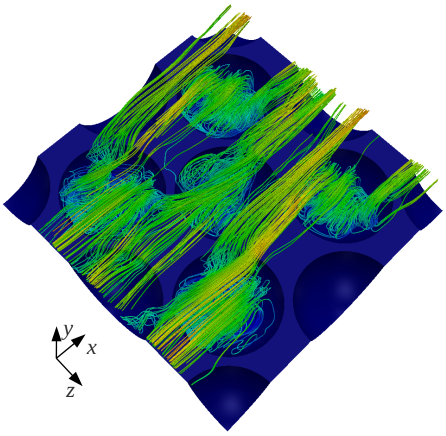

(c) $h/d = 0.326$

Fig. 7.10: Time averaged streamlines for 0.39s realtime inside a dimple package for various dimple depths at $\mathrm{Re}_d = 20000$.

The flow separates at the leading edge and forms a recirculation zone inside each dimple. The extension of reverse flow remains the largest for the deepest dimple at $h/d = 0.326$ which occupies nearly 80% of the whole dimple. From streamlines patterns it is obviously, that one part of the incoming fluid attaches the downstream side and leaves the dimple directly at the trailing edge generating vortex shedding. The other part enters the dimple, rotates and is finally ejected at the spanwise edges of the dimple into the main channel flow. Although the flow is dominated by small scale vortices it has to be mentioned that the fluid ejected from the dimple does not enter the dimple downstream. The streamlines indicate that the heated fluid is moving above the next dimple and becomes well mixed with the main channel flow.

Hence, when the domain size is assumed to be too small including only one half of the dimple, this phenomena will not be pictured in the streamlines and will lead to a significant difference of integral values (e.g. heat transfer) for different domain sizes. Further analysis shows the mix of instantaneous symmetric and asymmetric structures. For instance, the streamline patterns for deep dimples (see Fig. 7.10 c) indicate the presence of an asymmetric vortex structure in the lower row whereas at the top row a symmetric vortex structure is present. Thus, one can conclude that the flow topology is steadily changed in time with no stable vortex structure. The result is contradictory to the single dimple where two stable asymmetric vortex positions could be observed.
Further the results obtained from LES contradict to URANS ones proposed by Isaev [38]. The streamline patterns determined from performed URANS calculations for dimples with a depth of $h/d = 0.326$ showed a steady asymmetrical distribution. In contrast, the time averaged streamlines remain still symmetric in case of LES. The same conclusions have been found in case of a single spherical dimple. Streamlines patterns from LES and self conducted RANS simulations are presented in Fig. 7.11.

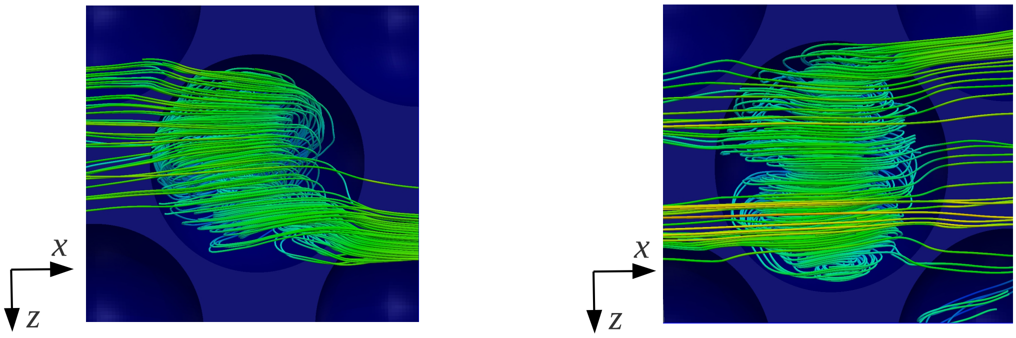

(a) RANS

(b) LES

Fig. 7.11: Comparison of time average streamlines from RANS and LES calculations for turbulent flow over a dimple package at $\mathrm{Re}_d = 20000$.

Hence, in case of using RANS for numerical simulation of turbulent flow over a dimple package, the results will be questionable since the predicted asymmetric flow structures cannot be found within LES computations and experiments. To underline this observation, the velocity profiles in spanwise direction obtained from LES and experiments located at $y/H = 0.9$ close above the dividing surface are presented in Fig. 7.12. If any steady asymmetric structures exists as predicted from RANS calculations, the velocity profiles obtained from LES and experiments should be also asymmetric.

However, the averaged velocity profiles from LDA measurements are symmetric

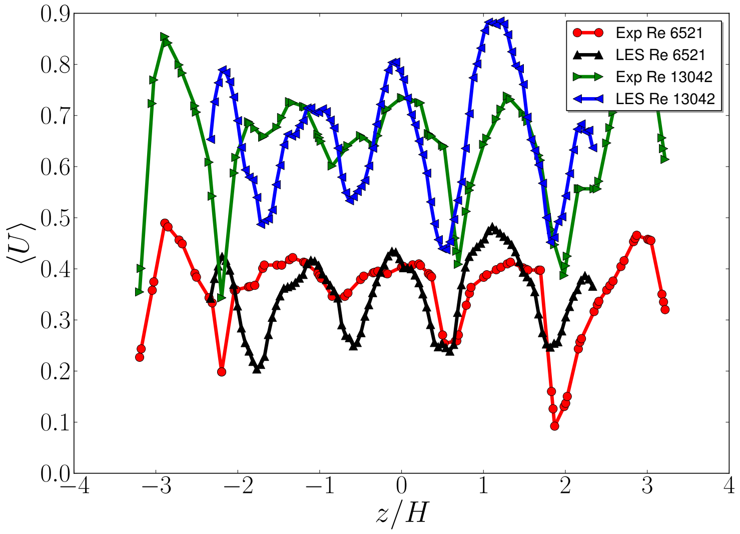

Fig. 7.12: Comparison of time averaged velocity profiles from LES and LDA measurements in spanwise direction at $h/d = 0.26$ for Reynolds numbers $\mathrm{Re}_d = 10000$ and $\mathrm{Re}_d = 20000$.

which is an additional weighty argument that no stable asymmetric structures exist inside the dimples arranged in a staggered array.

LES computations show that vortices arise primarily due to the shear layer shedding from the leading edge of the dimple. In contrast to a single spherical dimple, the evolution of the shear layer structures is strongly influenced by the vortices coming from the dimples located upstream. Hence, a clear visualization of the shear layer structures becomes difficult due to the high magnitude of perturbations inside the dimple. Pressure isosurfaces are used for visualization of the shear layer structures for a single dimple and a dimple package presented in Fig. 7.13.

The high level of perturbations caused by the dimples upstream can be seen on the right side of Fig. 7.13. Only small pressure cores of the shear layer can be observed whereas the shear layer structures can be clearly identified for the single spherical dimple presented in the left side in Fig. 7.13.

To conclude, no stable stationary symmetric or asymmetric vortex structure could be found for turbulent flow over dimple packages. The symmetric primary vortex pair in the center of the dimple and two secondary vortex pairs at each side proposed by Ligrani [60] at $\mathrm{Re}_H = 1250$ for dimples with a ration $h/d = 0.2$ cannot be seen for the turbulent flow regime. The flow remains highly turbulent where the dimples induce fluctuations with a high magnitude causing a high level of mixing inside the channel.

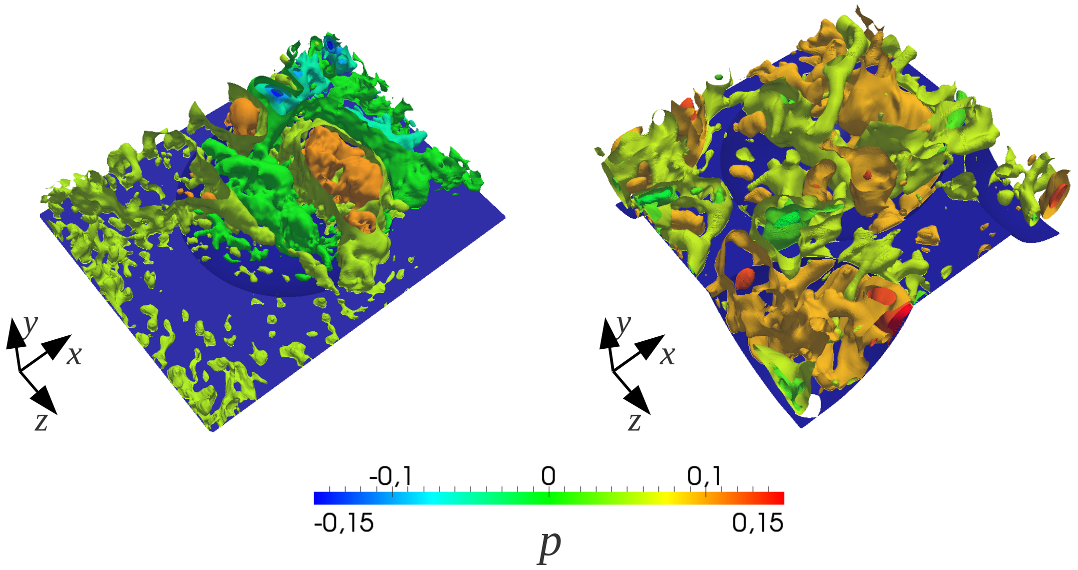

Fig. 7.13: Comparison of shear layer structures for turbulent flow over a single dimple (left) and a dimple package (right) for a ratio $h/d = 0.26$ at $\mathrm{Re}_d = 20000$.

7.4 POD analysis

Since the flow over a dimple package is highly turbulent without any stable symmetric or asymmetric vortex structures, the POD method is applied to find a certain order inside the velocity and pressure field. The POD analysis has been carried out for all investigated dimple configurations in the whole computational domain for the decomposition of the velocity and pressure field. Due to the high number of snapshots and large grid sizes, the performed eigenvalue calculations the computational resources and especially the hard disk storage systems are taken to their limits. But unfortunately, no characteristic structures could be found in the POD modes with variation of dimple depth, Reynolds number and number of snapshots. Therefore, only the results for the dimple standard case with a ratio $h/d = 0.26$ at a Reynolds number $\mathrm{Re}_d = 20000$ will be presented.

Eigenvalues

Since the number of snapshots necessary to capture all relevant flow physics is not known a priori, it has been varied in this work. Finally over 3500 snapshots with a interval of $\Delta t = 0.001s$ are used For dimple packages. The energy decay of the first 250 eigenmodes for the pressure and velocity field are presented in Fig. 7.14.

A rapid decay of the eigenvalues could not be observed for the pressure and velocity as it is in the case for a single spherical dimple (see Fig. 6.32). However, it is

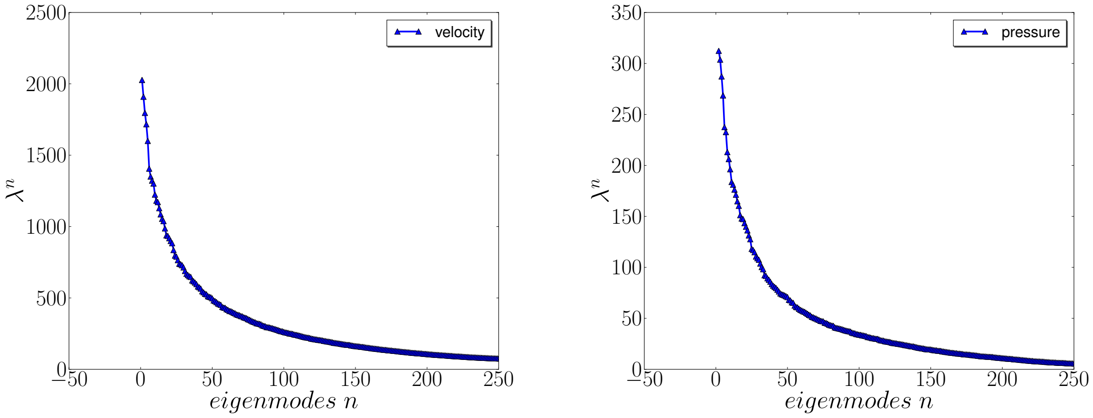

(a) (b)

Fig. 7.14: Energy distribution for the eigenmodes of pressure and velocity.

important for the application of the POD method that the first modes contain the most energy to represent significant flow features. The first modes capture nearly the same amount of energy for the present case which leads already to the conclusion, that the flow is highly turbulent and unordered. It underlines furthermore the previous results in the forgoing section.

Eigenmodes

The streamline patterns and iso-surfaces of the first two eigenmodes for the velocity and pressure field are presented in Fig. 7.15.

The first two eigenmodes of the velocity $\Phi_u^{(1)}$ and $\Phi_u^{(2)}$ reveal a large rotating structures taking its origin inside the cavities and penetrating into the main channel flow. Topologically this structure is very similar to the tornado-like structure proposed by Kiknadze [48] from intuitive considerations. The first eigenmodes involve the fluid motion out of the dimple which is preferable in terms of heat transfer. Furthermore, the mode axis is aligned with the main flow direction which can be seen as an additional explanation of the low pressure losses inside the channel. Nevertheless, it has to mentioned that the physical interpretation of the structures remains unclear since the energy decay of the first modes is fairly low. Especially for the pressure eigenmodes, the distribution of the structures is chaotic with no preferential order. Moreover, the time coefficients of the first modes show no dominant frequencies or any periodic behaviour. Hence one can conclude, that the POD analysis for turbulent flow above a dimple package underlines its chaotic behaviour with no coherent symmetric or asymmetric vortex structures.

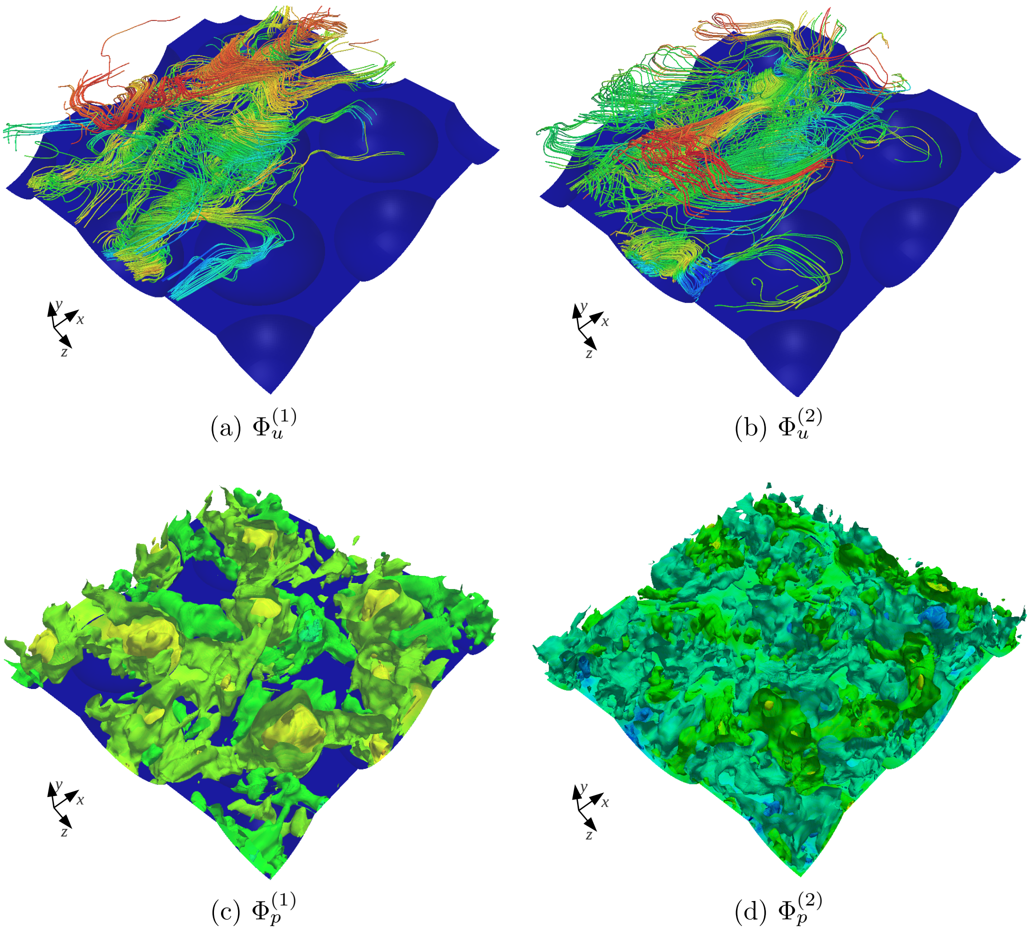
(a) $\Phi_u^{(1)}$ (b) $\Phi_u^{(2)}$

(c) $\Phi_p^{(1)}$ (d) $\Phi_p^{(2)}$

Fig. 7.15: Streamlines of the spatial eigenmodes for the velocity of turbulent flow over a dimpled package at $\mathrm{Re}_d = 40000$.

7.5 Heat transfer and pressure loss

Heat transfer and pressure loss coefficients are determined using LES and experimental methods. In the experimental setup about twelfth pressure sensors have been placed at the channel surface aligned in flow direction. Since the flow is periodic, the overall pressure resistance can be calculated by a regression line including all pressure sensors located in the fully developed range of the flow. Within the LES the overall losses (henceforth named as C_p are calculated on the fly necessary to determine the driving force to provide a constant mass flow rate inside the computational domain.

Table 7.6 illustrates the influence of the relative dimple depth and Reynolds number on the resistance coefficient C_p and the overall heat transfer enhancement Nu_m obtained from LES. The coefficient C_p and as well the integral Nusselt number Nu_m are normalized by the corresponding values of a smooth channel denoted with the subscript 0.

Tab. 7.6: Pressure coefficient C_p and integral Nusselt number Nu_m for different dimple depths at $\mathrm{Re}_H = 6521$ and $\mathrm{Re}_H = 13042$.

	h/d	0.196	0.26	0.326
$\mathrm{Re}_d = 10000$	$\mathrm{Nu}_m/\mathrm{Nu}_{m0}$	1.62	1.93	1.46
	C_p/C_{p0}	2.4	2.89	3.41
$\mathrm{Re}_d = 20000$	$\mathrm{Nu}_m/\mathrm{Nu}_{m0}$	1.75	2.01	1.52
	C_p/C_{p0}	2.83	3.03	3.81

The heat transfer rates are compared to measurements of Ligrani et al. [60] to determine the reliability of the obtained results. The integral Nusselt number $\mathrm{Nu}/\mathrm{Nu}_0 = 1.93$ at $\mathrm{Re}_H = 13042$ for dimples with a ratio $h/d = 0.26$ from LES agrees well with the value of $\mathrm{Nu}/\mathrm{Nu}_0 = 1.83$ proposed by Ligrani et al. [60] for a Reynolds number $\mathrm{Re}_H = 10200$ and a ratio $h/d = 0.22$. Measurements of the flow resistance have only been performed for dimples with a ratio $h/d = 0.26$ due to high mechanical effort to build up the test section for the dimple package including 165 dimples. Measurements showed discrepancies to LES for the resistance coefficient C_p. In reference to the flat channel it is experimentally determined as $C_p/C_{p0} = 3.49$ for a Reynolds number $\mathrm{Re}_H = 6521$ and $C_p/C_{p0} = 3.69$ at $\mathrm{Re}_H = 13042$ which are higher than $C_p/C_{p0} = 2.89$ at $\mathrm{Re}_H = 6521$ and $C_p/C_{p0} = 3.03$ at $\mathrm{Re}_H = 13042$ obtained from LES. While the results obtained from actual measurements and numerical simulation are in the same range, the results are more than twice as high as the results of $C_p/C_{p0} \approx 1.5$ at a Reynolds number $\mathrm{Re}_H = 10200$ and a ratio $h/d = 0.22$ reported by Ligrani [60]. The good agreement of the heat transfer rates and the large discrepancies for the pressure loss are contradictory. It has to be mentioned, that the performed simulations for the turbulent channel flow showed excellent agreement with empiric correlations for the pressure resistance and as well for the heat transfer rates. In addition, the results of the performed measurements and numerical simulations are in the same range. Moreover, it is interesting note that the same discrepancies with the measurements from Ligrani [60] have been found by Elyyan et al. [18].

The obtained results show that the pressure resistance is approximately three times higher for dimples with a ratio $h/d = 0.26$ than that for a smooth channel at Reynolds number $\mathrm{Re}_d = 20000$. The smallest resistance coefficient $C_p/C_{p0} = 2.83$ is documented for the most shallow dimple at $h/d = 0.196$. When h/d increases, the resistance grows attaining the maximum value of $C_p/C_{p0} = 3.81$ at $h/d = 0.326$. The same tendency is determined for the lower Reynolds number $\mathrm{Re}_d = 10000$.

Fig. 7.16 presents the time averaged Nusselt number Nu at the dimple surface for all investigated dimple depths.

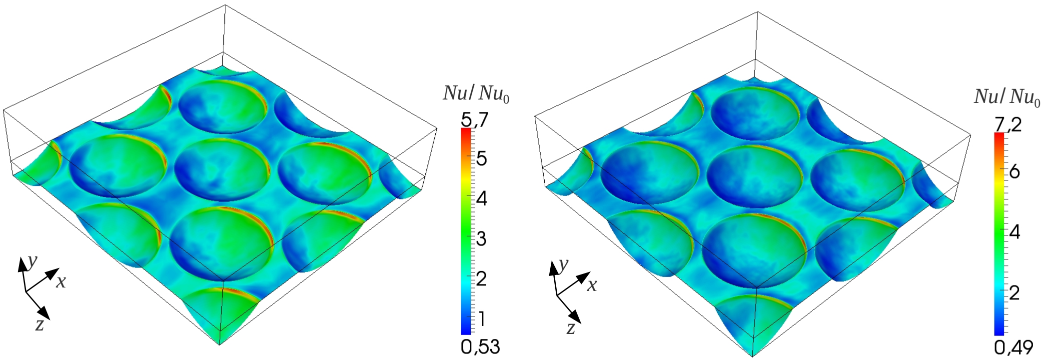

(a) $h/d = 0.196$ (b) $h/d = 0.26$

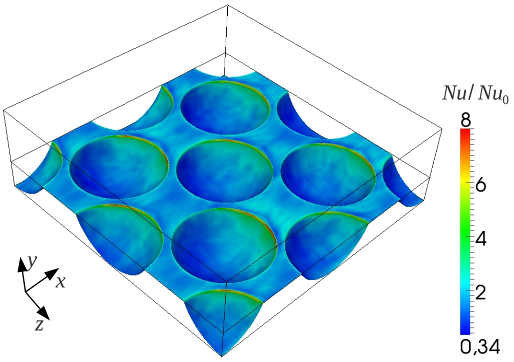

(c) $h/d = 0.326$

Fig. 7.16: Time averaged Nusselt number distribution on dimple packages for various dimple depths at $\mathrm{Re}_d = 20000$.

The highest heat transfer rates can be found at the downstream side of the dimple where the cold flow attaches the dimple surface. It can be up to eight times higher than compared to a smooth channel for the deep dimples. Nevertheless, the velocity is substantially decreased by increasing the dimple depth inside the recirculation zone which reduces the heat flux inside the dimples. The enlargement of the recirculation zone in respect to the dimple depth can be found in the Nusselt number distribution at the dimple wall. While for the flat dimple only a small area shows lower heat transfer rates at the upstream side, the area is significantly enlarged by an increasing dimple depth. Hence, the lowest Nusselt number drops down from $\mathrm{Nu}/\mathrm{Nu}_0 = 0.53$ to $\mathrm{Nu}/\mathrm{Nu}_0 = 0.37$ compared to a smooth channel.

The surface integrated Nusselt number Nu_m obtained from LES presents an overall increase of the heat flux at its maximum of $\mathrm{Nu}_m/\mathrm{Nu}_{m0} = 2.01$ for the standard dimple case ($h/d = 0.26$). Thus, the overall heat transfer enhancement can reach about 201% using an appropriate dimple packages. Two reasons for the high heat transfer rates can be found from numerical analysis. First, the hot fluid is driven out of the dimple in transversal direction leaving the dimple on one or both dimple sides depending on the instantaneous flow topology (symmetric or asymmetric) presented in Fig. 7.10. Surprisingly, the outcoming hot fluid of the dimple is not entering the following dimple as it might be expected, but due to its angle of outflow it moves directly into the main channel flow enhancing the mixing process. Therefore, the incoming fluid in each dimple is well mixed which is preferable in terms for heat transfer enhancement. Second, an additional enhancement of heat transfer is found due to the high magnitude of shear layer fluctuations and large perturbations coming from the upstream dimples.

The criterion proposed by Gee and Webb [26] has been used to determine the overall heat exchanger efficiency. The thermo-hydraulic performance $\mathrm{Nu}/\mathrm{Nu}_0/(C_p/C_{p0})^{1/3}$ shows the best results for dimples with a depth to diameter ratio of $h/d = 0.26$ which is in accordance with the expected one from literature survey (see Ligrani et al. [60]). The reason for the high efficiency can be found within in the numerical simulations. LES calculations showed that the vortices generated the shear layer between the recirculating flow and main channel flow play an important role on the heat transfer enhancement. It was observed that the vortices arising within the shear layer in a dimple with a ratio of $h/d = 0.26$ are stronger than compared to the flat dimple at $h/d = 0.196$. Therefore, both the pressure loss and the heat flux is increased (see Table 7.6). However, a further increase of the depth from $h/d = 0.26$ to $h/d = 0.326$ is followed by a heat transfer reduction. The reason for this phenomena can be explained by the spatial expansion of the vortices in the shear layer when the dimple depth exceeds a certain threshold. The induced fluctuations near the wall, which are responsible for the heat transfer, depend both on the vortex intensity and on the ratio of the vortex scale to the dimple depth, i.e. on the distance between the dimple bottom and the vortex center within the shear layer. In the case of $h/d = 0.26$ this ratio is sufficiently larger than in the case of $h/d = 0.195$ whereas the vortex intensities are nearly comparable. In deep dimples the recirculation zone is more stable. The vortices inside the shear layer are not strong enough to perturbate and interrupt the recirculation zone. Therefore, the hot fluid stays longer within the recirculation zone weakening the heat transfer down to $\mathrm{Nu}_/\mathrm{Nu}_{m0} = 1.51$. As a result, both the ratio $\mathrm{Nu}/\mathrm{Nu}_0$ and the thermo-hydraulic performance have a

maximum for dimples with a depth to diameter ratio of $h/d = 0.26$.
To conclude, the optimal dimple should have a restricted depth to diameter ratio h/d. From one side, it can not be too small, because the creating vortices in the shear layer are not strong enough to enhance the mixing processes. From the other side, it can not be too large. The heat exchange is getting worse when h/d exceeds a certain threshold, since the shear layer vortices are not able to provide efficient mixing in a large relatively stable recirculation zone.

7.6 Summary

Experimental and numerical investigations have been performed for turbulent flow over spherical dimples in a staggered arrangement inside a narrow channel. It was shown that large coherent vortex structures are hard to detect. The flow is chaotic and consists of eddies with a broad range of scales. Snapshots of streamlines show some kind of cell pattern corresponding to dimple arrangement. The instantaneous flow within each dimple can have both, symmetric and asymmetric forms for an increasing dimple depth starting from a ratio of $h/d = 0.26$ where the formation is changed in time revealing no stable configuration. Ejection of the heated fluid into the main channel flow occurs at the spanwise edges which is in accordance with visual observations of Ligrani [60]. The reason of the discrepancy between the flow topologies for a single dimple and dimpled package remains due to the high level of perturbations coming into each dimple from dimples located upstream preventing the creation and evolution of large scale coherent structures. For both Reynolds numbers it was found, that the dimple package with the depth h to diameter d ratio of $h/d = 0.26$ provides the highest thermo-hydraulic performance. At h/d smaller than 0.26 the vortices arising in the cavity are not strong enough to mix the hot and cold fluid effectively which results in a weak heat transfer enhancement. When h/d is larger than 0.26 a relatively stable recirculation zone arises in the dimple. The vortices of the shear layer are not able to destroy the recirculation zone and the hot fluid is kept longer in this zone weakening the heat flux. The POD method is applied to resolved LES fields to identify spatial-temporal structures hidden in the random fluctuations of pressure and velocity fields. The first eigenmodes look similar to tornado-like structures proposed by Kiknadze [48] from intuitive considerations. This structure with a strong inner rotation is aligned with main flow direction keeping the pressure increase at a low level. Nevertheless, the energy decay within the first eigenmodes is fairly small. Hence, a clear physical interpretation and identification of large scale coherent structures becomes difficult.

8 Optimization of heat transfer surfaces

8.1 Introduction

The experimental and numerical results of vortex structures and heat transfer rates for a single spherical dimple and a staggered arrangement of dimples have been presented in the foregoing chapters. The highest thermo-hydraulic efficiency was determined by variation of the dimple depth for dimples with a constant depth to diameter ratio of $h/d = 0.26$ arranged in a dimple package for both Reynolds number $\mathrm{Re}_d = 10000$ and $\mathrm{Re}_d = 20000$. Nevertheless, it is believed that the efficiency of the heat exchanger is not at its optimum.

The designers normally refer to well tested geometries like dimples, ribs or fins to improve the heat exchanger performance. The choice of geometric parameters like dimple diameter, dimple depth, smoothing radius, channel height, etc. is fairly difficult due to its large variety of combination. The parameters are commonly changed by a trial and error procedure using experiments and numerical methods to determine the heat flux and hydraulic losses for the constructed prototypes. However, the designer doesn't even know at the end whether the chosen dimple parameters are at its optimum.

A multi-objective optimization method based on genetic algorithms was implemented into the framework OpenFOAM to overcome the disadvantages of the trial and error method to find an optimal shape of the heat transfer surfaces. The choice of evolutionary algorithms was preferably done, because gradient-based methods are known for its tendency to fall into a local optimum and its numerical instabilities. Moreover, the genetic algorithms are able to optimize multi-objective problems in analogy to evolution theory and are meanwhile well-known and well tested. Thevenin et al. [90] give a detailed overview of the actual optimization methods starting from gradient-based methods up to genetic algorithms and adjoint methods and its application to various technical problems.

Therefore, the main goal in this work is not focused on the development of a new optimization method, but its application and further improvement to determine the optimal heat exchanger surface automatically. Since the mesh generation and computation time is still the main problem for optimization processes using CFD, the focus is placed on these topics within this work.

8.2 Problem formulation and genetic algorithm

The basic idea of genetic algorithms is based on Darwin's law of evolution. The strongest individuals will survive and reproduce enhanced individuals whereas the weak ones are selected out of the reproduction process.

In terms of optimizing heat transfer surfaces, a generation is defined as a set of individuals whereas each individual represents a different shape of the heated surface. The individual is defined by its genes called optimization parameters b_i. The evolution along one generation to the next generation is performed by the evaluation of the strength of each individual (in nature: the best genes) which is defined as fitness parameter or commonly called cost function F. The formulation of the cost function F in case of a heat exchanger leads to the thermo-hydraulic efficiency where the Nusselt number Nu and pressure resistance C_p are object functions in dependence of the optimization parameters b_i.
Hence, the fitness of each individual is characterized in terms of heat transfer and pressure resistance which can be formally written as

$$F_i = F(Nu, C_p)_i = \left(\frac{C_p/C_{p0}}{\mathrm{Nu}/\mathrm{Nu}_0} \right)_i . \tag{8.1}$$

The subscript 0 denotes the values of a smooth channel and remains constant as reference value. The goal of the genetic algorithm is to find an optimal set of the design parameters b_i to minimize the cost function F.

In general, the genetic algorithms show a high potential to explore the whole space of possibilities and avoid the stagnation in a local optimum. Its good robustness is based on the fact, that no derivatives of the object functions are necessary to evaluate the actual cost function (Thevenin et al. [90]). Ten years ago, the genetic algorithms were not preferred in combination with CFD since its high requirements of computational resources. However, at time the computational power has grown massively which allows the application of large optimization processes using numerical simulations performed in parallel on multiple processors.

8.3 Numerical methods

The object functions in terms of Nusselt number Nu and pressure loss C_p have to be calculated in dependence on the optimization parameters b_i. In the present work, the optimization parameters b_i are defined as the normal displacement of selected nodes from the boundary mesh of the heat exchanger surface. The computational domain including the area of optimization is presented in Fig. 8.1.

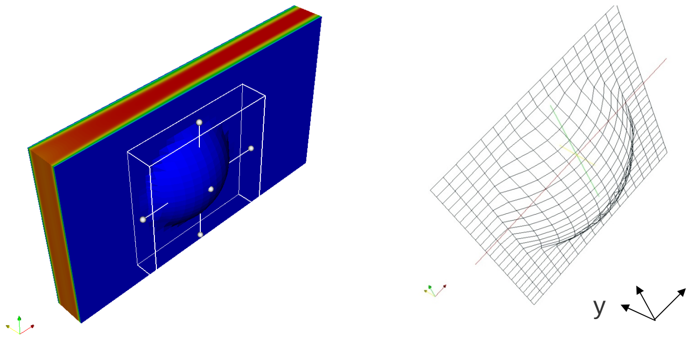

Fig. 8.1: Computational domain and selected nodes within the white box for the optimization

As mentioned above, there are existing several geometric parameters like channel height etc. which can be included in the optimization process. For this study the channel height and overall domain size is kept constant while only the nodes of the boundary mesh within the white box can be mutated according to the actual configuration. Therefore, it has to be highlighted that only the selected area can be transformed whereas the rest of the domain is bounded. The edges of the white box and the channel are assumed to be constant to satisfy the initial conditions and to avoid large scale deformations.

The optimization process requires the following steps according to Thevenin et al. [90].

- generation of the mutated surface of the heat exchanger for each individual
- adequate and fast mesh generation of each individual
- numerical simulation of the flow and temperature field
- determination of object functions and evaluation of the performance of each individuals

The grid generation, solution of transport equations and post-processing is done within the framework OpenFOAM. As mentioned previously, the node normal displacement of each node is chosen as design parameters for the optimization process. The randomly distribution of the node displacements for each individual was done using a gaussian PDF with a restricted magnitude of displacement. Hence, the surface can adopt an arbitrary shape and is not limited by any kind of interpolation functions like B-splines as it is the case of most optimization codes. Spline approximation will lead to smooth surfaces whereas the randomly chosen displacement of each node will result into a surface roughness. To avoid an artificial roughness, a smoothing function is implemented which determines the displacement of each node by an average of the surrounding nodes presented in Fig. 8.2

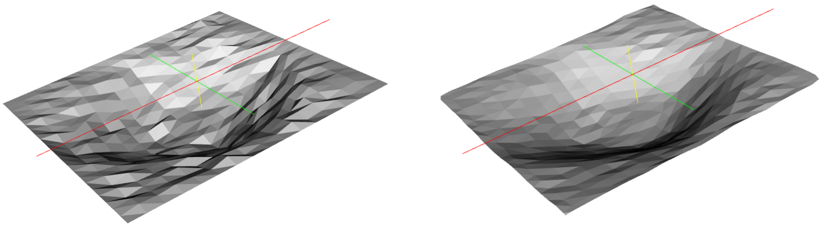

Fig. 8.2: Distorted surface (left) with application of the smoothing function (right).

One may notice that the design parameters of the optimizing surface depend directly on the mesh resolution. The more nodes are included for the optimization the more details of surface can be pictured. Detailed investigations of the different mesh resolutions and the differences between spline approximation and direct nodes displacement have been performed by Klunker [52].

The mesh generation of each individual is one of the time-consuming parts and is often the bottleneck. Commonly automatic meshing tools like IcemCFD are applied to overcome this problem. Nevertheless, the auto meshing tools often require additional work for the different designs to generate high quality meshes including prism layers at the wall which is especially important for heat transfer problems. Hence, the very comfortable method of mesh motion technique in combination with a mesh diffusion equation for grid generation of each individual is established. Therefore, the starting mesh is taken from a smooth channel and is stretched onto the mutated surface whereas the internal mesh is deformed by a generic diffusion equation. As result, the meshing can be performed fully automatically where the computation time reduces significantly and the mesh quality is excellent. Moreover, block-structured grids can be used to reduce the number of grid points in comparison to automatic meshing tools which mainly use tetrahedral grids to represent the whole geometry.

Since more than 1000 computations have to be performed, the LES method is not suitable due to its high computational effort and computation time. Therefore, the RANS method is used within the optimization process. To keep the computation time at a low level, the simulations are not started with an uniform velocity and temperature field, but with fields from the previous or similar generation. Therefore, the converged fields of the velocity, pressure and temperature are interpolated onto the grid of the actual individual. Thus, only a few iteration steps are necessary to obtain a converged numerical solution for the new individual. In addition, the optimization method is fully parallelized where each simulation is carried out on up to 64 processors.

The integral heat flux in terms of Nusselt number Nu_m and flow resistance C_p are determined for each individual to calculate the cost function F. The Nusselt number Nu_m and resistance coefficient C_p are equally weighted in this work. For example if the heat transfer is more important than the pressure loss, the weighting can be changed to drive the optimization method into certain directions. The flow chart in Fig. 8.3 presents the main steps of the optimization method.

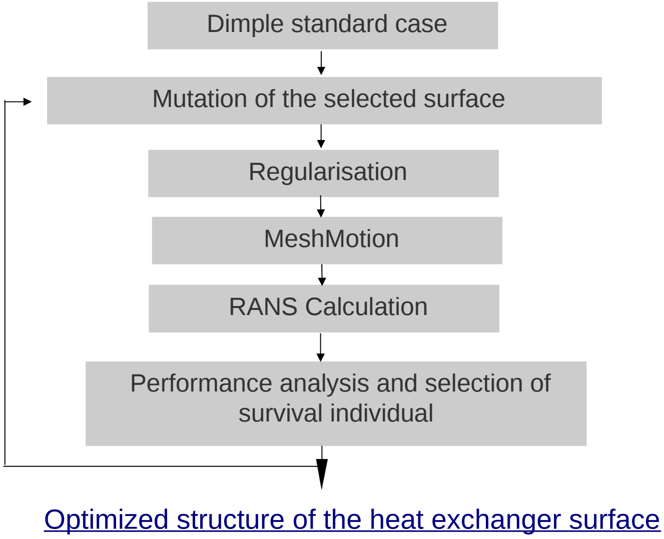

Fig. 8.3: Flow chart of the optimization process.

Since OpenFOAM is operating on bash commands, the combination of the different optimization steps becomes fairly easy. Moreover, the program has been translated into python language for comfortable usage (Klunker [52]).

8.4 Results

The single spherical dimple with a print diameter of $d = 46mm$, a depth of $h = 12mm$ and a channel height of $H = 15mm$ (see sec. 6.1 for detailed description) has been chosen as starting point for optimization. The presented results are obtained using a mesh with a number of 750'000 grid cells at a Reynolds number $\mathrm{Re}_d = 40000$. The selected area of optimization was quadratic of about $1.5d \times 1.5d$ around the spherical dimple including more than 1000 grid points as optimization parameters b_i. Ten individuals are created within each generation where the strongest survives and builds the starting point for the next generation.

Fig. 8.4 presents the evolution of the cost function F of about 70 generations.

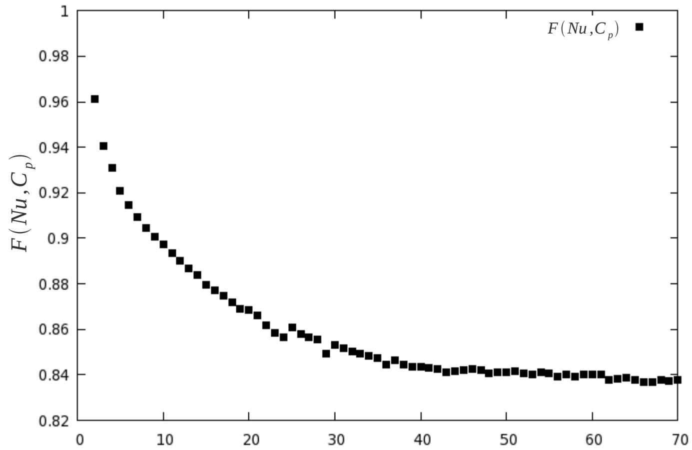

Fig. 8.4: Evolution of the cost function F of the heat exchanger.

With application of the optimization method, the heat exchanger performance could be increased up to 16% compared to the standard spherical dimple. Convergence is approximately reached at the 45^{th} generation. The different shapes during the evolution process of the optimized heat exchanger surface are presented in Fig. 8.5.

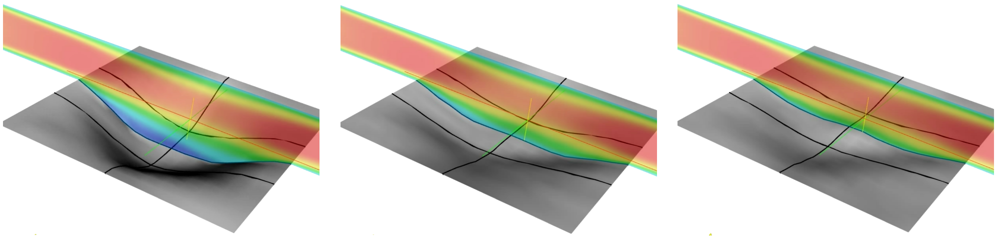
(a) $5^{th} generation$ (b) $25^{th} generation$ (c) $50^{th} generation$

Fig. 8.5: Shape of the optimized heat exchanger surface for different generations.

The depth of the dimple is strongly decreased and the edges of the dimple become smooth within the first iterations. This might be expected because the sharp edges at the downstream side induce a high pressure loss due to flow separation. However, the decrease of the pressure loss leads also to a reduction of the heat transfer rates at the lower surface, but the heat transfer decreases obviously not as much as the pressure drop what results in an increase of the overall performance of the heat exchanger. The appearance of a small hill inside the dimple within the latest generations (see Fig. 8.5 c) is interesting since the formation of a large recirculation zone is prevented which is preferable in respect to pressure loss reduction.
Hence, the dimple-hill structure has been adopted for dimples arranged in a package for further investigations. Therefore, the hill height is varied. The geometrical parameters are presented in Fig. 8.6 and are summarized in Tab. 8.1.

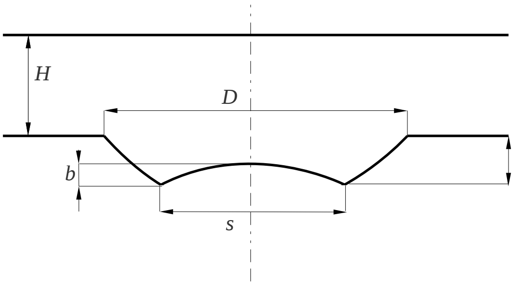

Fig. 8.6: Schematic sketch of the hill shaped dimple form and its geometrical parameters.

Tab. 8.1: Different geometrical parameters of dimple hill shape forms sketched in Fig. 8.6.

	0	1	2	3	4	5	6
s $[mm]$	0	3.8	5.3	5.6	6.25	6.7	6.98
b $[mm]$	0	0.7	1.15	1.6	2.0	2.4	2.85
h $[mm]$	6	6.9	6.4	5.9	5.4	4.9	4.4
d $[mm]$	23						
H $[mm]$	15						

The bounding box of the computational domain, dimple arrangement and boundary conditions are constant for each dimple form which are described in detail in section 7.3.1. Six different hill forms have been considered in this study. The standard dimple shape, denoted with a subscript d, is used as reference of evaluation of the different heat exchangers.

The resistance coefficient C_p and heat transfer rates Nu_m at the heated channel wall are determined to evaluate quantitatively the efficiency of the heat exchanger presented in Fig. 8.7.

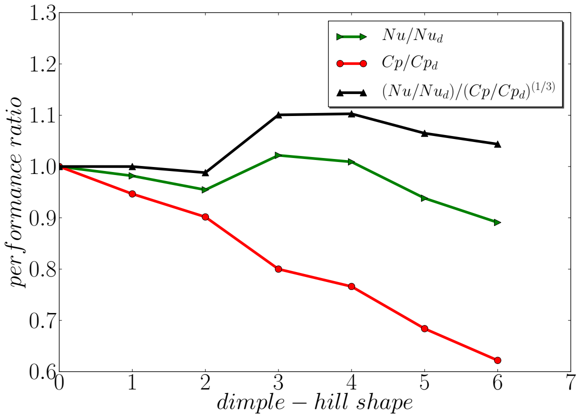

Fig. 8.7: Pressure resistance, heat transfer rates and thermo-hydraulic efficiency for different hill forms inside the dimples.

The resistance decreases nearly linearly up to ratio of $C_p/C_{pd} = 0.615$ by increasing the hill height since the recirculation zone inside the dimple is significantly reduced. In contrast, no drastic enhancement or reduction of heat transfer rates could be observed for the different forms. Moreover, the heat transfer rates remain nearly constant varying from $\mathrm{Nu}/\mathrm{Nu}_d = 1.02$ down to $\mathrm{Nu}/\mathrm{Nu}_d = 0.89$. While for the hill shapes no. one and two a slight decay is visible, the heat transfer rates gets recovered compared to the standard dimple for the hill shapes no. three and four followed again by a decrease for the forms no. five and six. The thermo-hydraulic efficiency shows a maximum value of $(Nu/\mathrm{Nu}_d)/(C_p/C_{pd})^{1/3} = 1.107$ for the hill shape no. four. In other words, the heat transfer could be increased up to 2.1% and the pressure resistance decreased down to 21.4% by using an optimal dimple-hill shape. Fig. 8.8 presents the structure of the modified heat transfer surface, the time averaged streamlines and the mean velocity obtained from LES calculations of the optimal dimple-hill shape.

The simulations of turbulent flow over the standard dimple package showed a widely extended recirculation zone inside each dimple as it is presented in the previous chapter. However, the recirculation zone shrinks significantly with forming a hill inside the dimple which leads to a strong reduction of the pressure resistance. The influence of the hill on the flow field is clearly visible in the axial velocity field presented in Fig. 8.8 c. The recirculating flow is split up into two zones in spanwise direction leading to a symmetric distribution of the flow field whereas the fluid is

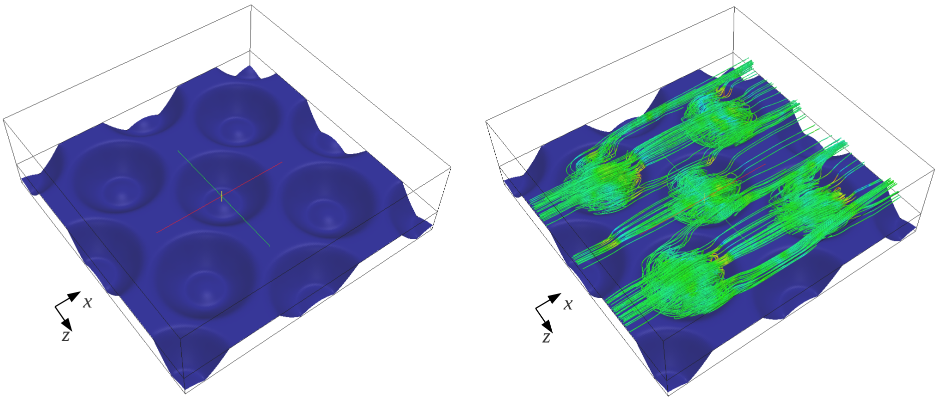

(a) *dimple – hill shape* (b) *Streamlines*

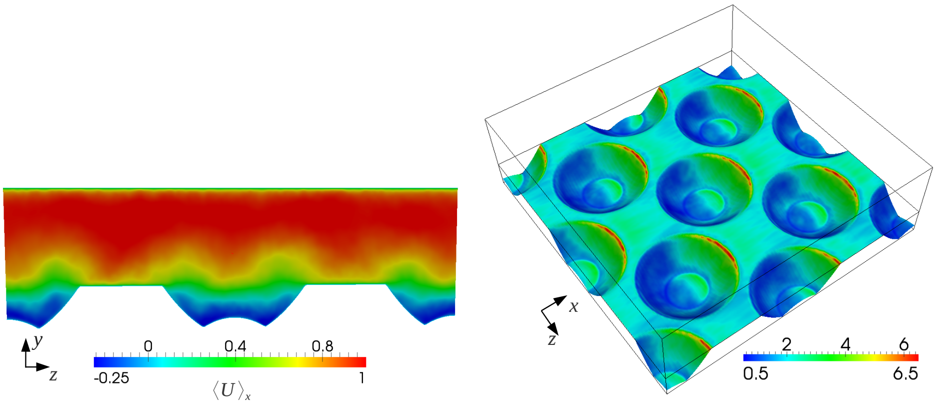

(c) *Reverse flow* (d) $\mathrm{Nu}/\mathrm{Nu}_0$

Fig. 8.8: Investigations of the dimple-hill shape design

ejected out of the dimple at both sides. In terms of heat transfer it can be seen that the attaching flow at the downstream side of the dimple makes the most contribution to increase the heat flux. But using the dimple-hill shape the heat transfer could be slightly increased since the area of low heat flux inside the dimple can be reduced due to the perturbation of the recirculation zone in comparison to the standard dimple configuration.

8.5 Summary

An optimization method was implemented into the framework OpenFOAM to increase the thermo-hydraulic efficiency of a heat exchanger. The general optimization techniques using CFD are already known and published in literature. However, two major improvements have been established and tested within this work. First of all, a predefined mesh is generated which is stretched onto the actual geometry of each individual using mesh motion technique coupled with a generic diffusion equation in OpenFOAM to overcome the problem of extensive mesh generation. The technique reduces the computation time for the mesh generation significantly and further ensures a high quality of the different grids. As result, the mesh needs not to be build for each individual separately but rather is generated fully automatically. The second main improvement is the choice of the optimization parameters (genes) which are defined as node normal displacements of the selected heat transfer surface. Hence, the geometry of the resulting optimized surface is not restricted to e.g. spline approximations which ensures a free evolution of the surface without any geometric pre-definitions.

Application of the optimization method for a single spherical dimple revealed, that the dimple is flattened compared to the standard dimple. Moreover, a small hill appears inside the dimple enhancing the thermo-hydraulic performance up to 16%. For further investigations, the dimple-hill shape has been adopted for dimples in a staggered arrangement where six different hill shapes have been analyzed in respect to pressure loss and heat transfer rates. The thermo-hydraulic performance shows its maximum with variation of the hill height. The pressure loss is substantially reduced down to 21.4% due to the shrinking of the recirculating zone inside the cavity. Moreover, the heat transfer rates could be slightly improved up to 2.1% which results in an improvement of the thermo-hydraulic efficiency up to 11%. Nevertheless, it has to be mentioned that the dimple-hill shape is not unique. The form of the heated surfaces depends mainly on the flow properties and overall dimensions of the heat exchanger. For example if the Reynolds number is changed, the form of the heated surfaces will be different compared to the investigated case.

9 Conclusion

Numerical and experimental investigations of heat transfer and vortex formations of turbulent flow over a single spherical dimple and dimples arranged in a staggered package have been performed. The different methods of investigation have been verified for a smooth channel using empiric correlations and DNS data published in literature. The comparison of numerical results with experimental data shows that especially the LES method is capable of predicting characteristic flow features of turbulent flow over dimpled surfaces with a satisfactory accuracy.

Time resolved simulations reveal the presence of oscillations with dominating frequencies inside the flow over a single spherical dimple with a depth to diameter ratio $h/d = 0.26$. One can distinguish low-frequency ($f = 0.223\ Hz$) and high-frequency ($f = 2.5\ Hz$ and $f = 10\ Hz$) components at selected points within dividing surface between the dimple and channel. Analysis of flow structures using phase averaged streamline patterns, pressure iso-surfaces, LDA and time resolved pressure measurements show clearly the presence of an asymmetric flow structure which is inclined in respect to the upstream flow direction at an angle of approximately ±45°. Although the instantaneous flow picture is asymmetric, however, the flow averaged over a sufficiently long time period is nearly symmetric. In this context LES results contradict to RANS simulations which predict the asymmetry even in the averaged flow pictures. Since the time averaged fields determined from experimental methods are also symmetric, LES reproduces the flow physics more adequately than RANS.

The implementation and application of the POD method shows the formation of tornado-like spatial structures inside the dimple. The first eigenmode of the velocity field corresponds to a mono structure steadily changing its rotation in time. This structure is responsible for fluctuations and outbursts at the back side of the cavity. The second POD mode corresponds to a twin structure located symmetrically inside the dimple. In addition, the eigenmodes of the pressure field reveal the presence of a strong shear layer arising between the recirculating flow and the main channel flow. It was found that the shear layer fluctuations have major impact on heat transfer enhancement since the fluctuating fluid attaches the downstream side of the dimple inducing high heat transfer rates. Starting from POD analysis the reason of the vortex switching between ±45° is found within the spatial inhomogeneities of the evolving shear layer structures. The fluid is accelerated and decelerated in the shear layer which leads to different spanwise velocities at each side when the fluid attaches the curved dimple surface. Hence, the different spanwise velocities form an asymmetric flow field inside the dimple.

The flow physics inside a single dimple are also studied using dye visualization, LDA and pressure measurements. The dye visualizations show clearly the formation of an asymmetric structure inside the dimple and its switching towards the main channel flow. In addition, LDA measurements are performed to validate the numerical models and to determine characteristic frequencies of the turbulent flow. Frequency analysis of the velocity signal obtained from LDA measurements confirmed the findings from LES. Moreover, only small discrepancies between measurements and numerical data for different cross sections of the velocity profiles could be achieved. Time resolved measurements of the pressure at the dimpled wall are carried out using piezo-resistance electronic sensors with a high temporal resolution. The correlations of the pressure signals confirm additionally the presence of an asymmetric flow structure and its switching inside the dimple found from LES simulations.

The formation of asymmetric flow structures show major advantages in respect to heat transfer since the heated fluid is steadily moving out of the dimple. Hence, it is preferable in comparison to a fully symmetric structure which keeps the fluid inside the dimple reducing the temperature differences between the hot wall and the cold fluid. The integral heat transfer enhancement of $\mathrm{Nu}_m/\mathrm{Nu}_{m0} = 1.142$ compared to a smooth wall was found relatively small if the dimple is placed in an evolving temperature boundary layer. In contrast, if the temperature profile is fully developed, the heat transfer can be increased up to $\mathrm{Nu}_m/\mathrm{Nu}_{m0} = 1.67$. A significant increase of the heat transfer rates due to the long period oscillations could not be found since the time scale of the heat transfer mechanism is much smaller than the switching time of the asymmetric flow structure. Therefore, the switching process shows only advantages to prevent fouling inside the heat exchanger.

Since the single dimple is only an academic case, further study has been carried for spherical dimples in a staggered arrangement inside a narrow channel. LDA and pressure measurements are additionally performed to validate the numerical methods. Vortex structures responsible for the high thermo-hydraulic efficiency for dimples with a ratio $h/d = 0.26$ have been determined using LES method by variation of the dimple depth. Ejection of the hot fluid into the main channel flow at the spanwise edges is in accordance with visual observations published in literature enhancing the mixing process inside the channel with a low induced pressure loss. Deep cavities with a ratio $h/d = 0.326$ reveal the formation of a large recirculation zone inside the dimple keeping the heated fluid inside which results in a strong decrease of the overall performance of the heat exchanger. The optimal dimple ratio $h/d = 0.26$ in respect to the thermo-hydraulic performance has been found with variation of the dimple depth including an integral heat transfer enhancement up to $\mathrm{Nu}_m/\mathrm{Nu}_{m0} = 2.01$ and an overall resistance of $C_p/C_{p0} = 3.03$ for the Reynolds number $\mathrm{Re}_d = 20000$. Obtained spatial structures from POD analysis show a strong rotation in flow direction. However, due to the low energy decrease within the first eigenmodes the physical identification and interpretation of the structures becomes difficult. The results underline the high turbulent state of the current flow field.

To search for the optimal shape of heat transfer surfaces, an optimization method based on genetic algorithms has been implemented into the framework OpenFOAM. The combination of mesh motion methodology allows a fast grid generation for each individual. Further using a mapping procedure to interpolate the converged fields onto the actual mesh of the present individual shows major advantage in respect to convergence performance and computation time. Moreover, the geometry is not restricted to a spline geometry what ensures a free evolution of the selected surface. As a result, a small hill appears inside the dimple enhancing the thermo-hydraulic performance up to 16% during the optimization process. The form has been adopted for dimples arranged in a staggered package which revealed a reduction of the pressure loss of 21.4% due to the shrinking of the recirculating zone inside the cavity. Moreover, the heat transfer rates could be slightly improved up to 2.1% which shows an improvement of the thermo-hydraulic efficiency of about 11%. Nevertheless, it is believed that there are existing other optimal structures allowing to increase heat transfer rates with a low flow resistance. Due to the high number of simulations (> 1000) and the restricted computational resources only a small area within the heat exchanger could be optimized. If the area of optimization will be enlarged, other structures like wavy surfaces might be expected.

The thesis presents only a part of the results which have been obtained within this work. In addition, asymmetric dimple structures have been investigated using experimental methods. Further detailed flow visualizations using dye injection method are conducted for a single dimple for different Reynolds numbers starting from the laminar towards the turbulent flow. A particle tracking hardware has been build up using blue light LED's in connection with fluorescent particles to determine the path lines inside the cavities. Further many RANS and URANS calculations with variation of grid resolution, turbulence models and boundary conditions have been carried out to analyze the effects of dimple depth, dimple diameter and channel height on heat transfer and pressure loss. Moreover, to improve and generalize the optimization method, an adjoint solver algorithm was implemented into the framework work OpenFOAM. The direct orientation towards the optimal structure of the heat exchangers surface shows major advantage compared to the established optimization method in respect to computation time.

This thesis lights up the complexity of a heat exchanger and gives a deep insight into flow physics and heat transfer in turbulent flows over dimpled surfaces in a narrow channel. With application of the LES method, a detailed analysis could be performed to determine instationary effects inside the dimples and to extract the different vortex structures responsible for the high heat transfer enhancement. The application of an optimization method showed, that the investigated dimple geometry is not its optimum and that there are existing modified structures to improve the heat exchanger performance.

Bibliography

[1] Afanasyev V.N., Chudnovsky Y.P.; Leontiev A.I.; Roganov P.S.: *Turbulent flow friction and heat transfer characteristics of spherical cavities on a flat plate.* Experimental Thermal and Fluid Science, (7):1–8, 1993.

[2] Aubry N., Holmes P.; Lumley J.L.; Stone E.: *The dynamics of coherent structures in the wall region of a turbulent boundary layer.* J. of Fluid Mechanics, 192:115–173, 1988.

[3] Aubry N., Guyonnet R., Lima R.: *Spatiotemporal analysis of complex signals: theory and applications.* J. of Statistical Physics, 64(3-4):683–739, 1991.

[4] Baehr H. D., Stephan K.: *Wärme und Stoffübertragung.* Springer, 2006.

[5] Balares E., Piomelli U., Wallace J.M.: *Self-similar states in turbulent mixing layers.* J. of Fluid Mechanics, 2001.

[6] Bardina J., Ferziger J.H, Reynolds W.C: *Improved subgrid models for large eddy simulation.* AIAA, page 801357, 1980.

[7] Bejan, A.: *General criterion for rating heat exchanger performance.* Int. J. of Heat and Mass Transfer, 21:655–658, 1978.

[8] Bejan, A.: *Entropy generation through heat and fluid flow.* Wiley, New York, 1982.

[9] Berkooz, G.: *Observation on the proper orthogonal decomposition.* Studies in Turbulence, Springer:229–247, 1991.

[10] Berkooz G., Holmes P., Lumley J.: *The proper orthogonal decomposition in the analysis of turbulent flows.* Annu. Rev.Fluid Mechanics, 25:539575, 1993.

[11] Burgess N.K., Ligrani P.M.: *Effects of dimple depth and on Nusselt numbers and friction factors for internal cooling channel.* Proceedings of ASME Turbo Expo, No. GT2004-54232, 2004.

[12] Chang K., Constantinesci G., Park S.O.: *Analysis of the flow and mass transfer processes for the incompressible flow past an open cavity with a laminar and a fully turbulent incoming boundary layer.* J. of Fluid Mechanics, 561:113–146, 2006.

[13] Chatterjee: *An introduction to the proper orthogonal decomposition.* Current Science, 78(7):808–817, 2000.

[14] Chosal S., Lund T.S; Moin P.; Akselvoll K.: *A dynamic localization model for large-eddy simulation of turbulent flows.* J. of Fluid Mechanics, 286:229–255, 1995.

[15] Chyu M.K., Yu Y., Ding H.; Downs J.P.; Soechting F.O.: *Concavity enhanced heat transfer in an internal cooling passage.* ASME, No. 97-GT-437, 1997.

[16] Davis, J.M.: *The aerodynamics of golf balls.* J. of Applied Physics, 20:821–828, 1949.

[17] Ekkad S., Nasir H.: *Dimple enhanced heat transfer in high aspect ratio channels.* J. of Enhanced Heat Transfer, 10(4):395–405.

[18] Elyyan M.A., Rozatia A., Tafti D.K.: *Investigation of dimpled fins for heat transfer enhancement in compact heat exchangers.* Int. J. of Heat and Mass Transfer, 51(11-12):2950–2966, 2007.

[19] Farabee T., Casarella M. J.: *Spectral features of wall pressure fluctuations beneath turbulent boundary layers.* Physics of Fluids, 3(10):2410–2420, 1991.

[20] Ferziger J.H., Peric M.: *Numerische Strömungsmechanik.* Springer, 2002.

[21] Fiebig, M.: *Embedded vortices in internal flow: heat transfer and pressure loss enhancement.* Int J. of Heat and Mass Transfer, 15(5):376–388, 1995.

[22] Fiebig, M.: *Vortices and Heat Transfer.* J. of Applied Mathematics and Mechanics, 77(1):3–18, 1997.

[23] Fiedler, H.E.: *Coherent structures in turbulent flows.* Proc. Aerospace Science, 25:231–269, 1988.

[24] Fox, R.: *Computational models for turbulent reacting flows.* Cambridge University Press, 2003.

[25] Frenz, M.: *Auswertung von Druck- und LDA Messungen turbulenter Strmung auf Dellenoberflächen.* Student work, 2011.

[26] Gee D.L., Webb R.L.: *Forced Convection Heat Transfer in Helically Rib-Roughened Tubes.* Int. J. of Heat and Mass Transfer, 23:1127–1136, 1980.

[27] Germano, M.: *Turbulence: The filtering approach.* J. Fluid Mechanics, 238:235–336.

[28] Gersten K., Herwig H.: *Strömungsmechanik.* Vieweg-Verlag, 1992.

[29] Gromov P.R., Zobnin A.B.; Rabinovich M.I.; Suschik M.M.: *Creation of solitary vortices in a flow around shallow spherical depressions.* Sov. Tech. Phys. Letter, 23(547), 1986.

[30] Haller, G.: *An objective definition of a vortex.* J. of Fluid Mechanics, 525:1–26, 2005.

[31] Herwig, H.: *Strömungsmechanik.* Springer, 2. Auflage, 2006.

[32] Herwig H., Kock F.: *Direct and indirect methods of calculating entropy generation rates in turbulent convective heat transfer problems.* Heat and Mass Transfer, 43:207–215, 2007.

[33] Hiwada M., Mabuchi I.; Kumada M.; Kawamura T.: *Some characteristics of flow pattern and heat transfer past a circular cylindrical cavity.* JSME, Bulletin, 26:1744–1752, 1983.

[34] Holmes P., Lumley J., Berkooz G.: *Turbulence, Coherent Structures, Dynamical Systems and Symmetry.* Cambridge University Press, 1998.

[35] Hunt J.C.R., Wray A.A., Moin P.: *Eddies, stream and convergence zones in turbulent flows.* Center for Turbulence Research Report CTR-S88, 1995.

[36] Hussain, F.: *Coherent Structures and turbulence.* J. of Fluid Mechanics, 173:303–356, 1986.

[37] Incropera F. P., DeWitt D. P.: *Fundamentals of Heat and Mass Transfer.* John Wiley and Sons 4th edition, 1996.

[38] Isaev, Prof. Dr.-Ing. S. Personal communications.

[39] Isaev S.A., Kornev N.; Leontiev A.I.; Hassel E.: *Influence of the Reynolds number and the spherical dimple depth on turbulent heat transfer and hydraulic loss in a narrow channel.* Int J. of Heat and Mass Transfer, 53(1-3):178–197, 2010.

[40] Isaev S.A., Leontiev A.I.: *Numerical simulation of vortex enhancement of heat transfer under condititions of turbulent ow past a dpherical dimple on the wall of a narrow channel.* High Temperature, 41(5):665679, 2003.

[41] Isaev S.A., Leontiev A.I.; Mitjakov A.V.; Pyshnyi I.A.: *Intensification of tornado-like heat transfer in asymmetric dimples.* J. of Engineering Physics and Thermophysics, 76:31–34, 2003.

[42] Isaev S.A., Leontiev A.I., Zhdanov V.: *Simulation of tornado-like heat transfer at flow passing a relief with dimples.* Proceedings of the 12th Int. Heat Transfer Conf., pages 735–738, 2002.

[43] Jahnke, S.: *Large Eddy Simulation of turbulent mixing process in a coaxial jetmixer.* University of Rostock, 2007.

[44] Jeong J., Hussain F.: *On the identification of a vortex.* J. of Fluid Mechanics, 285:69–84, 1995.

[45] Jeong J., Hussain F.; Schoppa W.; Kim J.: *Coherent structures near the wall in a turbulent channel flow.* J. of Fluid Mechanics, 332:185–214, 1997.

[46] Karhunen, K.: *Zur Spektraltheorie stochastischer Prozesse.* Annaleas Academiae Scientiarum Fennicae, 34, 1946.

[47] Kawamura H., Abe H., Matsuo Y.: *DNS of turbulent heat transfer in channel flow with respect to Reynolds and Prandtl number effects.* Int. J. of Heat and Fluid Flow, 20:196–207, 1999.

[48] Kiknadze G.I., Krasnov Y.K.: *Evolution of tornado like viscous flows.* Proc. Academy of Sciences USSR - Hydrodynamics, 291:1315–1319, 1986.

[49] Kiknadze G.I., Oleinikov V.G.: *Self-organization of tornado-like vortex structures in gas and liquid ows and heat transfer intensication.* Proc. Inst. Thermophysics Preprint, 227:47ff, 1990.

[50] Kim, J.: *On the structure of pressure fluctuations in simulated turbulent channel flow.* J. of Fluid Mechanics, 205:421–451, 1989.

[51] Kirby M., Boris J.P., Sirovich L.: *A proper orthogonal decomposition of a simulated supersonic shear layer.* Int. J. Numerical Methods Fluids, (10):411–428, 1990.

[52] Klunker, J.: *Dellenoptimierung.* Student work, 2010.

[53] Kock, F.: *Bestimmung der lokalen Entropieproduktion in turbulenten Strömungen und deren Nutzung zur Bewertung konvektiver Transportprozesse.* Shaker Verlag, 2003.

[54] Kornev N., Hassel E.: *Method of random spots for generation of synthetic inhomogeneous turbulent fields with prescribed autocorrelation functions.* Communications in Numerical Methods in Engineering, 23(1):35–43, 2007.

[55] Kornev N., Tkatchenko I., Hassel E.: *A simple clipping procedure for the dynamic mixed model based on taylor series approximation.* Communications Numerical Methods in Engineering, 22(1):55–61, 2006.

[56] Kuethe, A.M: *Boundary layer control of flow separation and heat transfer.* US Patent 3 578 264, 1971.

[57] Lai Y.G, So R.M.C: *Near-wall modeling of turbulent heat fluxes.* Int. J. of Heat and Mass Transfer, 33(7):1429–1440, 1990.

[58] Lewalle J., Delville J., Bonnet J.P.: *Decomposition of Mixing Layer Turbulence into Coherent Structures and Background Fluctuations.* Applied Scientific Research, 64(4):301–328, 2000.

[59] Lienhardt H., Breuer M., Koeksoy C.: *Drag reductions by dimples? - A complementary experiment/numerical investigation.* Int. J. of Heat and Fluid Flow, 29:783–791, 2008.

[60] Ligrani P.M., Oliveira M.M., Blaskovich T.: *Comparison of heat transfer augmentation techniques.* AIAA J., 41(3):337–362, 2003.

[61] Ligrani P.M., Harrison J.L.; Mahmmod G.I.; Hill M.L.: *Flow structure due to dimple depressions on a channel surface.* Phys. Fluids, 13(11):3442–3451, 2001.

[62] Ligrani P.M., Mahmood G.I.; Harrison J.L.; Clayton C.M.; Nelson D.I.: *Flow structure and local Nusselt number variations in a channel with dimples and protrusions on opposite walls.* Int. J. of Heat and Mass Transfer, 45:2011–2020, 2001.

[63] Lilly, D.K.: *A proposed modification of the germano subgrid-scale closure method.* Physics of Fluids, 4:633–635, 1992.

[64] Loeve, M.: *Probability Theory.* Princton NJ, 1955.

[65] Lugt, H.J.: *Vortex flow in nature and technology.* Wiley, 1983.

[66] Lumley, J.: *The structure of inhomogeneous turbulent flows.* Atmospheric turbulence and radio wave propagation, pages 166–178, 1967.

[67] Lumley, J.: *Stochastic Tools in turbulence.* Academic Press New York, 1970.

[68] Lumley, J.: *Coherent structures in turbulence.* Transition and Turbulence Academic Press, pages 215–245, 1981.

[69] Lyons S.L., Hanratty T.J, McLaughlin J.B.: *Direct numerical simulation of passive heat transfer in a turbulent channel flow.* Int. J. of Heat and Mass Transfer, 34(4-5):1149–1161, 1991.

[70] Mahmood G.I., Ligrani P.M.: *Heat transfer in a dimpled channel combined influences of aspect ratio, temperature, Reynolds number, and flow structure.* Int. J. of Heat and Mass Transfer, 45:2011–2020, 2004.

[71] Mahmood G.I., Sabbagh M.Z., Ligrani P.M.: *Heat Transfer in a shannel with dimples and protrusions on opposite walls.* J. of Thermophysics and Heat Transfer, 15(3):275–283, 2001.

[72] Manhart M., Wengle H.: *A spatiotemporal decomposition of a fully inhomogeneous turbulent flow field.* Theoret. Comput. Fluid Dynamics, 5:223–242, 1993.

[73] Meneveau C., Katz J.: *Scale-invariance and turbulence models for large-eddy simulation.* Annu. Rev. Fluid Mechanics, 32:1–32, 2000.

[74] Menter, F.R.: *Two-Equation eddy-viscosity turbulence models for engineering applications.* AIAA Journal, 32(8):1598–1605, 1994.

[75] Menter F.R., Kuntz M., Langtry R.: *Ten years of industrial experience with the SST turbulence model.* Turbulence, Heat and Mass Transfer, pages 625–632, 2003.

[76] Moin P., Moser R.D.: *Characteristic eddy decomposition of turbulence in a channel.* J. of Fluid Mechanics, 200:471–509, 1989.

[77] Moon H.K., O'Connel T., Sharma R.: *Heat transfer enhancement using a convex-patterned surface.* J. of Turbomachinery, 125:274–280, 2003.

[78] Moser R. D., Kim J., Mansour N. N.: *Direct Numerical Simulation of Turbulent Channel Flow up* Re_τ*=590.* Phys. of Fluids, 11(4):943–945, 1999.

[79] Park J., Desam P.R., Ligrani P.M.: *Numerical predicitions of flow structures above a dimpled surface in a channel.* Numerical Heat Transfer, 45:1–20, 2004.

[80] Pope, S.B.: *Turbulent Flows.* Cambridge University Press, 2000.

[81] Presser, K.H.: *Empirische Gleichungen zur Berechnung der Stoff- und Wãrmeubertragung für den Spezialfall der abgerissenen Strömung.* Int. J. of Heat and Mass Transfer, 15(12):2447–2471, 1972.

[82] Roshko, A.: *Structure of turbulent shear flows: A new look.* AIAA Journal, 14(10):1349–1357, 1976.

[83] Schlichting H., Gersten K.: *Boundary Layer Theory.* Springer, 2000.

[84] Schnueckel, C.: *Numerische Simulation mittels RANS/URANS Verfahren turbulenter Strömungen mit Wãrmebergang auf strukturierten Oberflãchen.* Master's Thesis, 2009.

[85] Sirovich, L.: *Turbulence and the dynamics of coherent structures. Part I: coherent structures. Part II: symmetries and transformations. Part III: dynamics and scaling.* Quart. Appl. Math., 45:561–590, 1987.

[86] Snedeker R.S., Donaldson C.P.: *Observation of a bistable flow in a hemispherical cavity.* AIAA J., 4:735–736, 1966.

[87] Tabor G.R., Baba-Ahmadi: *Inlet conditions for large eddy simulation: A review.* Computers and Fluids, 39:553–567, 2010.

[88] Terekhov V.I., Kalinina S.V., Mshvidobadse Y.M.: *Flow structure and heat transfer on a surface with a unit hole depression.* Russian J. of Engineering Thermophysics, 4:11–34, 1995.

[89] Terekhov V.I., Kalinina S.V., Mshvidobadse Y.M.: *Heat transfer coefficient and aerodynamic resistance on a surface with a single dimple.* J. of Enhanced Heat Transfer, 4:131–145, 1997.

[90] Thévenin D., Jániga G.: *Optimization and Computational Fluid Dynamics.* Springer, 2008.

[91] Turnow J., Kornev N.; Isaev S.; Hassel E.: *Large Eddy Simulation of Vortex Formation in a Channel with a Spherical Dimple.* Third OpenFOAM Workshop, Milan, Italy, July 2008.

[92] VDI-Gesellschaft: *VDI Heat Atlas.* Springer, 2003.

[93] Vreman B., Guerts B., Kuerten H.: *On the formulation of the dynamic mixed subgrid-scale model.* Physics Fluids, 6(12):4057–4059, 1994.

[94] Wang Z., Yeo K., Khoo B.C.: *Numerical simulation of laminar channel Flow over dimpled Surface.* 16th AIAA Computational Fluid Dynamics Conference 23-26, AIAA 2003-3964, 2003.

[95] Webb, R.L: *Performance evaluation criteria for use of enhanced heat transfer surfaces in heat exchanger design.* Int. J. of Heat and Mass Transfer, 24(4):715–726, 1981.

[96] Wieghardt, K.: *Erhöhung des turbulenten Reibungswiderstandes durch Oberflächenstoerungen.* Forschungshefte fur Schiffstechnik, 1:65–81, 1953.

[97] Wilcox, D.C: *Turbulence modeling for CFD.* DCW Industries Inc - La Canada - California, 1994.

[98] Williams, D.: *Drag force on a golf ball in flight and its practical significance.* The Quaterly J. of of Mechanis and Applied Mathematics, 12:387–392, 1959.

[99] Wu J-Z., Xiong A.K., Yang Y.T.: *Axial stretching and vortex definition.* Physics of Fluids, 17:038108, 2005.

[100] Wuest, C.: *Dellen im Dach.* Spiegel, 14:170–172, 2004.

[101] Zang Y., Street R.L, Koseff J.R: *A dynamic mixed subgrid-scale model and its application to turbulent recirculating flow.* Physics Fluids, 12:3186–3196, 1993.

A Validation of RANS method

The validation, mesh studies and further determination of sensitivities of the results for RANS method in OpenFOAM using $k - \omega$-SST-Model written for low Reynolds number flow have been performed. Only a brief summary of this work is presented. Geometric dimensions are equally as described in sec. 6.2 for the turbulent plane channel wall. A sufficient mesh resolution was found for the mesh C2 (see Tab. 6.4) with about 1'272'864 grid cells. The velocity at the inlet was set to the 1/7th power law profile with a varying turbulence intensity of $Tu = 1\%$ and $Tu = 5\%$ respectively. In addition, computations have been performed with periodic boundary conditions to evaluate heat transfer rates for fully developed flow. In Fig. A.1 the temperature distribution inside the channel in streamwise direction for the non-periodic and periodic case are presented respectively.

For evaluation of the results the profiles are compared to DNS data from Moser et al. [78] and to correlations of Dean (see eq. 6.2) for the friction coefficient C_f and the Chilton and Colburn correlation for the Nusselt number distribution in streamwise direction.

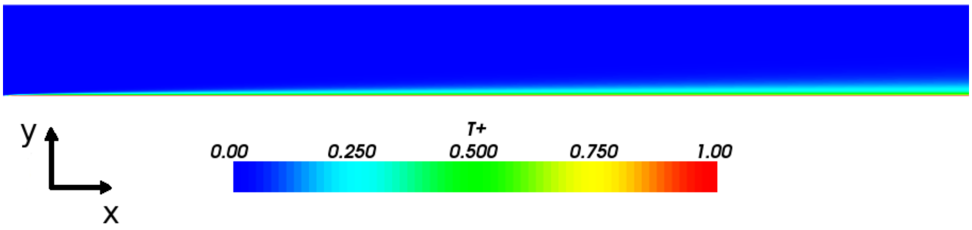

(a)

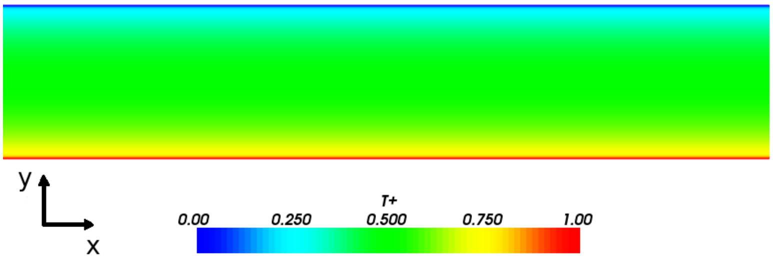

(b)

Fig. A.1: Temperature distribution inside the plane channel for an evolving temperature boundary layer (a) and for a fully developed thermal boundary layer using periodic boundary conditions for a Reynolds number $Re_H = 13043$ obtained from RANS computations (b).

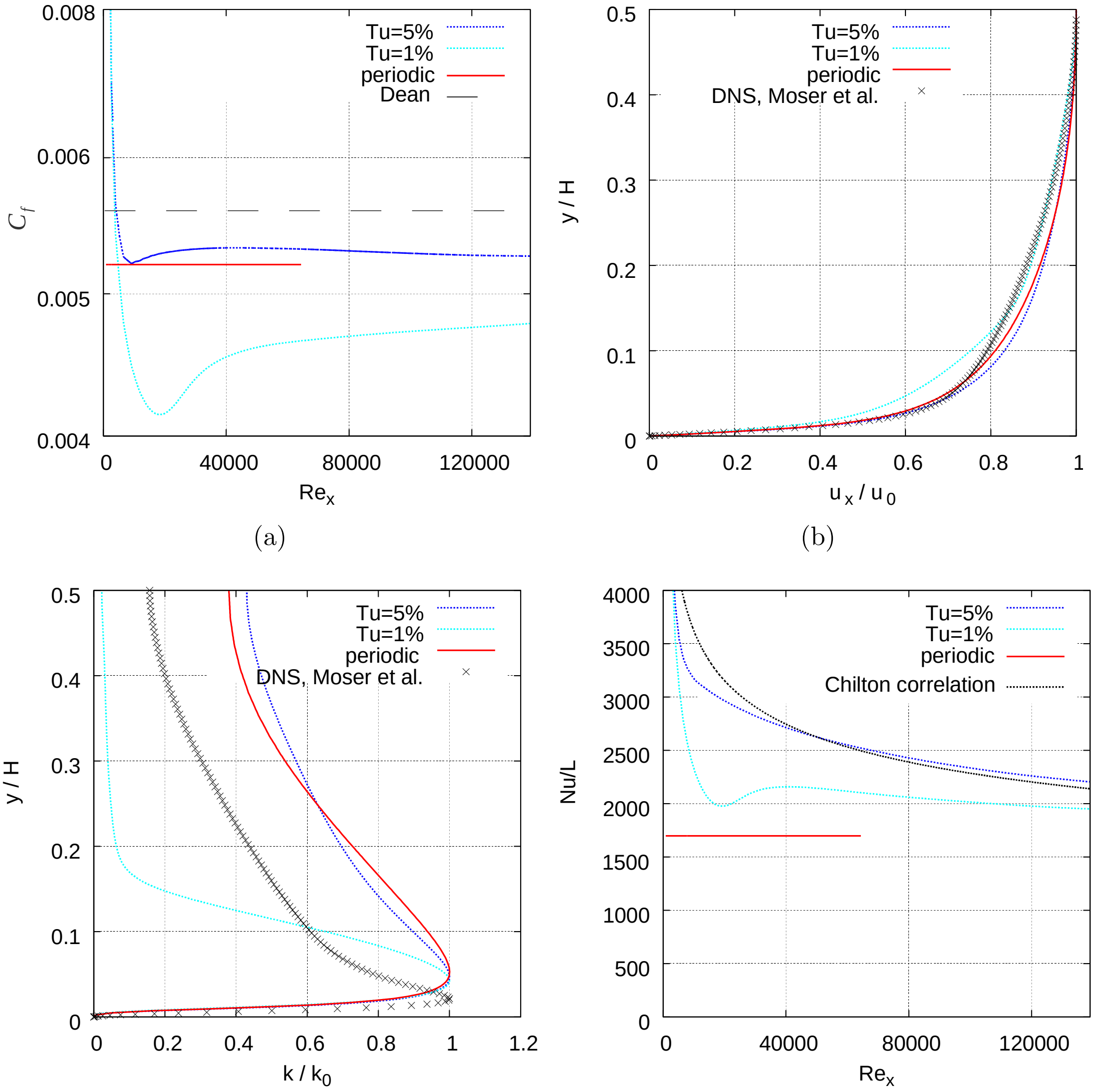

(a) (b)

(c) (d)

Fig. A.2: Numerical results obtained with RANS method at Reynolds number $Re_H = 13043$ for fixed inlet profiles with an turbulence intensity of $Tu = 1\%$ and $Tu = 5\%$ and periodic boundary conditions for (a) friction coefficient C_f in comparison to empiric correlation of Dean, for (b) mean velocity profile normal across the channel height in comparison to DNS data taken from Moser et al. [78], for (c) normalized kinetic energy k in comparison to calculated kinetic energy by Moser et al. and for (d) the Nusselt Number Nu distribution along the flow direction at the lower channel wall in comparison to empiric correlation of Chilton and Colburn [4].

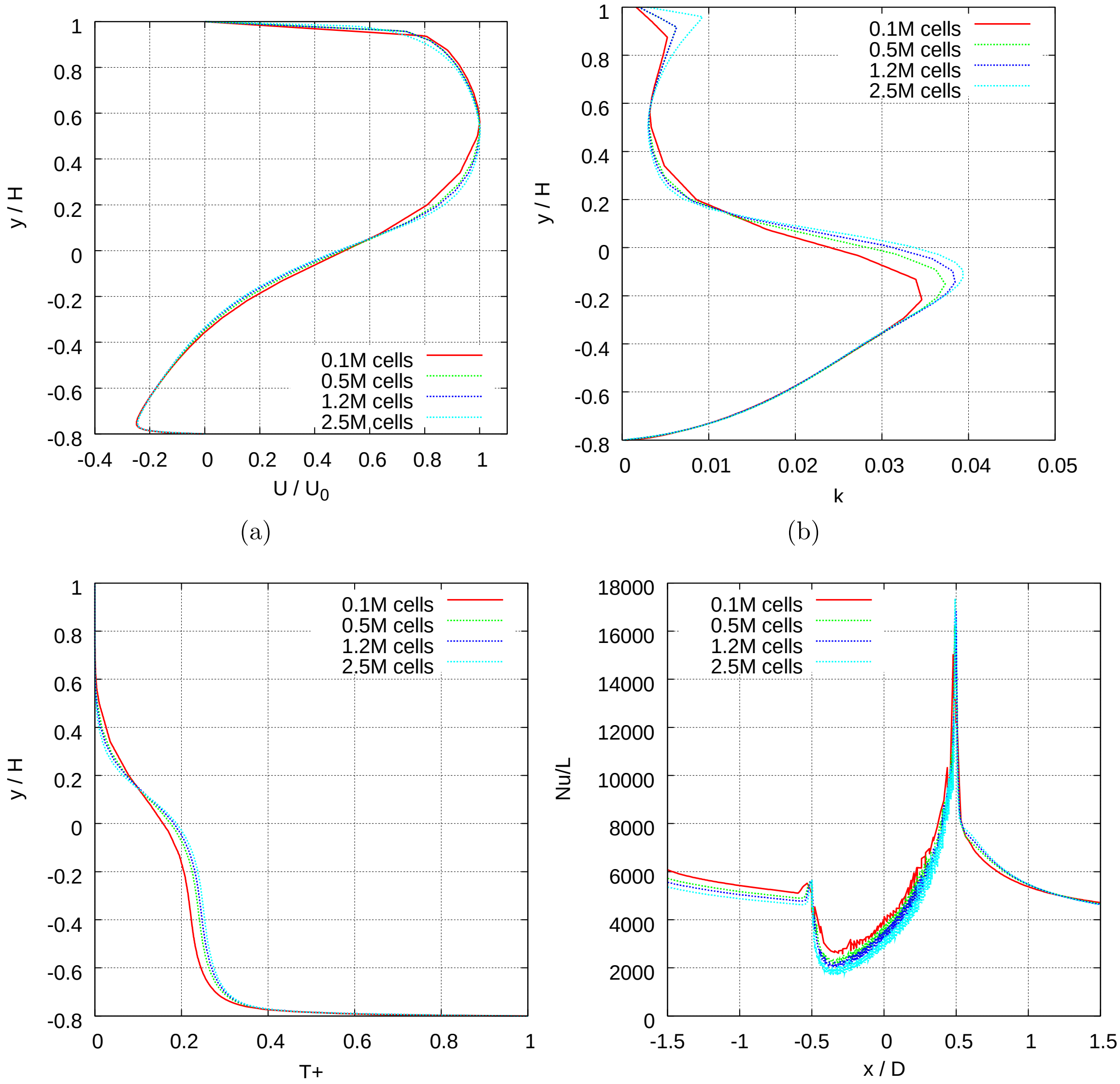

(a) (b)

(c) (d)

Fig. A.3: Numerical results obtained with RANS method for different mesh resolutions at Reynolds number $Re_H = 13043$ for turbulent flow over a single spherical dimple.

B LDA Measurements of turbulent flow over a spherical dimple

In this section the measurements are compared to experimental results performed by Terekhov et al. [89] to estimate reliability of the experiments.

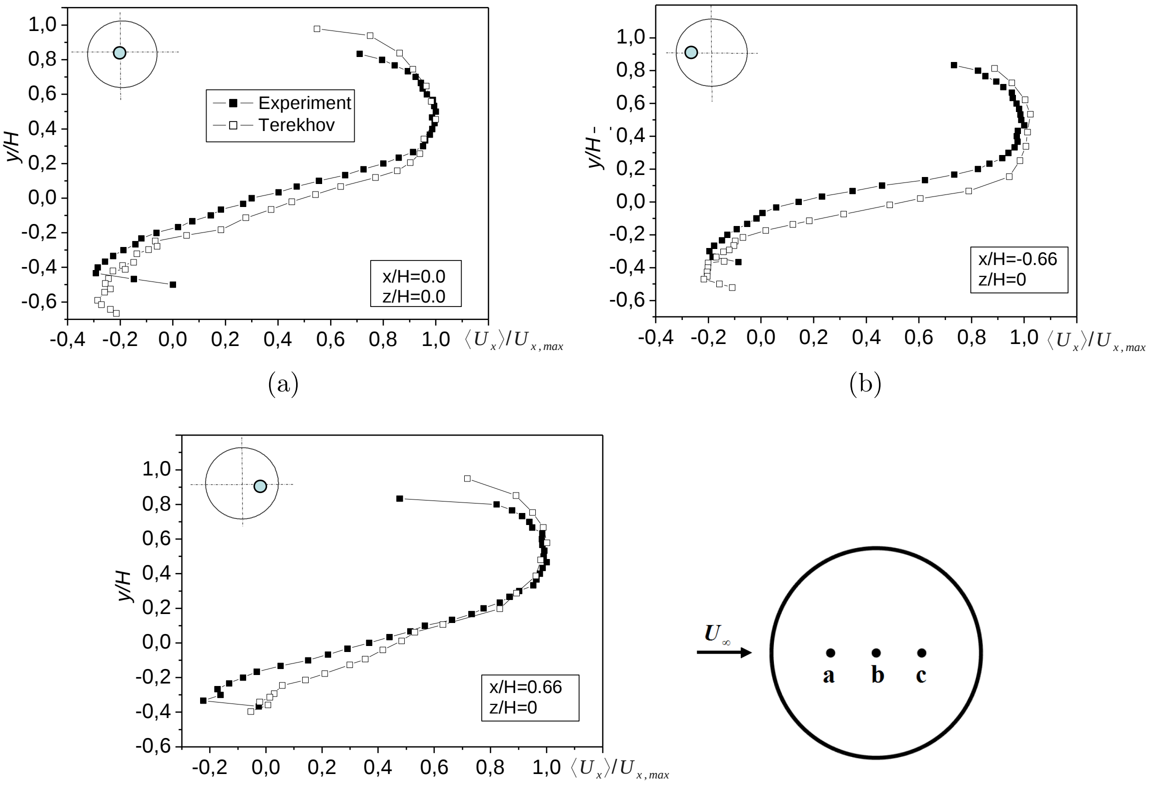

(a) (b)

(c)

Fig. B.1: Mean profiles of axial velocity U_x inside a single dimple for $Re_d = 40000$ normal to the channel wall in comparison with experimental results from Terekhov et al. [89] at three different positions normalized by the time averaged axial velocity U_0.

Fig. B.1 shows the time averaged axial velocity $\langle U_x \rangle$ normal to channel surface at different axial positions ($x/H = 0$, $x/H = \pm 0.66$) at the mid plane of the dimple

($z/H = 0.0$) normalized by the maximum velocity inside the channel in comparison to results from Terekhov et al. [89]. At each measurement point data was collected over a long time period of at least $20s$ realtime to ensure statistical independence. In this case the point of origin was placed at the dividing surface of dimple and channel at $x/H = 0.0$ respectively. The measured profiles that have data points extending from wall and show good agreement in comparison to Terekhov et al. [89]. Moreover the profiles at the positions $x/H = 0$ and $x/H = -0.66$ reveal clearly the presence of a recirculation zone inside the dimple with negative velocities up to $U_x = -0.3\ m/s$ where at position $x/H = 0.66$ only velocities against main flow direct could be observed. At all measured positions a large generated shear layer between the main flow and the reverse flow is present where the point of $U_x = 0.0$ moves inside the dimple. Nevertheless it can be seen, that there existing several discrepancies to the reference data. First the measured points located near the wall reveal unrealistic velocities and a clear recirculation zone cannot be observed inside the dimple from measurements in this work. Main reasons for the deviation are reflections from the laser beam of the walls and the large size of the control volume of the two laser beams of the LDA device. The magnitude of deviation becomes more significant while comparing the pulsations of the longitudinal velocity at the equal positions as for the mean velocity inside the dimple.

In Fig. B.2 the rms values of the axial velocity are presented in comparison with Terekhov et al. [89]. As mentioned before the presence of a shear layer between the recirculating flow and main channel flow lead to an increase of fluctuations due to the high velocity gradients. The highest magnitude of pulsations can be found near the upper channel wall and at the dividing surface between channel and dimple where the magnitude of both peaks of the fluctuations are nearly the equal. It is interesting to note, that in measurements of Terekhov et al. [89] the location of the peak lies about $y/H = -0.2$ down from the channel wall which is contradictory to actual measurements. The strongest gradients in performed measurements were found at the mid-plane at $x/H = 0.0$ which leads to the conclusion, that at this point the highest fluctuations should be observed.

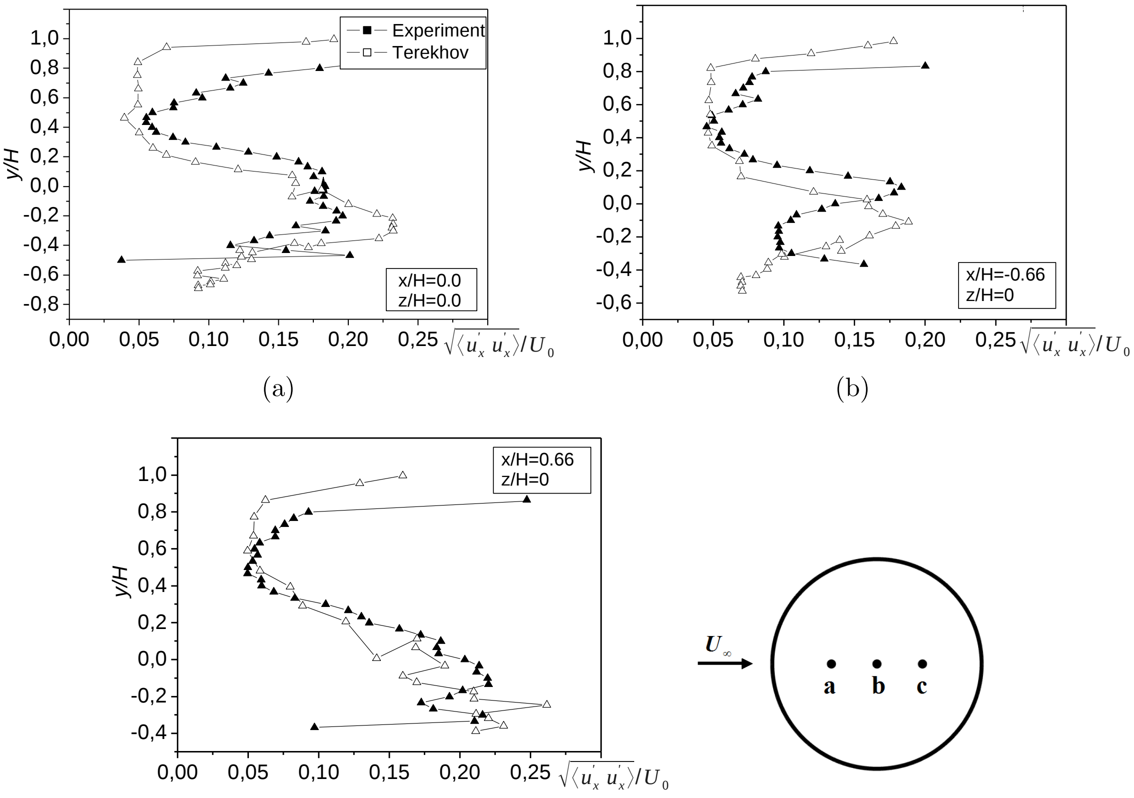

(a)

(b)

(c)

Fig. B.2: Distribution of rms values of axial velocity U_x inside a single dimple for $Re_d = 40000$ normal to the channel wall in comparison with experimental results from Terekhov et al. [89] at three different positions normalized by the time averaged axial velocity U_0.

Declaration in lieu of oath

I hereby declare that this submission is my own work and that, to the best of my knowledge and belief, it contains no material previously published or written by another person nor material which to a substantial extent has been accepted for the award of any other degree or diploma of the university or other institute of higher learning, except where due acknowledgment has been made in the text.

Rostock, 04. October 2011 Johann Turnow